



Jordanian Journal of Computers and Information Technology

August 2017

VOLUME 03

NUMBER 02

ISSN 2415 - 1076 (Online)
ISSN 2413 - 9351 (Print)

JJCIT

PAGES

PAPERS

71- 88

A REVIEW ON WIRELESS POWER TRANSFER IN FREE SPACE AND CONDUCTING LOSSY MEDIA

Rula Alrawashdeh

89 - 109

ADJACENT CHANNEL INTERFERENCE REDUCTION IN OFDM SYSTEMS

Arwa Waleed Mustafa and Khalid G. Samarah

110 - 130

NOVEL TECHNIQUE FOR SECURING DATA COMMUNICATION SYSTEMS BY USING CRYPTOGRAPHY AND STEGANOGRAPHY

Walaa H. Al-Qwider and Jamal N. Bani Salameh

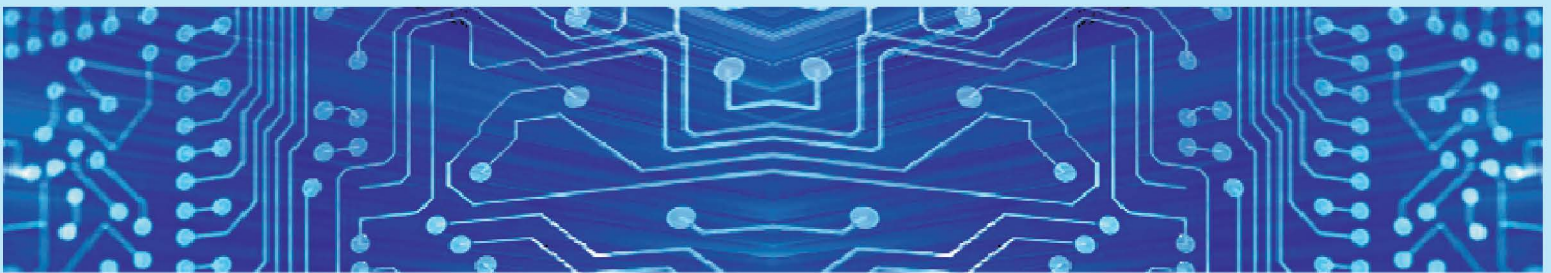
131- 141

EFFECT OF MULTIPLEXER/DEMULTIPLEXER BANDWIDTH ON UPGRADING CURRENT 10G TO 40G OPTICAL COMMUNICATION SYSTEMS

A. Atieh, M. Wa'ad and I. Mansour

www.jjcit.org

jjcit@psut.edu.jo



An International Peer-Reviewed Scientific Journal
Financed by the Scientific Research Support Fund

Jordanian Journal of Computers and Information Technology (JJCIT)

The Jordanian Journal of Computers and Information Technology (JJCIT) is an international journal that publishes original, high-quality and cutting edge research papers on all aspects and technologies in ICT fields.

JJCIT is hosted by Princess Sumaya University for Technology (PSUT) and supported by the Scientific Research Support Fund in Jordan. Researchers have the right to read, print, distribute, search, download, copy or link to the full text of articles. JJCIT permits reproduction as long as the source is acknowledged.

AIMS AND SCOPE

The JJCIT aims to publish the most current developments in the form of original articles and review articles in all areas of Telecommunications, Computer Engineering and Information Technology and make them available to researchers worldwide.

The JJCIT focuses on topics including, but not limited to: Computer Engineering & Communication Networks, Computer Science & Information Systems and Information Technology and Applications.

INDEXING

JJCIT is indexed in:

- CrossRef:
<http://search.crossref.org/?q=jjcit>
- OCLC WorldCat:
http://www.worldcat.org/search?qt=worldcat_org_all&q=jjcit
- Scilit:
<http://www.scilit.net/journals/387088>
- DRJI (Directory of Research Journals Indexing):
<http://drji.org/JournalProfile.aspx?jid=2415-1076>

EDITORIAL BOARD

Ahmad Hiasat (EIC)

Dia Abu-Al-Nadi

"Moh'd Belal" Al-Zoubi

Sameer Bataineh

Ahmad Alshamali

Ismail Ababneh

Mohammad Mismar

Taisir Alghanim

INTERNATIONAL ADVISORY BOARD

Ahmed Yassin Al-Dubai
UK

Chip Hong Chang
SINGAPORE

Fawaz Al-Karmi
JORDAN

Gian Carlo Cardarilli
ITALY

João Barroso
PORTUGAL

Khaled Assaleh
UAE

Lewis Mackenzies
UK

Marc Dacier
QATAR

Martin T. Hagan
USA

Michael Ullman
USA

Mohammed Benaissa
UK

Nadim Obaid
JORDAN

Omar Al-Jarrah
JORDAN

Paul G. Plöger
GERMANY

Shambhu J. Upadhyaya
USA

Albert Y. Zomaya
AUSTRALIA

Enrique J. Gomez Aguilera
SPAIN

George Ghinea
UK

Issam Za'balawi
JORDAN

Karem Sakallah
USA

Laurent-Stephane Didier
FRANCE

Zoubir Hamici
JORDAN

Marco Winzker
GERMANY

Marwan M. Krunz
USA

Mohammad Alhaj Hasan
JORDAN

Mowafaq Al-Omsh
JORDAN

Nazim Madhavji
CANADA

Othman Khalifa
MALAYSIA

Shahrul Azman Mohd Noah
MALAYSIA

Wejdan Abu Elhaija
JORDAN

"Opinions or views expressed in papers published in this journal are those of the author(s) and do not necessarily reflect those of the Editorial Board, the host university or the policy of the Scientific Research Support Fund".

"ما ورد في هذه المجلة يعبر عن آراء الباحثين ولا يعكس بالضرورة آراء هيئة التحرير أو الجامعة أو سياسة صندوق دعم البحث العلمي".

A REVIEW ON WIRELESS POWER TRANSFER IN FREE SPACE AND CONDUCTING LOSSY MEDIA

Rula Alrawashdeh

(Received: 29-Dec.-2016, Revised: 08-Mar.-2017, Accepted: 02-Apr.-2017)

ABSTRACT

Recently, the interest in wireless power transfer (WPT) has significantly increased due to its attractive applications. The power transfer efficiency and communication range of most of the existing WPT systems are still limited, which is due to many technical challenges and regulation limitations. This requires more research and technical efforts to overcome the current limitations and make WPT systems much more efficient and widely used. This paper aims at reviewing recent advances and research progress in the area of WPT for the purposes of addressing current challenges and future research directions. To obtain these purposes, an introduction to WPT is provided. Also, main research themes of WPT in free space and lossy media are discussed. Additionally, the benefits of using split ring resonators WPT in conducting lossy media are investigated. This will be very helpful to boost WPT in lossy media and inspire more optimized structures for further improvement.

KEYWORDS

ICPT, MPT, PTE, UWICPT, WPT.

1. INTRODUCTION

Wireless power transfer (WPT) is a process of transferring electrical energy from transmitter to receiver ends without wires. It can be applied to power and charge different devices, such as mobile phones. Such applications will be very beneficial to increase the life time of devices and save their internal space which is mainly occupied by batteries. Additionally, WPT is green for the environment, as no batteries may be used [1]. The principle of WPT has been introduced since the days of Nikola Tesla and WPT has been adopted for commercial use for some small items, such as phones, toothbrushes and cochlear implants [2]-[4]. However, power transfer efficiency and range for most of commercial systems are still limited. Due to the promising applications of WPT in different media, research is ongoing to improve the efficiency and feasibility of WPT despite its challenges.

WPT techniques fall mainly into two categories: non-radiative and radiative techniques [2]. Most of research themes of all WPT types focus mainly on increasing power transfer efficiency and range. The research progress in the area of WPT has been reviewed in this paper. Compared to other related review papers, this paper elaborates the challenges of WPT in conducting lossy media, such as the human body. Further, it summarizes the work that has been conducted in the area of WPT to implantable and underwater devices. Additionally, it indicates the beneficial effect of using a layer inspired by split rings around antennas in a lossy medium on the WPT process. This paper is arranged as follows: First, an introduction to the principle and types of WPT is provided. Then, the research that has been conducted in the areas of inductive and microwave-based WPT in free space and lossy media (the human body and underwater devices) is reviewed and related challenges are summarized. Finally, the beneficial effect of using a layer inspired by split ring resonators on boosting WPT in lossy media is indicated and demonstrated by measurements.

2. TYPES AND PRINCIPLE OF OPERATION

The principle of operation and main characteristics of different types of WPT are discussed and summarized in this section.

2.1 Non-Radiative WPT

In non-radiative techniques, power is transferred by the following methods:

2.1.1 Inductive Coupling Power Transfer (ICPT)

A typical inductive coupling system is shown in Figure 1. It is composed of transmitter and receiver coils (TC and RC, respectively) of self-inductances of L_{TX} and L_{RX} (H), respectively. The TC is connected to an AC source of V_s (V) voltage and R_s (Ω) internal resistance and the RC is connected to a load resistance R_L (Ω). A current $i_1(t) = I_1 \sin(\omega t)$ passing through the primary coil produces a magnetic field as explained by Ampere's law given in Equation (1). Most of this magnetic field links the secondary coil which induces a voltage and current as explained by Faraday's law given in Equation (2). Hence, power can be delivered to the load.

$$\oint \vec{H} \cdot d\vec{L} = i. \quad (1)$$

\vec{H} (A/m) is the magnetic field intensity and $d\vec{L}$ (m) is a differential length element along the closed path that encloses the current i (A) [5].

$$\text{emf} = -N \frac{d\Phi}{dt}. \quad (2)$$

emf (V) is the electromotive force (induced voltage), N is the number of turns of the secondary coil and Φ (Wb) is the magnetic flux [5].

The flux linkage between coils is proportional to the current $i_1(t)$ and mutual inductance between coils (M); $\Phi = M i_1(t)$. Hence, the voltage at the receiver terminals $V_r(t)$ (V) can be expressed as [6]:

$$V_r(t) = M \frac{di_1(t)}{dt} \equiv M \omega I_1 \cos(\omega t). \quad (3)$$

This technique offers the advantages of simplicity and safety. Also, energy is stored in the region between coils and no radiation will be lost to the surrounding area. Therefore, it has been widely used in different applications, such as charging medical implants. However, this technique has the shortcomings of short transmission range and sensitivity to misalignment between transmitter and receiver coils. Additionally, strong electromagnetic fields can be harmful to the human health. Therefore, it is important to evaluate the resonant system for WPT applications where humans are exposed to electromagnetic fields to ensure that the safety levels enacted by the European Union [7] are satisfied. If the distance between coils increases, the induced voltage at the receiver decreases. To increase the power transmission efficiency (PTE) over a longer distance, resonant circuits are used as will be discussed in the following section.

2.1.2 Magnetic Resonant Coupling (Electrodynamic Induction)

A typical magnetic resonant coupling system is shown in Figure 2. It is composed of transmitter and receiver coils and capacitors. For simplicity, the self-inductance for each coil is supposed to be (L (H)) and the capacitance of each capacitor is (C (F)). Maximum power transfer occurs at the resonant frequency to which the resonant circuits in the transmitter and receiver are tuned. If the distance between coils increases, the mutual coupling between coils decreases and thus $V_r(t)$ decreases accordingly (see Equation (4)). The frequency or TC current can be increased to compensate for any reduction in the induced voltage [6], [8]. However, the current in the transmitter coil is usually utilized to increase $V_r(t)$ as electromagnetic radiation and hence power dissipation around the system is possibly generated at very high frequency [6]. When a resonant frequency of $\omega_{res} = 1/\sqrt{LC}$ is approached, the currents in coils grow to the huge resonant currents $i_{1res}(t)$ and $i_{2res}(t)$ (A) at the transmitter and receiver coils, respectively. These currents produce a noticeable voltage at the receiver ($V_r(t)$) and hence enough power can be delivered to a proper load [6]:

$$V_r(t) = M \frac{di_{1res}(t)}{dt} + L \frac{di_{2res}(t)}{dt}. \quad (4)$$

Another effective parameter of the magnetic resonant power transfer system is the quality factor (Q-factor), which is a measure of the ratio between the energy stored by L and C and the energy loss rate (the loss is represented by R in the circuit) [9]. In general, resonators of high Q-factors are required for an efficient power transfer at small coupling levels and longer distance between the transmitter and

receiver [10]. The main shortcoming of this technique is the difficulty to adjust the resonant frequency when charging multiple devices [11]. Also, at close ranges when the two resonant circuits are tightly coupled, the resonant frequency of the system is no longer constant, but "splits" into two resonant peaks, so the maximum power transfer no longer occurs at the original resonant frequency and the oscillator frequency must be tuned to the new resonance peak [12].

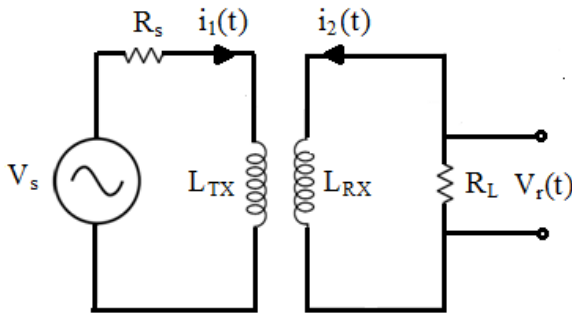


Figure 1. A typical inductive coupling system [6].

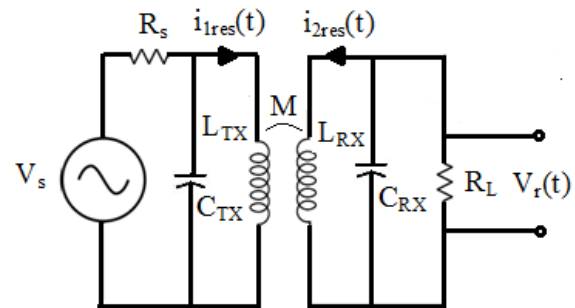


Figure 2. A typical magnetic resonant coupling system.

2.1.3 Capacitive Coupling (Electrostatic Induction)

In this technique, the transmitter and receiver electrodes form a capacitor as shown in Figure 3. An alternating voltage generated by the transmitter induces an alternating potential and current on the receiver plate by electrostatic induction [2]. It is worth indicating that this method will not be surveyed in this paper.

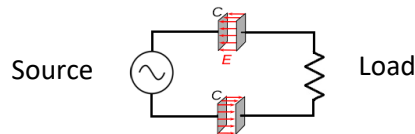


Figure 3. Capacitive coupling.

To overcome the limitations of non-radiative WPT and provide longer transmission ranges, power is transmitted using radiative techniques via microwaves or visible light.

2.2 Radiative WPT

2.2.1 Microwave Power Transfer (MPT)

For the case of power transfer via microwaves, a transmitting antenna emits electromagnetic waves to a receiving antenna which is connected to a rectifier in the rectenna as shown in Figure 4. The rectifier converts the ac power to dc power. An ideal diode for rectenna application with a small turn-on voltage or zero-bias is preferable, as well as with large reverse breakdown voltage and low capacitance. It should also have a high power handling capacity [13]. A matching circuit is used to match the antenna to the rectifier circuit. A filter is usually used before rectification to ensure that the incoming RF signal is operating at the desired frequency for the rectifier and prevent re-radiation of higher-order harmonics produced by the non-linear I-V characteristics of the rectifying diode. It will also reject out-of-band interference signals. The post-rectification filter is used to extract the dc component and reflect the rest of the frequencies back to the rectifier [14].

The conversion efficiency η of the whole system is the ratio between the DC output power at the receiver end $P_{out,DC}$ (W) and the input AC power $P_{in,AC}$ (W) at the receiver front [1]:

$$\eta = \frac{P_{out,DC}}{P_{in,AC}}. \quad (5)$$

$P_{out,DC}$ (W) delivered to the load resistance R_L (Ω) can be calculated using:

$$P_{out,DC} = \left(\frac{V_{out,DC}^2}{R_L} \right). \quad (6)$$

$P_{in,AC}$ (W) is mainly defined by the incident power density P_d (W/m²) and effective area of the receiving antenna A_{eff} (m²) [15]:

$$\begin{aligned} P_{in,AC} &= (P_d)(A_{eff}) = \left(\frac{P_t G_t}{4\pi d^2}\right) \left(\frac{\lambda^2 G_r}{4\pi}\right) \\ &= \frac{P_t G_t G_r}{(4\pi d/\lambda)^2} ; \end{aligned} \quad (7)$$

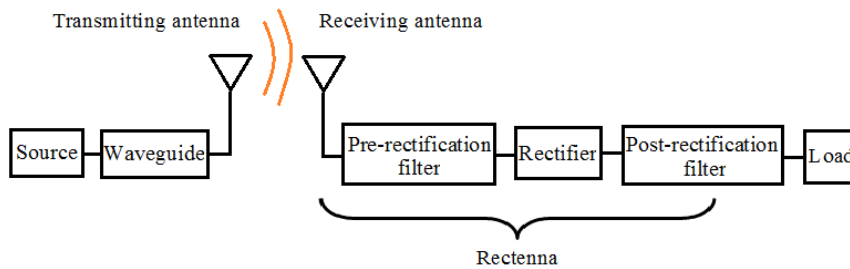


Figure 4. A typical microwave power transfer (MPT) system.

where P_t (W) is the transmitted power, G_t and G_r are gain of the transmitting and receiving antennas, respectively, λ (m) is the free space wavelength and d (m) is the distance. This equation shows that antennas of larger gain are capable of radiating and receiving larger power [16].

This technique has the advantage of transferring power over longer ranges than those for non-radiative techniques. Also, the rectenna lifetime is unlimited, as it does not need replacement (unlike batteries). However, the RF/microwave power is reduced from the transmitter through attenuation, mainly due to free-space path loss. Moreover, line of sight (LOS) transmission and small rectenna size are required [17]-[18].

2.2.2 Laser-Based WPT

In this case, power can be transmitted by a laser beam [19]-[20]. In comparison with MPT, laser systems offer larger improvement capacities and potentially much smaller systems [19]. However, laser radiation is hazardous and the conversion between electricity and light is limited. It is worth indicating that reviewing and investigating this technique is beyond the focus of this paper.

2.3 Main Characteristics and Applications of WPT in Conducting Media

WPT has many beneficial applications in lossy media, such as powering and charging implantable and undersea water devices [21]-[22]. For implantable applications, WPT can be achieved using: 1) primary coil on the skin and secondary coil beneath it (inductive coupling), or 2) two lightly coupled coils; one on the skin and another one deeply implanted inside the human body (magnetic resonant coupling), or 3) far field power transfer from a transmitter outside the human body (via microwaves). Power can be also transferred to an ingestible capsule that rotates while taking pictures of the digestive tract for the applications of wireless capsule endoscopy (WCE). WPT for these applications will be very beneficial to increase the lifetime of the device and save surgeries that are usually used to replace or charge the battery. For underwater wireless sensors, there is a variety of important applications. They are used to monitor environmental or physical phenomena, such as temperature, humidity, ... etc. and to spread data through a sensor network to a shore access point [23]-[24]. There are also applications where the receiver is placed around the lossy medium, such as wearable sensors [25]. The review of WPT for wearable devices is beyond the focus of this paper.

The conducting medium is lossy and most of the power is absorbed inside it. Most of lossy media, such as the human body and sea water, are nonmagnetic and do not present magnetic losses ($\mu_r = 1, \mu_r'' = 0$). Hence, the magnetic field is not dissipated in the region close to the source. The electric near field couples with the lossy medium and causes power loss due to absorption.

The absorbed power (P_{abs}) increases with the magnitude of the electric near field intensity ($|E|$) [26]:

$$P_{\text{abs}} = \frac{\omega}{2} \iiint \epsilon_0 \epsilon''_r |E|^2 dV; \quad (8)$$

where ω (rad/s) is the angular frequency, ϵ_0 (F/m) is the free space permittivity and ϵ''_r is related to the imaginary part of the tissue permittivity which accounts for the electric losses of the medium [26]-[27].

$$\epsilon = \epsilon_0 (\epsilon'_r - j\epsilon''_r). \quad (9)$$

Conductivity and permittivity of these lossy media are frequency -and temperature- dependent. The main challenge in all these applications is to mitigate the negative effect of the lossy medium on the power transfer system as much as possible. Requirements of the inductive coupling WPT for implantable applications in the lossy human body can be summarized as follows:

1. Small coil dimensions that fit into the available space inside the small implantable device.
2. Large inductance and quality factor Q over the frequency range of interest given the limited available space and size. This represents a challenge as an implantable coil of small size has usually a small inductance [28].
3. Robust performance with the other internal components of the implant (the performance should not be altered with the overall device package).
4. Robustness against misalignments.
5. Satisfaction of safety limitations.

Some of these requirements are contradictory as indicated in point 2. Thus, design parameters should be carefully adjusted to obtain the largest possible inductive coupling for a compact size. The probability of misalignment to happen is high for this case because of the changing and time-variant human body environment. For the case of underwater sea applications, size and safety requirements are less restricted. For the case of MPT for implants, antennas of magnetic type, such as loop antennas are preferred, because non-magnetic lossy media do not present magnetic losses. It is very important to satisfy the safety limitations of the specific absorption rate (SAR) and current density in order not to heat up the human body tissues [29]-[30]. The SAR can be calculated using Equation (10); where σ (S/m) and ρ (kg/m³) are the tissue conductivity and mass density, respectively, and $|E|$ is the magnitude of electric near field intensity. Excessive received power may cause overheating of the receiver coil, but according to the Japan Society of Medical Electronics and Biological Engineering (JSMEBE), temperatures below 42.5 °C are safe for the tissues surrounding the RC [31].

$$\text{SAR} = \frac{\sigma |E|^2}{\rho}. \quad (10)$$

3. RESEARCH PROGRESS AND CHALLENGES

In this section, the main contributions and challenges in the area of WPT are reviewed.

3.1 Inductive WPT

3.1.1 In Free Space

Many WPT systems based on inductive coupling were presented in literature for both of low (mill watts) and high power (multiple kilowatts) applications, such as charging mobile phones and powering electric vehicles, respectively [32]-[33]. A PTE of more than 75% was obtained for these systems at a distance of less than 10 cm between the transmit and receive coils [34]. A mobile phone charger was developed in [32] at 1.2 MHz. For this system, an output DC voltage of 3.79 V was obtained at the load when the distance between the TC and RC was 5 cm. An inductive coupling system was also proposed in [35] for a radio frequency identification (RFID) system. However, PTE decreases with distance and when misalignment happens. Moreover, the receiver mobility is very restricted. Research has been directed to overcome these shortcomings as summarized in Table 1.

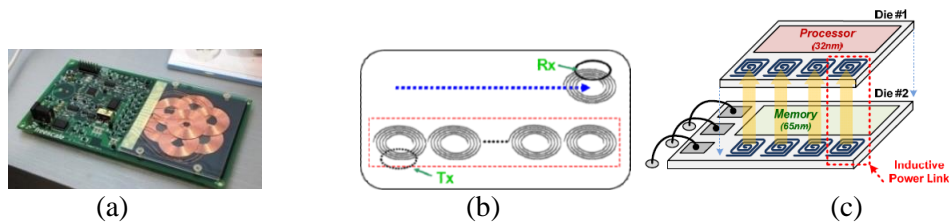


Figure 5. Proposed designs of multiple coils and resonators in: (a) [36], (b) [37] and (c) [38].

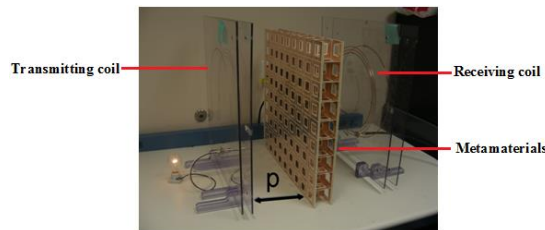


Figure 6. The proposed metamaterial in [40].

Based on the review above, it can be concluded that future investigations may be directed to:

1. Investigate the effect of using multiple metamaterial slabs and different metamaterial structures to obtain further improvement of WPT.
2. Design flexible coils that reduce the weight and size of the ICPT system and investigate the effect of the flexible structure on the coil parameters and performance.

3.1.2 In a Conducting Medium

Research on inductive power transfer in the lossy human body and underwater devices is reviewed in this section.

3.1.2.1 Underwater Applications

Underwater inductive coupling power transfer (UWICPT) system with resonant circuits has been shown to be a good candidate for charging underwater devices and vehicles. Such a system was presented in [49] for autonomous underwater vehicle docking applications. Figure 7 shows the installation of the coils in an AUV docking system. The output power was up to 45 W and the efficiency was up to 84%. A circuit and a finite element analysis (FEA) simulation model were developed to study the system power losses to increase the system efficiency. The electrical characterization of coupled electromagnetic coils in saltwater for an undersea WPT system was presented in [50]. It was indicated that the electrical properties of coils and their mutual coupling were almost identical whether in air or in saltwater at frequencies below 100 kHz, but different above 100 kHz, as seawater becomes much more effective. An underwater WPT system was realized in [51] for high power applications to recharge underwater vehicles. It was demonstrated that 3 kilowatts of power could be transferred over 15 cm with a high efficiency of around 80%.

All of these systems have validated ICPT for underwater applications. However, further research should be conducted to:

1. Increase the power transfer efficiency of WPT over longer ranges.
2. Generalize the effect of overall losses of the WPT system on its output power and efficiency.
3. Investigate the effect of packaging and realization of the ICPT system on the PTE.
4. Investigate and quantify the detrimental effect of seawater on the resistance of the coils and their coupling performance.

3.1.2.2 Implantable Applications

In this review, implantable applications are divided into two categories: WCE and implantable applications other than WCE.

3.1.2.2.1 WCE Applications

Magnetic resonant WPT is mainly used for this case, as the distance between TC and RC is relatively long. Low power levels are usually required to power or charge wireless capsules.

Table 1. A summary of main design approaches for inductive WPT in free space in literature.

Facility of improvement: Multiple coils. See Figure 5.		
Ref. and proposed approach	[36]	Multiple overlapped transmitter coils
Achievements	Mitigation of misalignment. Multiple receiver coils can be powered at the same time.	
Shortcomings	Increase of design size and complexity as a control IC is used to detect which coil is the best for WPT.	
Ref. and proposed approach	[37]	Array of coils of similar resonant frequency
Achievements	Increase of mobility range of the receiver. Increase of power transfer range. Multiple receiver coils can be powered at the same time. PTE of around 85% at $f=25$ MHz for 10 resonant loops.	
Shortcomings	Increase of design size and complexity.	
Ref. and proposed approach	[38]	Planar spiral coils are designed using a $0.13\mu\text{m}$ CMOS process and vertically stacked.
Achievements	Increase of the amount of the transferred power which depends on the coil's diameter and distance between coils. PTE of 52% for a power transfer density of 49 mW/mm^2 .	
Shortcomings	Increase of design size.	
Facility of improvement: Metamaterials. See Figure 6.		
Ref. and proposed approach	[39]	An NIM slab used between two resonators
Achievements	Improvement of magnetic coupling and hence power transfer efficiency due to enhancement of the evanescent wave coupling. PTE of around 50% at $f=10$ MHz.	
Shortcomings	Complicated to design and fabricate, because both of ϵ and μ are required to be negative. Large loss, as it responds to both of electric and magnetic fields.	
Ref. and proposed approach	[40], [41]	A single negative ($\mu = -1$) metamaterial slab between resonators.
Achievements	Increases PTE with smaller losses and complexity in comparison with those of the NIM slab. [40] PTE of 50% at $f=27.12$ MHz which is 42% larger than that when no metamaterial slab is used. [41] PTE of 18.2% at $f=26.65$ MHz which is 61% larger than that when no metamaterial slab is used.	
Shortcomings	Larger losses than those when no slab is used.	
Facility of improvement: Techniques for mitigating frequency splitting.		
Ref. and proposed approach	[42], [43], [44], [45], [46]	Frequency tracking/ tuning techniques.
Achievements	The driving frequency of the ICPT link is maintained at an optimum value to ensure that the link is working at resonance and the output voltage is maximized. [42] PTE of over 70% for a range of 0-70 cm. [46] PTE of 15% at $f=4.5-5.5$ MHz.	
Shortcomings	Additional space and power consumption are introduced because a series of complex control circuits -such as phase compensator phase-locked loop- is required.	
Ref. and proposed approach	[47], [48]	Anti-parallel resonant loops, Non-identical resonant coils (NIRCs)
Achievements	Offset of excess mutual inductance (magnetic over coupling) which is the reason of frequency splitting.	
Shortcomings	Further investigations on the system stability and impact of coil parameters on the overall system performance are required.	

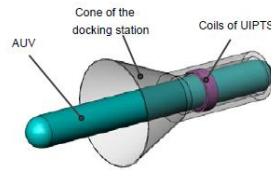


Figure 7. The UICPT system in [49].

However, the received power decreases for some orientations while the capsule is rotating in the digestive tract. To overcome these limitations, some approaches were presented as summarized in Table 2.

Table 2. Approaches to overcome ICPT limitations for WCE applications presented in literature.

Ref.	The approach	The benefit
[52]	3D orthogonal RC	The receiver delivers more than 300 mW at any orientation.
[53]	A hollow-cylinder-like 3D RC	Improves space utilization in comparison with typical 3D RC. An output power ranging from 206 mW to 1130 mW was obtained which powered the capsule robot successfully.
[54], [55]	Utilization of a ferrite core	Increases the magnetic field intensity and the received power at the RC. A ferrite core of large magnetic permeability and small loss factor is used for larger improvement. Reduces the size of the RC. 330 mW was received by the capsule.
[56]	A pair of double-layer TC solenoids	Produces a larger magnetic field intensity and PTE in comparison with that for a single solenoid and pair of solenoids.
[57]	Segmented TC solenoids	Improve the efficiency of the WPT system in comparison with non-segmented solenoids.
[58]	Helmholtz TC	Provides a much more uniform magnetic field within the inner region in comparison with that for the solenoid and reduces the risk of unnecessary exposure in the patient's body.

It is obvious that solutions of a ferrite core and 3D RC increase the capsule weight and profile. Moreover, the biocompatibility of the ferrite core should be validated. The detuning effect differs in different human bodies and becomes very large in close proximity to the fat layer [59]. No food and drink should be taken for around 10 hours before the investigation and 2-4 hours after swallowing the capsule [60], which means that the digestive tract will be filled up mostly with air for this case. Most of the existing software packages consider a digestive tract that is filled up with food of much larger permittivity than that for air, such as in [61]. This requires an accurate body model of the digestive tract when filled up with air (a model of an effective permittivity between air and tissues of the digestive tract). Therefore, an accurate in vitro test (inside a human body phantom) is very important and should be conducted. Based on this review of ICPT for WCE, it can be also concluded that further investigations on the SAR and safety limitations should be provided. More practical designs of light weight and small profile are also still needed.

3.1.2.2.2 Other Implantable Applications

For implantable (low power) applications other than WCE, magnetic resonant coupling is mainly used to transfer power to implants such as pacemakers. Examples can be found in [62]-[63]. In [64], a WPT system of resonant four coils was presented. The power transfer efficiency of the resonant four coils was shown to be much higher than that of two coils. An approximate output voltage of 3.3 V and a current of 10 mA were obtained at a distance of 2 cm. In addition, it was possible to obtain power larger than 100 mW when the distance was decreased, which can meet the power requirements of most reported biomedical implant consumption, such as artificial retina, intraocular pressure, and neural

recording system. Printed coils for magnetic resonant coupling were designed in [26], [65]. In [65], a procedure to design the geometries of a pair of lithographically planar printed spiral coils was presented. This procedure optimized the mutual inductance and quality factor of printed coils in a way that the PTE was maximized. A flexible coil design was also presented in [66]. The transmitter and receiver coils were realized by inkjet printing. Wireless power transfer efficiencies of 55% and 35% at 13.56 MHz were obtained for the air and water (for testing purposes) surrounding environments, respectively. The printed and flexible designs help in providing more conformity and reducing the device size, weight and profile. However, further studies are still needed to: characterize the effect of the lossy human body on the design parameters and performance of printed or flexible coils, derive formulae of the design parameters for different structures of printed or flexible coils and evaluate the performance of flexible coils when they get bent.

3.2 Microwave-Based Systems

3.2.1 In Free Space

Research in this area has been mainly focused on optimizing the design of the receiving antenna and rectifier circuit. For the rectifier circuit, different rectifier diodes were used. Examples can be found in [67] and [68], where (HSMS-8101) and (HSMS2860) Schottky diodes were used, respectively because of their high speed and low voltage drop. A novel wide dynamic range and high-efficiency rectifier was proposed in [69]. The proposed rectifier consisted of two rectifying circuits in parallel, an asymmetrical output impedance power divider which adaptively divided the RF input signal to the rectifying circuits according to a signal power level and a DC combiner. More than 27 dB dynamic range with an RF-DC conversion efficiency of higher than 50% was obtained. A maximum conversion efficiency of 76.8% at 2.45 GHz was obtained at an input power of 5dBm. In [70], metasurfaces composed of different types of resonators were used instead of antennas in the rectenna, as they were found to be more efficient than classical antennas in energy harvesting. However, no in-depth study has been provided to explain the overall benefits of metasurfaces for the WPT process in general (not for harvesting purposes only). Antenna optimization techniques proposed in literature are summarized in Table 3. Metamaterials and metamaterial-based structures are found to be very advantageous for ICPT. Therefore, it is important to investigate them for MPT in depth.

3.2.2 In a Lossy Medium

For implantable rectennas, different types of antenna were designed and presented as summarized in Table 4. It is worth indicating that the comparison between different implantable rectennas can be considered accurate only if the properties of the medium of implantation is the same for all of them. Magnetic type antennas, such as loop antennas, are popular for this type of application, because they are of smaller SAR and larger radiation efficiency and gain. PIFAs have the advantages of small size and low profile in addition to relatively small electric near field and SAR. 0.433 GHz is mainly exploited for the applications of implantable rectennas, because it enables size reduction of the rectenna system in comparison with that at lower frequencies. At the same time, the human body loss around this frequency is smaller than that at higher frequencies. For the rectifier design, it is preferred to facilitate low turn-on voltage and very low leakage current. Different rectifier designs in literature are summarized in Table 4.

It is very important to evaluate and validate the implantable rectenna performance with the overall package which may alter the overall antenna performance. This has been done in some research studies such as in [93]. However, further deep related investigations are still needed. Based on this survey of proposed designs in literature, future research should be focused on:

1. Introducing new techniques and designs that further increase the magnetic field or decrease the electric field in close proximity to the implantable antenna, in order to boost the power received at the rectenna.
2. Introducing new techniques to maintain matching (of the receiving antenna and between the receiving antenna and rectifier) in the time-variant human body.
3. Investigating the effect of the implantable device packaging on the WPT process.
4. Validating the WPT system by both of in-vitro and in-vivo tests.

5. Evaluating the WPT system using actual design parameters (load resistance, available diodes, ...etc.) for actual implantable chips in the market.
6. Characterizing the WPT channel of the human body in different areas of implantation for different implantable applications.
7. Investigating metamaterials or structures inspired by metamaterials for MPT in lossy media. The benefits of these structures will be indicated in the following section.

Table 3. A summary of antenna optimization techniques for MPT in literature.

Technique	Ref.	Structure/ Achievements	
Increasing the antenna gain	[71]	Artificial magnetic conductor (AMC) with a $\lambda/2$ dipole antenna/3.529 dB enhancement in gain.	
Antenna miniaturization	[72]	Wide slot antenna/Size reduction of 60% with a measured RF to-DC conversion efficiency of 75%.	
	[73]	A fractal structure/A maximum efficiency of 57% at an input power level of 20 dBm.	
	[74]	A slot of cross shape slot etched on a square aperture patch antenna/ A patch size reduction of 32.5%. RF-to-DC conversion efficiencies were 15.7% and 42.1% for input power levels of -20 dBm and -10dBm, respectively at 2.45 GHz.	
	[75]	Square patch with interconnection of four corner patches alternating with four strips and a fifth central patch/A size reduction of 60%.	
Direct matching between the antenna and rectifier	[67]	Folded dipole antenna	Saves the space of the matching circuit and simplifies the rectenna. RF/DC power conversion efficiencies were 49.7% and 72.9% at 0.868 and 2.45 GHz in [76] and [67], respectively.
	[76]	Yagi-Uda	
Increasing the bandwidth	[67]	Folded dipole antenna	
	[77]	A dual-polarized wideband rectenna with a cross-dipole/A maximum conversion efficiency of 57% was obtained at 1.7 GHz and over 20% over the frequency range from 1.6 to 2.5 GHz for an input power density smaller than 200 $\mu\text{C}/\text{m}^2$.	
Antenna array and Multiple-Input, Multiple-Output (MIMO) elements	[78] [79] [80]	The output voltage increases with the number of array elements.	
Circular polarization	[81] [82]	[81] Truncated patch, [82] two crossed slots introduced to the ground of a patch antenna and coupled on a microstrip feed line/Overcomes the limitations of rectenna orientation.	
Harmonic rejection	[83]	An optimized length of the feeding line and defect ground structure (DGS) of a microstrip rectenna are used to reject the second and third harmonics with a maximum conversion efficiency of 74%.	The insertion loss and rectenna size can be minimized when no low pass filter is used.
	[84]	DGS is applied near to the coaxially fed location of a microstrip antenna/20 dB suppression at the 2 nd and 3 rd harmonic frequencies.	
	[85]	Harmonics were suppressed with the aid of a spur-line that is inserted between the feed and short line of Planar Inverted-F Antenna (PIFA).	
	[86]	A single slot on a ground conductor of a CPW-fed circular slot antenna is utilized for the suppression.	

Table 4. A summary of proposed antennas for implantable rectennas in literature.

Ref.	Antenna type	f (GHz)	Dimensions (mm)	Tissue of implantation	The rectifier	Output voltage (V) or power (W)
[87]	Printed dipole	1.2	14×14	-----	Full-wave rectifier	3 V
[88]	Loop	0.433	30×15	Muscle	-----	-----
[18]	PIFA	0.915	10×12.5×1.5	Six-Layer rat head model	Couple of Schottky barrier diodes	-----
[89]	Folded helical	0.433	9.5×23	Muscle	-----	-----
[90]	Multilayer PIFA	0.433	10×10	-----	-----	-----
[91]	Slot PIFA	0.433	19×30×1.6	Multilayer (muscle, skin, fat)	-----	-----
[92]	Slot antenna	0.915	-----	Chicken breast tissue	Full-wave cross-coupled bridge rectifier	1 V / 50 μW DC
[93]	Meandered antenna with feeding loop	2.45	18×11×8.5	-----	A bridge rectifier (Avago HSMS-2828)	2.6 V / 250 μW

4. PRELIMINARY INVESTIGATIONS ON USING SPLIT RINGS TO MAXIMIZE THE POWER RECEIVED BY RECTENNAS IN LOSSY MEDIA

In this section, it is demonstrated that a layer inspired by split ring resonators (SRR) around a receiving antenna at the rectenna front inside a lossy conducting medium can improve the power received by this antenna. This has been indicated by the increase of the transmission coefficient between an external antenna in free space and the receiving antenna in the conducting lossy medium when the SRR-based layer is used. In general, the power received by an antenna at the rectenna front inside a conducting lossy medium can be increased if:

1. The antenna gain in the conducting medium (G_{con}) increases. This can be obtained by increasing the magnitude of the magnetic field $|H|$ (A/m):

$$G_{con} = \frac{4\pi \sqrt{(\omega\mu/2\sigma)} (|H|de^{(d/\delta)})^2}{R_r(i_i)^2}; \quad (11)$$

where d (m) is the distance at which $|H|$ is taken or measured, δ (m) is the skin depth, R_r (Ω) is the radiation resistance and i_i (A) is the input current [94].

2. The power loss due to power absorption decreases. This can be obtained if the electric near field intensity around the antenna decreases as explained in some previous sections of this paper.

Both of magnetic and electric fields around the antenna can be controlled by metamaterials or structures inspired by metamaterials (which may not lead to the same properties of metamaterials) [95-97]. Therefore, a layer inspired by split-ring-resonators is designed and used around a loop antenna inside a lossy medium. The antenna and layer structures are shown in Figure 8. The antenna and layer are optimized using CST Microwave studio [61] in a model of a lossy conducting medium to work for the 2.45 GHz Industrial, Scientific and Medical (ISM) band for $S_{11} < -10$ dB. The lossy medium is simulated with a conductivity of 1.74 S/m and a permittivity of around 52, which resemble the dielectric properties of the human muscle at 2.45 GHz [26]. It is worth indicating that this section aims

to show the advantages of using SRR layer for WPT in lossy media and not to optimize the design for maximum power transfer.

The power transfer from an external meandered loop antenna to the proposed antenna with and without the SRR-based layer inside the conducting lossy model is set at a distance of 0.5 m and the transmission coefficient is simulated at this distance at a frequency of 2.45 GHz. The simulated antenna gain and transmission coefficient are found to be larger by 2.7 dB when the SRR-based layer is used. This is because the SRR-based layer served to increase the magnetic near field by 20% and reduce the electric near field by 40% in comparison with the case when no SRR layer is used. This increases the power at the rectenna front as discussed above.

A phantom of lossy medium was prepared by adding salt and sugar to water to control its conductivity and permittivity, respectively. Salt and sugar were added gradually until an effective permittivity of around 52 and a conductivity of 1.74 S/m were obtained and measured using Agilent 85070E Dielectric Probe [98].

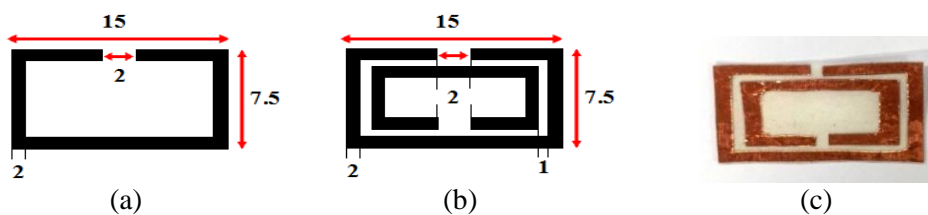


Figure 8. A layout structure of the: (a) antenna (b) SRR-based layer (c) fabricated SRR-based layer; units in (mm).

The antenna (with and without the SRR layer) is wrapped around a cylinder and fed by a coaxial cable that is isolated from the lossy medium to provide accurate measurement results. The measurement setup is shown in Figure 9. The simulated and measured reflection coefficients are shown in Figure 10. The transmission coefficient between the antenna inside the lossy phantom and the external loop antenna at 0.5 m and 2.45 GHz was measured. 2.5 dB increase in the transmission coefficient and gain is measured which is in good agreement with the simulated results.

5. CONCLUSIONS

WPT has many beneficial applications in different media and thus has gained a wide interest. The development of efficient WPT systems require great and comprehensive efforts to overcome the current limitations and challenges of WPT. Different techniques and approaches were proposed to boost WPT in different media which have been discussed in this paper. There are, however, still many unsolved issues and challenges to solve and overcome.

While the option of multiple coils (overlapped, in linear array, stacked in parallel) has helped in increasing the power transfer range, mobility of the receiver coil and number of powered receivers in the ICPT system, it increases the system weight, size and profile. This might be not optimum for most of the recent wireless communication devices which are preferred to be small in size and light in weight. A good way to overcome the limitations of some of the multiple coil designs is to use printed or flexible coils. Therefore, further investigations on the effect of the flexible coil structure on the coil parameters and overall performance are needed. The bending effect of the flexible coil on the ICPT should be also studied. This also applies to ICPT for implantable applications, where printed or flexible coils are much more practical. For underwater applications, the option of using larger and multiple coils is viable as size and weight restrictions are less. However, coil parameters underwater should be derived for this case. Most of the proposed designs were tested in free space, which does not guarantee the actual validation of them underwater. The overall losses should be also quantified for such systems. Frequency splitting elimination techniques, such as using non-identical coils and frequency tracking techniques, increase the ICPT system complexity and consumed power and require further investigations regarding the system stability and optimized parameters.

Metamaterials have been used to increase the power transfer efficiency of ICPT systems. However, rigid structures between coils were mostly utilized. Future designs may utilize metamaterial-based

coils which can yield the same performance without adding extra layers. Coils based on flexible metamaterials could be also utilized.



Figure 9. Measurement setup.

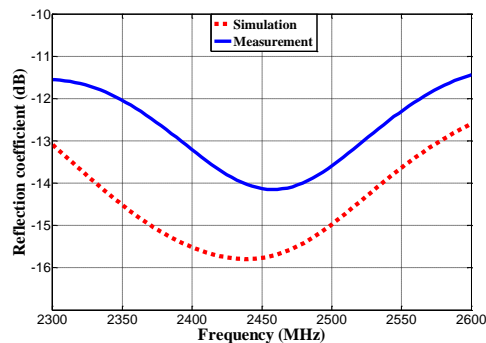


Figure 10. Simulated and measured reflection coefficients of a loop antenna with SRR-based layer for the 2.45 GHz ISM band.

Table 5. The simulated transmission coefficient (dB) and realized gain (dBi) of the receiving antenna in a conducting lossy medium with and without the SRR based layer.

	Transmission coefficient (dB)	Realized gain (dBi)
With SRR	-40	-27
Without SRR	-42.7	-29.7

For MPT, different rectenna designs were proposed. In general, miniaturized rectennas of wide or broad bandwidth are required for efficient and stable MPT. For applications where power limitations are not very restricted, rectennas based on MIMO and antenna arrays should be further investigated and designed. For the rectifier circuit, smart designs are still needed. In both of the human body and underwater media, the MPT channel should be carefully characterized which is very challenging considering that the human body and sea water are time-variant and their characteristics are affected by many factors such as the temperature. New functionalities of split rings for MPT in lossy media have been indicated in this paper. It has been shown that structures inspired by SRR can increase the received power at the front edge (input) of the rectenna in a lossy conducting medium (by 2.5 dB or larger for the case discussed in this paper). Further designs inspired by metamaterials or split rings to boost MPT especially in lossy media could be a hot research area for future investigations.

REFERENCES

- [1] J. Zhang, Rectennas for RF Wireless Energy Harvesting, Ph.D. dissertation, Dept. Elect. Eng., University of Liverpool, Liverpool, UK, 2013.
- [2] Wikipedia.org, "Wireless Power Transfer," [Online], Available: https://en.wikipedia.org/wiki/Wireless_power_transfer.
- [3] Wikipedia.org, "Wireless Power Transfer," [Online], Available: https://en.wikipedia.org/wiki/Tesla_coil.
- [4] N. Shinohara, Wireless Power Transfer via Radiowaves, New Jersey: John Wiley & Sons, Inc., 2014.
- [5] W. Hayt and J. Buck, Engineering Electromagnetics, USA, New York: McGraw-Hill, 2012.

- [6] H. Sugiyama, "Performance Analysis of Magnetic Resonant System Based on Electrical Circuit Theory," in: Tech., pp. 95-116, Jan. 2012.
- [7] ICNIRP Guidelines for Limiting Exposure to Time-Varying Electric, Magnetic and Electromagnetic Fields (up to 300 GHz), Health Physics, vol. 74, no. 4, pp. 494-522, 1998.
- [8] M. A. Hassan and A. Elzawawi, "Wireless Power Transfer through Inductive Coupling," Proc. of 19th International Conference on Circuits (part of CSCC '15), pp.115-118, 2015.
- [9] D. M. Pozar, Microwave Engineering, USA, New Jersey, John Wiley & Sons, Inc., 2015.
- [10] M. Kesler, "Highly Resonant Wireless Power Transfer: Safe, Efficient and over Distance," Witricity Corporation-White Paper, pp. 1-13, 2017.
- [11] X. Mou and H. Sun, "Wireless Power Transfer: Survey and Roadmap," Proc. of 81st Vehicular Technology Conference (VTC2015- Spring), pp. 1-13, 2015.
- [12] M. Biswal, P. Sharma, N. Shete, S. Sokande and P. Tayade, "Study and Survey of Wireless Charging Technologies," International Journal of Advanced Research in Computer Engineering & Technology (IJARCET), vol. 5, no. 5, pp. 1450–1453, May 2016.
- [13] L. M. M. Tan, Efficient Rectenna Design for Wireless Power Transmission for MAV Applications, Master thesis, Dept. Elect. and Computer Eng., Naval Postgraduate School, California, Dec. 2005.
- [14] C-H. Hung, Design and Development of Wireless Power Transmission for Unmanned Air Vehicles, Master thesis, Dept. Elect. and Computer Eng., Naval Postgraduate School, California, Sep. 2012.
- [15] Antenna-theory.com, "The Friis Equation," [Online], Available: <http://www.antenna-theory.com/basics/friis.php>.
- [16] Y. Huang and K. Boyle, Antennas from Theory to Practice, UK, John Wiley & Sons, Ltd., 2008.
- [17] R. Mehrotra, "Cut the Cord: Wireless Power Transfer, Its Applications and Its Limits," pp. 1-11. 2014, [Online], Available: <http://www.cse.wustl.edu/~jain/cse574-14/ftp/power.pdf>, [Accessed: 5- May-2014].
- [18] M. K. Hosain *et al.*, "Development of a Compact Rectenna for Wireless Powering of a Head-Mountable Deep Brain Stimulation Device," IEEE Journal of Translational Engineering in Health and Medicine, vol. 2, pp. 1-13, 2014.
- [19] L. Summerer and O. Purcell, "Concepts for Wireless Energy Transmission via Laser," [Online], Available: <http://www.esa.int/gsp/ACT/doc/POW/ACT-RPR-NRG-2009-SPS-ICSOS-concepts-for-laser-WPT.pdf>.
- [20] A. W. Bett, F. Dimroth, R. Lockenhoff, E. Oliva and J. Schubert, "III–V Solar Cells under Monochromatic Illumination," Proc. of 33rd IEEE Photovoltaic Specialists Conference, pp. 1-5, 2008.
- [21] A. Yakovlev, S. Kim and A. Poon, "Implantable Biomedical Devices: Wireless Powering and Communication," IEEE Communications Magazine, vol. 50, no. 4, pp. 152-159, April 2012.
- [22] N. W. Bergmann, J. Juergens, L. Hou, Y. Wang and J. Trevathan, "Wireless Underwater Power and Data Transfer," Proc. of 38th Annual IEEE Conference on Local Computer Networks- Workshops, pp. 104-107, 2013.
- [23] E. A. Karagianni, "Electromagnetic Waves under Sea: Bow-Tie Antenna Design for Wi-Fi Underwater Communications," Progress in Electromagnetics Research M, vol. 41, pp. 189–198, 2015.
- [24] W. Dargie and C. Poellabauer, Fundamentals of Wireless Sensor Networks: Theory and Practice, USA, New Jersey, John Wiley and Sons, Ltd., 2010.
- [25] C. M. Nguyen *et al.*, "Wireless Power Transfer for Autonomous Wearable Neurotransmitter Sensors," Sensors, vol. 15, no. 9, pp. 24553-24572, Sep. 2015, doi:10.3390/s150924553.
- [26] F. Merli, Implantable Antennas for Biomedical Applications, Ph.D. dissertation, Dept. Elect. Eng., EPFL Univ., Lausanne, Switzerland, 2011.
- [27] R. W. P. King and G. S. Smith, Antennas in Matter: Fundamentals, Theory and Applications, Cambridge, Mass: MIT Press, 1981.
- [28] Allaboutcircuits.com, "Factors Affecting Inductance," [Online], Available: <http://www.allaboutcircuits.com/textbook/direct-current/chpt-15/factors-affecting-inductance/>.

- [29] IEEE Standard for Safety Levels with Respect to Human Exposure to Radio Frequency Electromagnetic Fields, 3 kHz to 300 GHz, IEEE Standard C95.1-1999, 1999.
- [30] IEEE Standard for Safety Levels with Respect to Human Exposure to Radio Frequency Electromagnetic Fields, 3 kHz to 300 GHz, IEEE Standard C95.1-2005, 2005.
- [31] M. D. Basar, M. Ahmad, J. Cho and F. Ibrahim, "Application of Wireless Power Transmission Systems in Wireless Capsule Endoscopy: An Overview," *Sensors*, vol. 14, no. 6, pp. 10929–10951, Jun. 2014, doi: 10.3390/s140610929.
- [32] M. Fareq, M. Fitra, M. Irwanto, S. Hasan and M. Arinal, "Low Wireless Power Transfer Using Inductive Coupling for Mobile Phone Charger," *Journal of Physics: Conference Series* 495, pp. 1-7, 2014, doi:10.1088/1742-6596/495/1/012019.
- [33] K. A. Kalwar, M. Aamir and S. Mekhilef, "Inductively Coupled Power Transfer (ICPT) for Electric Vehicle Charging – A Review," *Renew. and Sustainable Energy Reviews*, vol. 47, pp. 462–475, 2015.
- [34] Wikipedia.org, "Resonant Inductive coupling," [Online], Available: https://en.wikipedia.org/wiki/Resonant_inductive_coupling.
- [35] C. Reinhold, P. Scholz, W. John and U. Hilleringmann, "Efficient Antenna Design of Inductive Coupled RFID-Systems with High Power Demand," *Journal of Communications*, vol. 2, no. 6, pp. 14-23, Nov. 2007.
- [36] Wirelesspowerconsortium, "Magnetic Resonance and Magnetic Induction," [Online], Available: <https://www.wirelesspowerconsortium.com/technology/magnetic-resonance-and-magnetic-induction-making-the-right-choice-for-your-application.html>.
- [37] B. Wang, K. H. Teo, S. Yamaguchi, T. Takahashi and Y. Konishi, "Flexible and Mobile Near-Field Wireless Power Transfer Using an Array of Resonators", *WPT*, pp.73-77, Oct. 2010.
- [38] S. Han and D. D. Wentzloff, "Wireless Power Transfer Using Resonant Inductive Coupling for 3D Integrated ICs," 2010 IEEE International 3D Systems Integration Conference (3DIC), pp. 1-5, 2010.
- [39] B. Wang, T. Nishino and K. H. Teo, "Wireless Power Transmission Efficiency Enhancement with Metamaterials," *Proc. of the IEEE International Conference on Wireless Information Technology and Systems*, pp. 1-4, 2010.
- [40] B. Wang, K. H. Teo, T. Nishino, W. Yezazunis, J. Barnwell and J. Zhang, "Wireless Power Transfer with Metamaterials," *Proc. of the 5th European Conference on Antennas and Propagation (EUCAP)*, pp. 3905-3908, 2011.
- [41] A. Rajagopalan, A. K. RamRakhyani, D. Schurig and G. Lazzi, "Improving Power Transfer Efficiency of a Short-Range Telemetry System Using Compact Metamaterials," *IEEE Transactions on Microwave Theory and Techniques*, vol. 62, no. 4, pp. 947-955, April 2014.
- [42] A. P. Sample, D. T. Meyer and J. R. Smith, "Analysis, Experimental Results and Range Adaptation of Magnetically Coupled Resonators for Wireless Power Transfer," *IEEE Transactions on Industrial Electronics*, vol. 58, no. 2, pp. 544-554, Feb. 2011.
- [43] J. Park, Y. Tak, Y. Kim, Y. Kim and S. Nam, "Investigation of Adaptive Matching Methods for Near-Field Wireless Power Transfer," *IEEE Transactions on Antennas and Propagation*, vol. 59, no. 5, pp. 1769-1773, May 2011.
- [44] W. Q. Niu, J. X. Chu, W. Gu and A. D. Shen, "Exact Analysis of Frequency Splitting Phenomena of Contactless Power Transfer Systems," *IEEE Transactions on Circuits and Systems I: Regular Papers*, vol. 60, no. 6, pp. 1670-1677, June 2013.
- [45] N. Y. Kim *et al.*, "Automated Adaptive Frequency Tracking System for Efficient Mid-Range Wireless Power Transfer via Magnetic Resonance Coupling," *Proc. of the 42nd European Microwave Conference*, pp. 221-224, 2012.
- [46] M. Schormans, V. Valente and A. Demosthenous, "Frequency Splitting Analysis and Compensation Method for Inductive Wireless Powering of Implantable Biosensors", *Sensors*, vol. 16, no. 8, pp. 1-14, Aug. 2016.
- [47] W. S. Lee, W. I. Son, K. S. Oh and J. W. Yu, "Contactless Energy Transfer Systems Using Antiparallel Resonant Loops," *IEEE Transactions on Industrial Electronics*, vol. 60, no. 1, pp. 350-359, Jan. 2013.
- [48] Y. L. Lyu *et al.*, "A Method of Using Nonidentical Resonant Coils for Frequency Splitting Elimination in Wireless Power Transfer," *IEEE Trans. on Power Electronics*, vol. 30, no. 11, pp. 6097-6107, 2015.

- [49] J-G. Shi, D-J. Li and C-J. Yang, "Design and Analysis of an Underwater Inductive Coupling Power Transfer System for Autonomous Underwater Vehicle Docking Applications," *Journal of Zhejiang University-SCIENCE C*, vol. 15, no. 1, pp. 51-62, Jan. 2014
- [50] V. Bana, G. Anderson, L. Xu, D. Rodriguez, A. Phipps and J. D. Rockway, "Characterization of Coupled Coil in Seawater for Wireless Power Transfer," *Technical Report 2026*, pp. 1-18, Sep. 2013.
- [51] M. Kesler, "Highly Resonant Wireless Power Transfer in Subsea Applications," *Colin McCarthy WiTricity Corporation*, [Online], Available: <http://www.witricity.com/assets/HRWPT-in-Subsea-Applications.pdf>.
- [52] M. Ryu, J. D. Kim, H. U. Chin, J. Kim and S. Y. Song, "Three-Dimensional Power Receiver for in Vivo Robotic Capsules," *Medical and Biological Engineering and Computing*, vol. 45, no.10, pp. 997–1002, Oct. 2007.
- [53] J. Gao, G. Yan, Z. Wang, P. Jiang and D. Liu, "A Capsule Robot Powered by Wireless Power Transmission: Design of Its Receiving Coil," *Sensors and Actuators A: Physical*, vol. 234, pp. 133-142, Oct. 2015.
- [54] R. Carta, R. J. Thone' and R. Puers, "A Wireless Power Supply System for Robotic Capsular Endoscopes," *Sensors and Actuators A: Physical*, vol.162, no. 2, pp. 177–183, Aug. 2010.
- [55] R. Carta, J. Thone and R. Puers, "A 3D Ferrite Coil Receiver for Wireless Power Supply of Endoscopic Capsules," *Procedia Chemistry*, vol. 1, no. 1, pp. 477–480, Sep. 2009.
- [56] J. Zhiwei, Y. Guozheng, J. Pingping, W. Zhiwu and L. Hua, "Efficiency Optimization of Wireless Power Transmission Systems for Active Capsule Endoscopes," *Physiological Measurement*, vol. 32, no. 10, pp. 1561–1573, Aug. 2011.
- [57] Y. Huang *et al.*, "An Efficiency-Enhanced Wireless Power Transfer System with Segmented Transmitting Coils for Endoscopic Capsule," *Proc. of the IEEE International Symposium on Circuits and Systems (ISCAS2013)*, pp. 2279-2282, 2013.
- [58] R. Beiranvand, "Analyzing the Uniformity of the Generated Magnetic Field by a Practical One-Dimensional Helmholtz Coils System," *Review of Scientific Instruments*, vol. 84, no. 7, 2013.
- [59] N. Vidal, S. Courto, J. M. Lopez Villegas, J. Siero and F.M. Ramos, "Detuning Study of Implantable Antennas Inside the Human Body," *Progress in Electromagnetics Research (PIER)*, vol. 124, pp. 265-283, 2012.
- [60] Virtual Medical Centre, "Wireless Capsule Enteroscopy Capsule Endoscopy," [Online], Available: <https://www.myvmc.com/investigations/wireless-capsule-enteroscopy-capsule-endoscopy-pill-cam/>.
- [61] Computer Simulation Technology, [Online], Available: <http://www.CST.com>.
- [62] J. Hartford, *Wireless Power for Medical Devices*, *Electronic Components*, 2013, [Online], Available: <http://www.mddionline.com/article/wireless-power-medical-devices>.
- [63] A. E. Czarnecki, *Efficient Inductively Coupled Resonant Power Transfer for an Implantable Electroencephalography Recording Device*, Master thesis, Dept. Elect. Comp. Eng., Northeastern University, Boston, Massachusetts, July 2012.
- [64] X. Li *et al.*, "A Wireless Magnetic Resonance Energy Transfer System for Micro Implantable Medical Sensors," *Sensors*, vol. 12, no. 8, pp. 10292-10308, July 2012.
- [65] U-M. Jow and M. Ghovanloo, "Design and Optimization of Printed Spiral Coils for Efficient Transcutaneous Inductive Power Transmission," *Proc. of the IEEE Transactions on Biomedical Circuits and Systems*, vol. 1, no. 3, pp. 193-202, Sept. 2007.
- [66] A. Usman, J. Bitto and M. M. Tentzeris, "Flexible & Planar Implantable Resonant Coils for Wireless Power Transfer Using Inkjet Masking Technique," *Proc. of the IEEE Topical Conference on Biomedical Wireless Technologies, Networks and Sensing Systems (BioWireleSS)*, pp. 97-99, 2016.
- [67] F. Zhang *et al.*, "Design of a Compact Planar Rectenna for Wireless Power Transfer in the ISM Band," *International Journal of Antennas and Propagation*, pp. 1-9, Feb. 2014.
- [68] M. I. Anju, R. Siva, S. Abisha, V. Nandhini and R. Priya, "A Linearly Polarized Rectenna for Far-Field Wireless Power Transfer," *International Journal of Advanced Research in Electrical, Electronics and Instrumentation Engineering*, vol. 4, no. 3, March 2015.

- [69] R. Tanaka, H. Sakaki, M. Kuroki, F. Kuroiwa and K. Nishikawa, "Wide Dynamic Range Rectifier with Adaptive Power Control Technique," Asian Wireless Power Transfer Workshop, pp. 1-6, Feb. 2015.
- [70] O. Ramahi, "Metasurfaces for Far-Field Wireless Power Transfer and Energy Harvesting," Proc. of Qatar Foundation Annual Research Conference, 2016: EEPP3120 <http://dx.doi.org/10.5339/qfarc.2016.EEPP3120>.
- [71] M. Abu, M. S. A. Jamil Kher, N. H. Izahar, A. F. Ab. Latif and S. N. Zabri, "Enhancement of Rectenna Performance Using Artificial Magnetic Conductor for Energy Harvesting Applications," Journal of Telecommunication, Electronic and Computer Engineering (JTEC), vol. 7, no. 2, pp. 77-82, Dec. 2015.
- [72] J-S. Sun, R-H. Chen, S-K. Liu and C-F. Yang, "Wireless Power Transmission with Circularly Polarized Rectenna," Microwave Journal, pp. 1-15, Jan. 2011.
- [73] D-Y. Choi, S. Shrestha, J-J. Park and S-K. Noh, "Design and Performance of an Efficient Rectenna Incorporating a Fractal Structure," International Journal of Communication Systems, vol. 27, no. 4, pp. 661-679, April 2014.
- [74] G. Andia Vera, A. Georgiadis, A. Collado and S. Via, "Design of a 2.45 GHz Rectenna for Electromagnetic (EM) Energy Scavenging," Proc. of the IEEE Radio and Wireless Symposium (RWS), pp. 61-64, 2010.
- [75] S. Shrestha, S-K. Noh and D-Y. Choi, "Comparative Study of Antenna Designs for RF Energy Harvesting," International Journal of Antennas and Propagation, pp.1-10, Jan. 2013.
- [76] S. Keyrouz and H. Visser, "Efficient Direct-Matching Rectenna Design for RF Power Transfer Applications," Journal of Physics: Conference Series, pp.1-5, 2013.
- [77] J-W. Zhang, Y. Huang and P. Cao, "An Investigation of Wideband Rectennas for Wireless Energy Harvesting", Wireless Engineering and Technology, pp. 107-116, Aug. 2014.
- [78] M. A. Sennouni, J. Zbitou, A. Benaissa, A. Tribak, O. Elmrabet and M. Latrach, "Development of a New Slit-Slotted Shaped Microstrip Antenna Array for Rectenna Application," Journal of Emerging Technologies in Web Intelligence, vol. 6, no. 1, pp. 49-53, Feb. 2014.
- [79] F. Mohammad and M. Saed, "A Retrodirective Array with Reduced Surface Waves for Wireless Power Transfer Applications," Progress in Electromagnetics Research C, vol. 55, pp. 179–186, 2014.
- [80] D. Arnitz and M. S. Reynolds, "MIMO Wireless Power Transfer for Mobile Devices," Proc. of the IEEE Pervasive Computing, vol. 15, no. 4, pp. 36-44, 2016.
- [81] Y-Y. Gao, X-X. Yang, C. Jiang and J-Y. Zhou, "A Circularly Polarized Rectenna with Low Profile for Wireless Power Transmission," Progress in Electromag. Research Letters, vol. 13, pp. 41–49, 2010.
- [82] Z. Harouni, L. Cirio, L. Osman, A. Gharsallah and O. Picon, "A Dual Circularly Polarized 2.45-GHz Rectenna for Wireless Power Transmission," Proc. of the IEEE Antennas and Wireless Propagation Letters, vol. 10, pp. 306-309, 2011.
- [83] Z. Harouni, L. Osman and A. Gharsallah, "Efficient 2.45 GHz Rectenna Design with High Harmonic Rejection for Wireless Power Transmission," IJCSI, vol. 7, no. 5, Sep. 2010.
- [84] Y. Xu, S. Gong and Y. Guan, "Coaxially Fed Microstrip Antenna for Harmonic Suppression," Electronics Letters, vol. 48, no. 15, pp. 895-896, July 2012.
- [85] J. Ahn, W. Lee, Y. Yoon and Y-D. Kim, "Planar Inverted F-antenna with Suppressed Harmonics," Proc. of the Asia-Pacific Microwave Conference, pp. 1-4, 2008.
- [86] J. Yeo and D. Kim, "Harmonic Suppression Characteristic of a CPW-Fed Circular Slot Antenna Using Single Slot on a Ground Conductor," Progress in Electromag. Research Lett., vol. 11, pp. 11–19, 2009.
- [87] S. M. Asif and B. D. Braaten, "Design of a Compact Implantable Rectenna for Wireless Pacing Applications," Proc. of the IEEE International Symposium on Antennas and Propagation (APSURSI), pp. 167-168, 2016.
- [88] R. S. Alrawashdeh, Y. Huang, M. Kod and A. Sajak, "A Broadband Flexible Implantable Loop Antenna with Complementary Split Ring Resonators," Proc. of the IEEE Antennas and Wireless Propagation Letters, vol. 14, pp. 1506 – 1509, Feb. 2015.
- [89] T. Kumagai, K. Saito, M. Takahashi and K. Ito, "A 430MHz Band Receiving Antenna for Microwave Power Transmission to Capsular Endoscope," Proc. of the IEEE URSI General Assembly and Scientific Symposium, pp. 1-4, 2011.

- [90] M. K. Kumar, S. Rajkumar and J. J. Paul, "Miniaturized Planar Inverted F Antenna for Tri-Band Bio-Telemetry Communications," International Journal of Scientific & Engineering Research, vol. 4, no. 5, pp. 982-987, May 2013.
- [91] F. Gozasht and A. S. Mohan, "Miniaturized Slot PIFA Antenna for Triple Band Implantable Biomedical Applications," Proc. of the IEEE MTT-S International Microwave Workshop Series on RF and Wireless Technologies for Biomedical and Healthcare Applications (IMWS-BIO), pp. 1-3, 2013.
- [92] A. Y. S. Jou, H. Pajouhi, R. Azadegan and S. Mohammadi, "A CMOS Integrated Rectenna for Implantable Applications," Proc. of the IEEE MTT-S Int. Microwave Symposium (IMS), pp. 1-3, 2016.
- [93] O. Kazanc, G. Yilmaz, F. Maloberti and C. Dehollain, "Remote Powering Platform for Implantable Sensor Systems at 2.45 GHz," Proc. of the 36th IEEE Annual International Conference of the Engineering in Medicine and Biology Society (EMBC), pp. 2028-2031, 2014.
- [94] R. Moore, "Effects of a Surrounding Conducting Medium on Antenna Analysis," Proc. of the IEEE Transactions on Antennas and Propagation, vol. 11, no. 3, pp. 216-225, May 1963.
- [95] JB. Pendry, "Metamaterials and the Control of Electromagnetic Fields," [Online], Available: <http://www.cmth.ph.ic.ac.uk/photonics/Newphotonics/pdf/RochPaper.pdf>.
- [96] R. Marque's, F. Martin and M. Sorolla, Metamaterials with Negative Parameters: Theory, Design and Microwave Applications, Hoboken, New Jersey, USA, Wiley & Sons, Ltd., 2008.
- [97] C. Calos and T. Itoh, Electromagnetic Metamaterials: Transmission Line Theory and Microwave Applications, Hoboken, New Jersey, USA, Wiley & Sons, Ltd., 2005.
- [98] Agilent 85070E Dielectric Probe Kit Printed Version of 85070E Help File, 2013, [Online], Available: <http://na.support.keysight.com/materials/help/85070.pdf>, [Accessed: 16- July- 2013].

ملخص البحث:

ازداد في الآونة الأخيرة الاهتمام بالنقل اللاسلكي للقدرة بشكل ملحوظ، نظراً لتطبيقاته الجذابة. والجدير بالذكر أن فعالية نقل القدرة ومدى الاتصال لغالبية أنظمة النقل اللاسلكي للقدرة لا يزالان محدودين، وذلك بسبب العديد من التحديات التقنية والتحديات المتعلقة بالتنظيم. وهذا يتطلب المزيد من البحث والجهود التقنية للتغلب على التحديات الراهنة وجعل أنظمة النقل اللاسلكي للقدرة أكبر فعالية وأوسع استخداماً.

تهدف هذه الورقة إلى مراجعة أوجه التقدم الأخيرة وتقدم البحث في مجال النقل اللاسلكي للقدرة لأغراض التصدي للتحديات الراهنة وتحديد اتجاهات البحث المستقبلي. ولتحقيق هذه الأغراض، تقدم هذه الورقة مدخلاً إلى النقل اللاسلكي للقدرة. هذا إضافة إلى مناقشة القضايا البحثية الرئيسية المرتبطة بالنقل اللاسلكي للقدرة في الفضاء الحر وفي الأوساط التي يحدث فيها فقد للقدرة. من ناحية أخرى، يجري استقصاء فوائده استخدام دارات الرنين منفصلة الحلقات في النقل اللاسلكي للقدرة في الأوساط الموصلة التي يحدث فيها فقد للقدرة. وهذا من شأنه أن يساعد كثيراً في تعزيز النقل اللاسلكي للقدرة في الأوساط التي يحدث فيها فقد للقدرة، وأن يكون مصدر إلهام للحصول على بنى أقرب إلى المثالية من أجل مزيد من التحسين.

ADJACENT CHANNEL INTERFERENCE REDUCTION IN OFDM SYSTEMS

Arwa Waleed Mustafa¹ and Khalid G. Samarah²

(Received: 01-May-2017, Revised: 03-Jul.-2017, Accepted: 19-Jul.-2017)

ABSTRACT

Orthogonal frequency division multiplexing (OFDM) is a promising candidate for cognitive radio transmission. OFDM supports high data rates that are robust to channel impairments. However, one of the biggest problems for OFDM transmission is high out-of-band radiation, which results from the sidelobes of the OFDM sub-carriers. These sidelobes are a source of interference to neighbouring transmissions. This paper focuses on reducing out-of-band radiation by reading and extracting the radiation power in the sidelobes. This is done by extending the time domain OFDM signal by zeros in both sides. The resulting signal is then transformed to the time domain and extended samples are removed to obtain the N -samples of time domain signal representing the out-of-band radiated signal. The resulting signal is Fourier transformed and high frequency sub-carriers are removed to obtain pilots that are inverted and added to the original OFDM data sub-carriers, resulting in reducing the Adjacent Channel Interference (ACI), which affects the adjacent systems. The added signal represents a noise signal to the desired OFDM signal that reduces the BER performance of the desired system, thus a weighing factor is applied to the added signal in order to get a better BER performance with good out-of-band radiation reduction.

Matlab/Simulink simulation is adopted to perform an assessment of the proposed technique with different weighing factors and different frequency separation between the desired signal and the adjacent one. For 0 dB attenuation on the added signal, a 10 dB reduction in out-of-band radiation is obtained, while 6 dB reduction is obtained when the weighing factor reduces the input signal power by 3 dB. BER performance is better by performing the reduction technique and depends on the frequency distance between the adjacent signal and the desired one.

KEYWORDS

OFDM, Out-of-band Radiation, Adjacent Channel Interference (ACI), Matlab/Simulink Simulation.

1. INTRODUCTION

In wireless communications, because of the nature of the propagation channel, adjacent signals in frequency are subject to be affected by interference that reduces their performance as well as increases the BER (Bit Error Rate) of the system. Therefore, to improve the system performance, wireless communication systems have to decrease the effect of interference. The wireless communication system is regulated in using the frequency spectrum by several institutes, like the ITU (International Telecommunication Union), where regulations are done over long areas and periods, whereas spectrum is accessed locally and over short periods [1]-[2].

Adjacent Channel Interference (ACI) is one of several types of interference discussed in this paper. It occurs between the signals that are close in frequency and due to several reasons that will be discussed later. As such, ACI helps engineers in deciding how the frequency bands may be allocated to different wireless communication systems.

Adjacent Channel Interference (ACI) results from adjacent systems with out-of-band radiation equal to the desired system frequency. This interference can be minimized using a strictly restricted signal bandwidth or a proper channel assignment [3]-[4].

The ACI is created by two effects:

1. The transmitter radiation due to the type of modulator and different hardware properties of the used devices extended over a larger frequency range. This out-of-band radiation is not completely suppressed, since the transmit filters are not ideal. This will affect the receiver with receiving unwanted power from the adjacent signals that are not perfectly filtered.

1. A. W. Mustafa is with Electrical Engineering Department, Mutah University, Alkarak, Jordan. Email: arwa_wr@yahoo.co.uk.

2. Kh. G. Samarah is with Electrical Engineering Department, Mutah University, Alkarak, Jordan. Email: kgsamarah@mutah.edu.jo

- At the receiver, the radiation from the desired channel is suppressed insufficiently by the receiver filter. Thus, some of the signal in the adjacent channel is passed onto the demodulator, where it acts as interference.

The main definition for ACI is that it is a power leakage from neighboring channels that introduce energy reception in the desired frequency band from the unwanted frequency. ACI limits the capacity and decreases the performance of the wireless system [5]. ACI is enhanced if the adjacent channel user is transmitting in a close range (as cellular systems) compared to the receiver while the receiver is trying to receive a BS (base station) signal on the channel. This is called near-far effect, as depicted in Figure 1. This effect can also occur if a mobile close to a base station transmits on a channel close to one being used by another mobile station has weak signal power due to its far position to BS. This problem also might occur if the base station has a problem in distinguishing the mobile user from the interference signal caused by the close adjacent channel mobile [6]-[7].

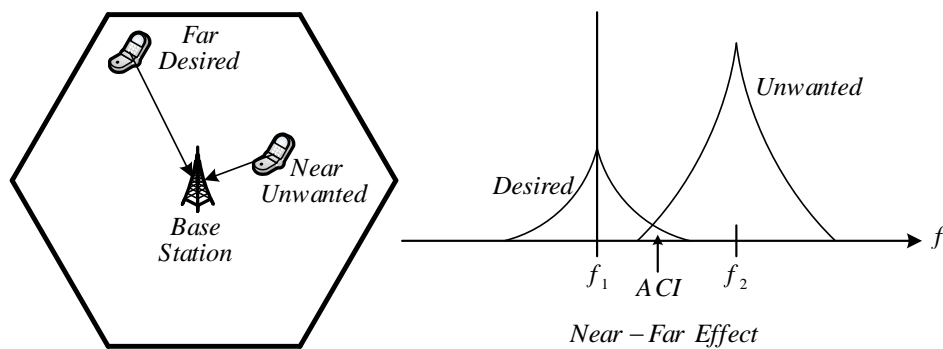


Figure 1. Near-far effect.

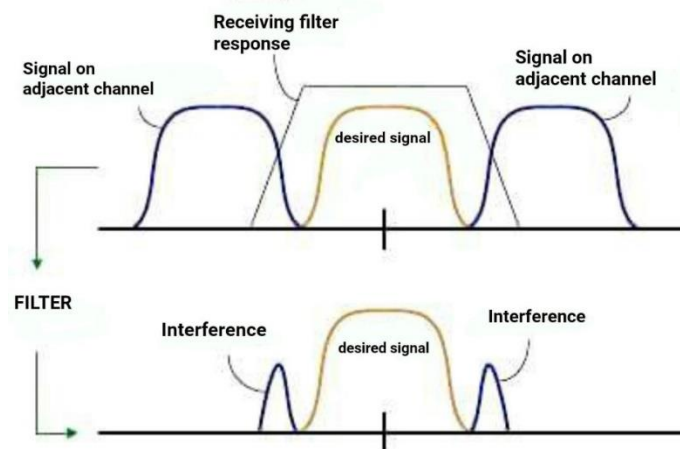


Figure 2. Imperfect receiver filtering develops ACI.

In the receiver side, additional interference from the adjacent channel will occur, since the receiver filter cannot be ideal, not completely rectangular, as in Figure 2 above. The filter will have sidelobes in the adjacent channel, causing the power from the main lobe of the transmitted interference source to affect receiver performance [8].

2. OFDM SYSTEMS

Orthogonal frequency division multiplexing (OFDM) is a technology that splits the wide band channel into smaller frequency bands called sub-carriers. These sub-carriers have to be lower than the coherent bandwidth of the multi-path propagation channel, which will convert the frequency selective fading that may affect the whole band into flat fading on each sub-carrier [9]-[11].

At the same time, OFDM converts the high data rate stream into N_d data streams (symbols). Zero padding is presented to introduce a guard band to the left and right of the frequency sub-carriers and prevent the OFDM signal from aliasing and increasing the resolution in time. The resulting

$N = N_d + N_z$ symbols modulate the frequency sub-carriers using the inverse Fourier transform. Mathematically, The k^{th} sub-carrier of the OFDM signal is described by the sinusoidal basis functions $e^{j2\pi k f_{sc} t}$. The OFDM signal is given by:

$$s(t) = \frac{1}{N} \sum_{k=-N/2}^{N/2-1} S_k e^{j2\pi k f_{sc} t} p(t), \quad k = -N/2 : N/2 - 1$$

$$p(t) = \text{rect}\left(\frac{t - T_u/2}{T_u}\right)$$
(1)

A rectangular pulse shaping filter, $p(t)$, is applied for each sub-carrier in the time domain, where f_{sc} is the sub-carrier frequency spacing, while T_u is the width of the rectangular pulse shaping filter (also called the OFDM useful symbol duration) [12]. OFDM signal given by Equation (1) can be Fourier transformed into the frequency domain by the following analysis:

$$s(t) = \frac{1}{N} \sum_{k=-N/2}^{N/2-1} S_k e^{j2\pi k f_{sc} t} p(t)$$

$$\text{fft}\{s(t)\} = \text{fft}\left\{\frac{1}{N} \sum_{k=-N/2}^{N/2-1} S_k e^{j2\pi k f_{sc} t} p(t)\right\}$$

$$S(f) = \text{fft}\{p(t)\} * \text{fft}\left\{\frac{1}{N} \sum_{k=-N/2}^{N/2-1} S_k e^{j2\pi k f_{sc} t}\right\}$$
(2)

The Fourier transform of two multiplied functions is the convolution between the Fourier transform of each function alone, where the symbol $\{*\}$ represents the convolution process [13]-[16]. OFDM signal representation in the frequency domain is given as follows:

$$S(f) = [T_u \text{sinc}(T_u f) e^{-j\pi T_u f}] * \left[\sum_{k=-N/2}^{N/2-1} S_k \cdot \delta(f - k f_{sc}) \right]$$

$$S(f) = e^{-j\pi \frac{f}{f_{sc}}} \sum_{k=-N/2}^{N/2-1} \frac{S_k}{f_{sc}} \text{sinc}\left(\frac{f - k f_{sc}}{f_{sc}}\right)$$
(3)

Due to the rectangular pulse shaping filter applied to each sub-carrier, each OFDM symbol in the frequency domain is represented by a *sinc* function. This is clearly shown in Equation (3). Due to the *sinc* shape of the OFDM symbols, large sidelobes may occur which could potentially interfere with the signal transmissions of the neighboring systems [17]-[18].

Figure 3a, shows the OFDM sub-carriers where at each sub-carrier frequency there is only one peak value of the *sinc* function and all other sub-carriers have zero values. That means that even though multiple sub-carriers coexist, they are all independent and do not influence each other. This is referred to as orthogonality [16]-[19]. Figure 3b shows the power spectral density of an OFDM modulated signal. The interference power due to the first sidelobe in the first adjacent band is shown.

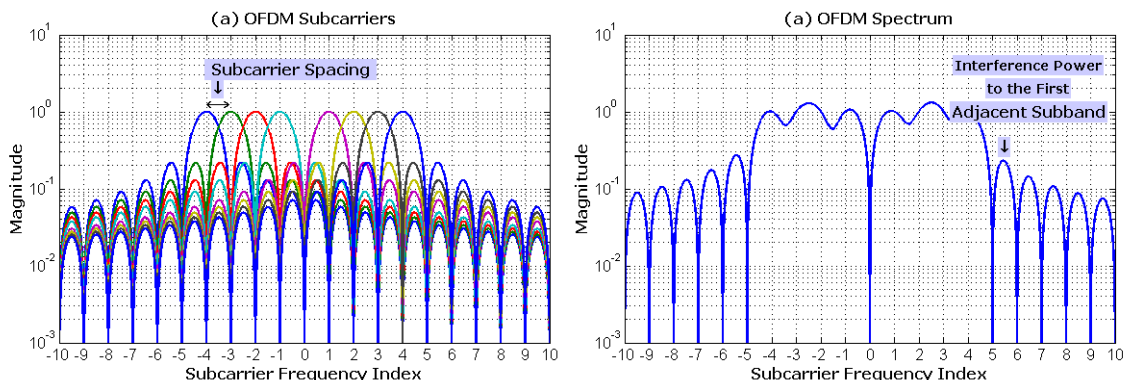


Figure 3. Orthogonality between sub-carriers.

3. MITIGATING TECHNIQUES FOR ACI

ACI in OFDM system, is a result of high out-of-band radiation that prevents the efficient use of the available spectrum [8]. Recently, four different techniques for sidelobe suppression have been proposed and are summarized next.

3.1 Guard Bands

Guard bands represent a simple technique that modulates high frequency sub-carriers with zero data. In Figure 4, one guard band is used on each side of the OFDM signal in order to reduce the out-of-band radiation. However, these guard bands act as buffer bands between the different OFDM systems and are actually wasted spectrum [20].

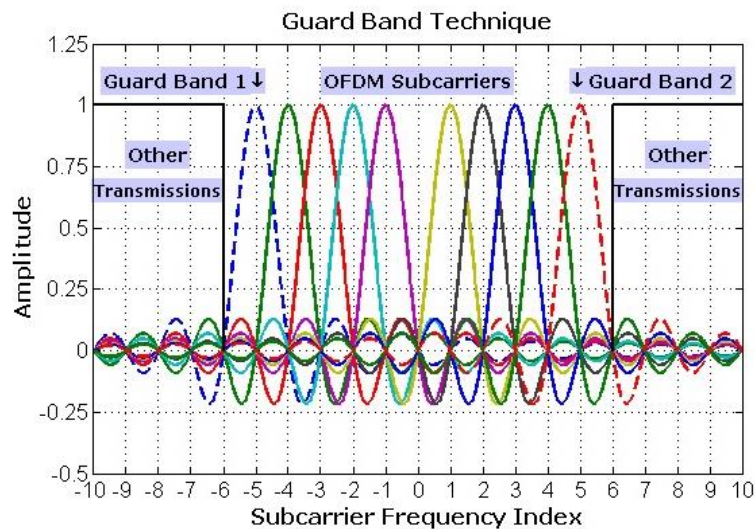


Figure 4. Guard band technique for OFDM sidelobe suppression.

The effect of GBs differs for different non-linear devices that may introduce OOB radiation due to excessive clipping of the OFDM signal. However, the reduction effect using guard bands is not significant enough and the drawback of this method is the less effective use of the available bandwidth.

3.2 Sub-carrier Weighing

This technique was proposed in [21] based on the multiplication of the used sub-carriers by sub-carrier weights which are chosen carefully to reduce the power in the sidelobes.

In Figure 5, an example of five sub-carriers is introduced and the amplitudes of individual sub-carriers are adapted to cancel each other in the optimization range, thus reducing the sidelobe power. SW method does not need to transmit any side information and is capable of reducing the OOB radiation of OFDM signals by more than 10 dB. However, it suffers from a slight loss in BER as mentioned in [21].

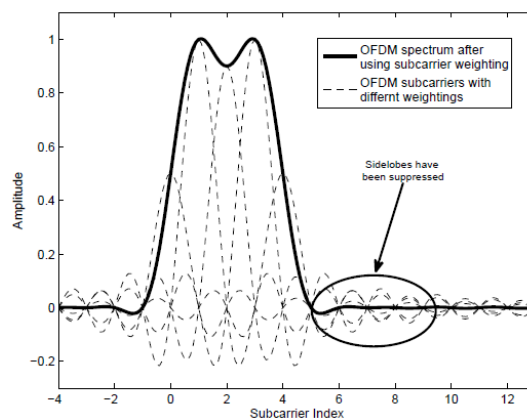


Figure 5. Sub-carrier weighing technique.

3.3 Cancellation Carriers

The cancellation carrier (CC) technique operates by inserting no data information carriers on the left and right hand sides of the OFDM spectrum with optimized weights as shown in Figure 6. In this figure, one CC (dashed line) is inserted on the right side of the OFDM spectrum (solid line) [22].

The amplitude of the CC is calculated to cancel out the sidelobe of the original OFDM signal. However, there is a small loss in bit error rate performance due to transmitting sub-carriers, which are not available for data transmission.

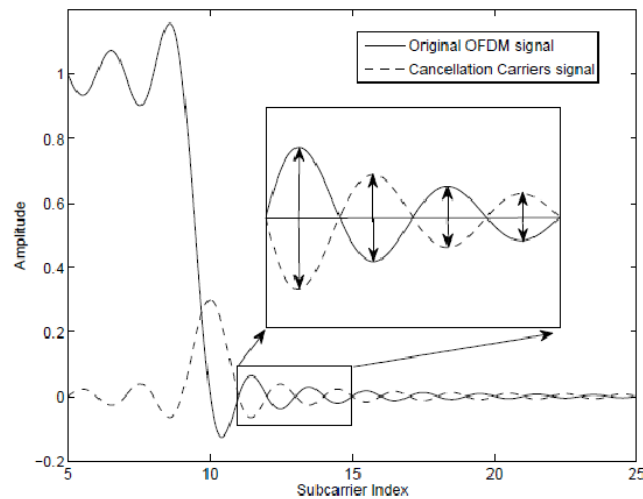


Figure 6. Cancellation carriers technique.

3.4 Raised-Cosine Filter

Raised-cosine a filter is relatively straight forward implementation and has the ability to reduce ISI, thus it is a good candidate to be used for OFDM sidelobe suppression. The ideal raised-cosine filter impulse response that is shown in Figure 7 is defined in [23] as follows:

$$h(t) = \text{sinc}\left(\frac{t}{T}\right) \frac{\cos\left(\frac{\pi\beta t}{T}\right)}{1 - \frac{4\beta^2 t^2}{T^2}} \quad (4)$$

where T is the symbol time. The frequency response of an ideal raised-cosine filter consists of unity gain at low frequencies, a raised-cosine function in the middle frequencies and significant attenuation at high frequencies. The width of the middle frequencies is defined by the roll-off factor β , where $0 < \beta < 1$.

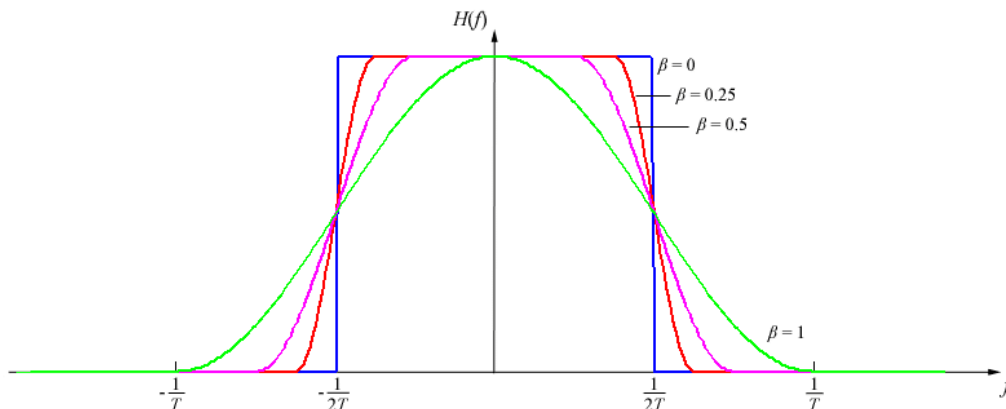


Figure 7. Different roll-off factors for raised-cosine filter.

3.5 Combined Techniques

To achieve better sidelobe suppression, several of the existing techniques can be combined. When digital signal is transmitted, the sidelobe of OFDM signal should be suppressed by 15 dB, which means low enough interference with other transmissions. For some of the techniques mentioned previously, a reduction of about 15 dB can be achieved [24].

By the combination of modulated raised-cosine filter and the cancellation carriers technique, a more reduction in the OOB radiation can be achieved in comparison with using the individual reductions of either technique. [25]. For an ideal raised-cosine filter, the frequency response is symmetric and the center frequency is located at zero. However, the raised-cosine filter needs to be modulated to the location of the OFDM data carrier block. In addition, to ensure that the spectrum is efficiently used and there is no interference with other transmissions by using CCs to reduce the OOB radiation, the sidelobe power of the signal must be suppressed.

4. PROPOSED TECHNIQUE FOR ACI REDUCTION

4.1 Reduction Technique

The proposed technique is based on increasing the resolution in the frequency domain OFDM signal by padding the time domain signal with zeros as illustrated in Figure 8 [26].

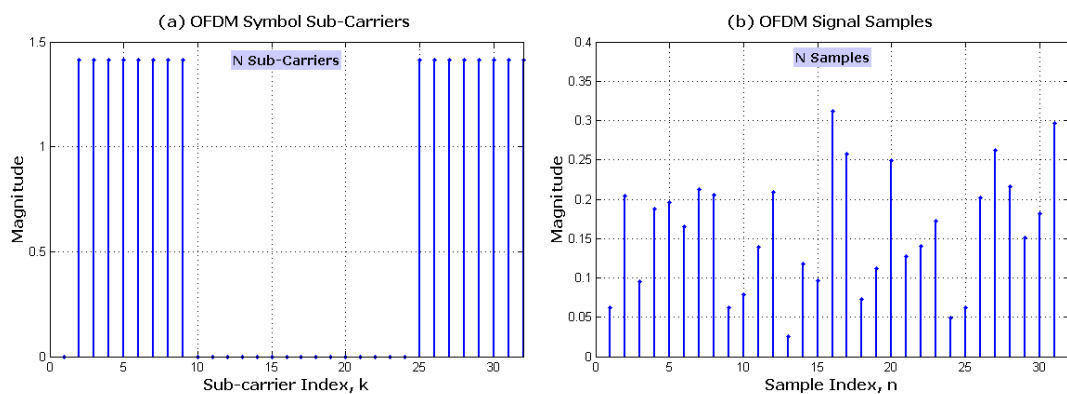


Figure 8. Illustrated OFDM sub-carrier input and output of the IFFT.

The frequency domain signal shows the sidelobes of the OFDM symbol that interfere with the adjacent systems reducing their performance. These sidelobes are selected and padded by zeros in the positions of the desired signal as shown in Figure 9.

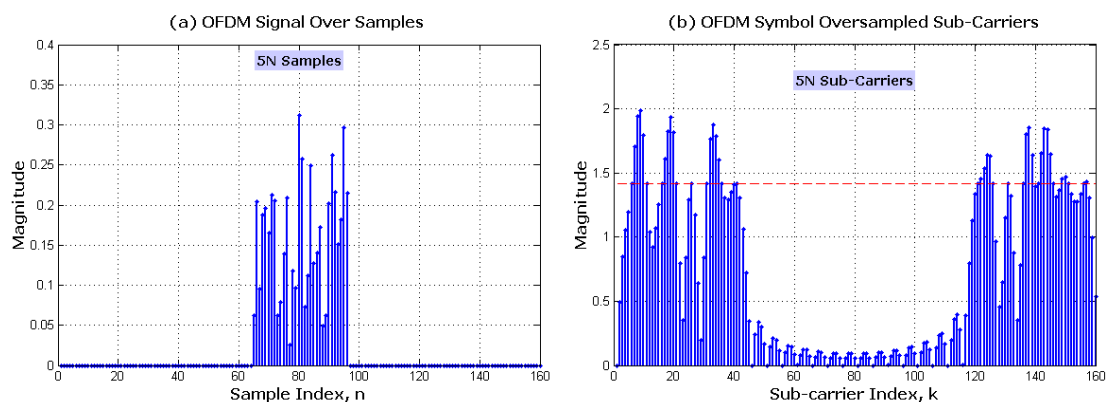


Figure 9. Increasing the resolution in the frequency domain OFDM signal.

At the receiver, these sidelobes do not affect the desired OFDM signal performance, since the FFT process at the receiver only samples the OFDM sub-carriers at the desired sub-carrier frequencies, which are orthogonal and the sampling at the sidelobes returns zero values. These zeros are removed to select only the desired data sub-carriers to be demodulated and detected.

But, when this signal is received by an adjacent system, these sidelobes interfere with the new system data and reduce its performance, resulting in what is called ACI. The sidelobes are selected, zero padded and then inverse Fourier transformed, resulting in a time domain signal that represents the assumed ACI signal as illustrated in Figure 10. The time domain signal in Figure 10b represents the N-samples OFDM signal representing the sidelobes padded to the right and to the left in order to increase the resolution of its frequency domain signal.

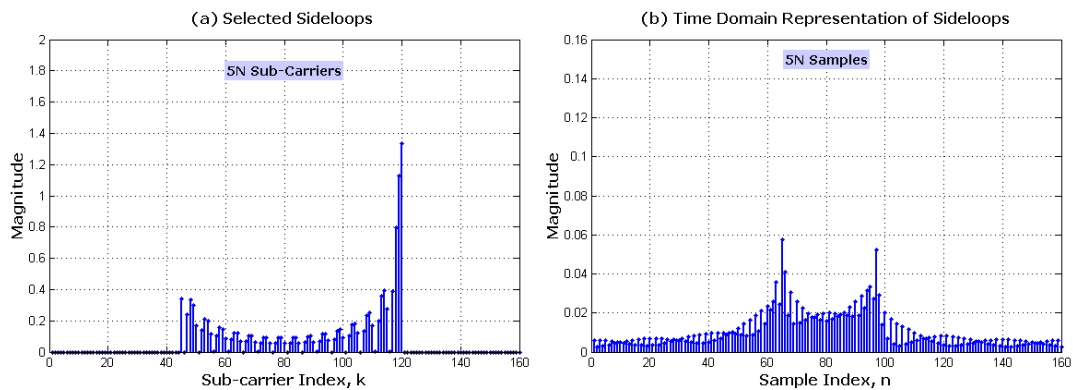


Figure 10. The selected sub-carriers in the sidelobes positions.

To down-sample the frequency domain signal, the padded samples in the time domain must be removed and the resulting samples then Fourier transformed to N-number of pilots at the positions of the desired OFDM sub-carrier frequencies as illustrated in Figure 11.

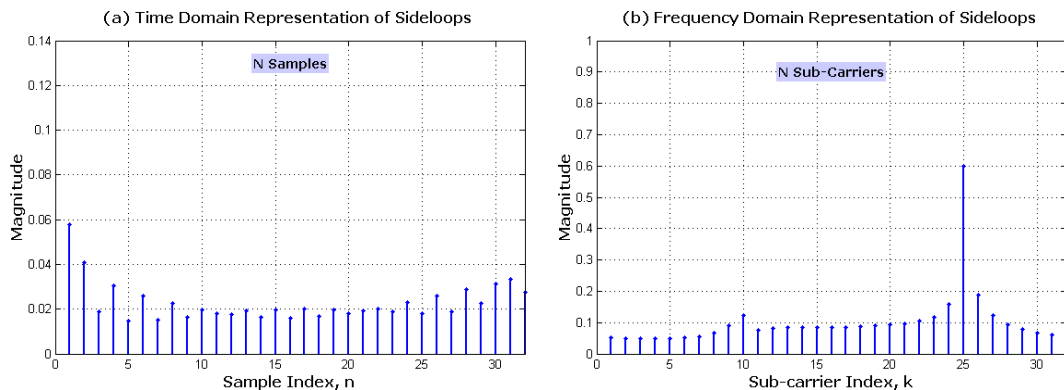


Figure 11. The selected N (number of samples) representation of sidelobes.

In order not to add power at the high frequency sub-carriers that represent the sidelobes, the positions of these sub-carriers are replaced by zeros keeping the needed pilots as a compensated signal to the sidelobes. This is illustrated in Figure 12. These pilots are then extracted from the main data sub-carriers in the desired signal resulting in reduced sidelobes power and ACI.

4.2 Matlab/Simulink Model

In this paper, the simulation model is divided into three parts. The first part is the transmitter (the original signal), then comes the ACI reduction part (ACI signal on the original signal) and finally the receiver part. Data transmission is a binary signal that consists of ones and zeros. The transmitted data are generated by OFDM symbol generator through QPSK mapping, S/P converter, zero padding, IFFT and cyclic prefix, through the transmission channel to the receiver.

Oversampling in OFDM is usually implemented by modulating some sub-carriers at the spectrum margins with zero. In this technique, more resolution in the frequency domain is needed that corresponds to adding zeros to the left and right of the OFDM time domain signal, as in Figure 13. This will increase the time duration of one OFDM symbol without changing the sampling time. By keeping the sampling

time constant, the sampling frequency is kept constant, but the number of frequency components increases due to increasing the FFT size for this process, where each component will have a frequency less than the main sub-carrier frequency of the original OFDM symbol. Looking at the sidelobes of the main OFDM symbol shows zeros (zero padding) at each OFDM subcarrier, whereas after adding zeros at the time domain, frequency components between these zeros appear with some power said to be the ACI affecting the adjacent OFDM signals.

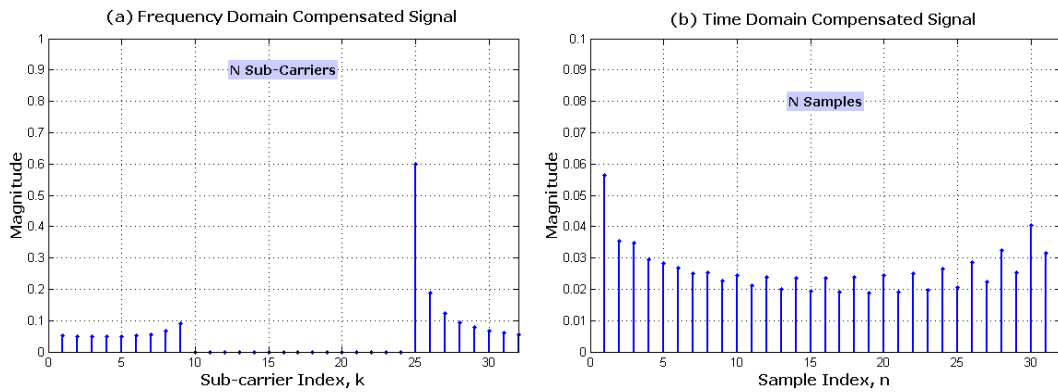


Figure 12. Selecting the sub-carriers that compensate for the ACI.

ACI is a result of the addition process from all the sub-carrier samples in the sidelobes of the OFDM signal. Those sidelobes will interfere with the adjacent OFDM signal. Each OFDM signal has its own sampling frequency reading. So when the desired OFDM signal starts to sample its sub-carriers and because the adjacent OFDM signal is close to it, it will sample the adjacent signal without knowing the difference between the two OFDM signals that would cause an interference or noise. To reduce noise, the power of the OFDM sidelobes has to be reduced.

As shown in Figure 13, the block labelled “Select Sidelobes Zero Padded” selects only these frequencies that represent the ACI and pads the new real data sub-carriers with zeros to reach a new number of IFFT points, as in Figure 14.

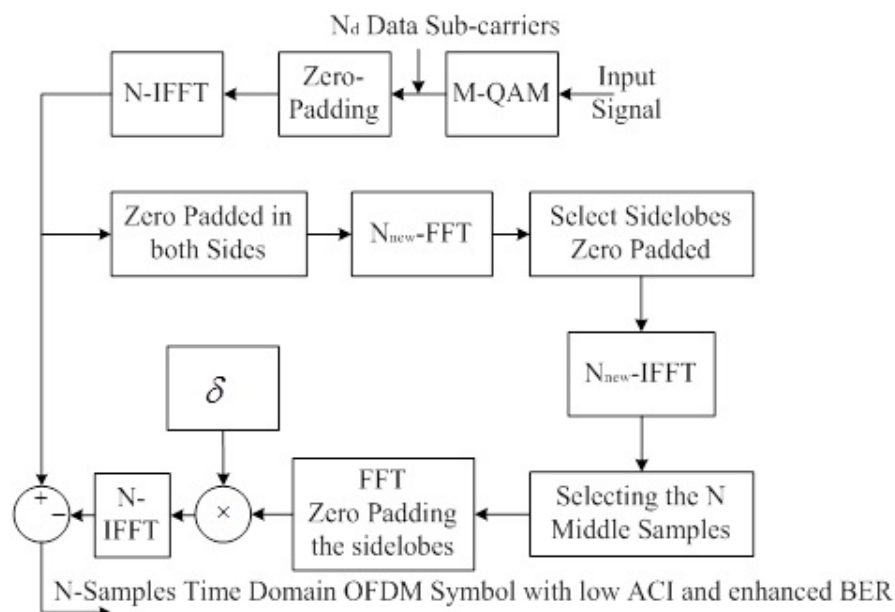


Figure 13. OFDM transmitter using the proposed technique.

The zero padded frequency domain signal is converted into the time domain using N_{new} -IFFT process, where N_{new} is the N original number of OFDM samples with the new zeros added as samples to the time domain signal.

The resulting N -number of samples in the middle of the output of the N_{new} -IFFT process is selected, which is assumed to be the power added to the original signal producing more power in the sidelobes. These sub-carriers are then translated to the frequency domain by N -FFT process, which results in some power components at the positions of the original N_d data sub-carriers, whereas the other components are neglected because we do not want to add more power to the zeros of the original signal that increases the ACI. The resulting frequency components are then multiplied by δ -factor to compromise for the BER performance of the system, since these components represent noise to the original signal.

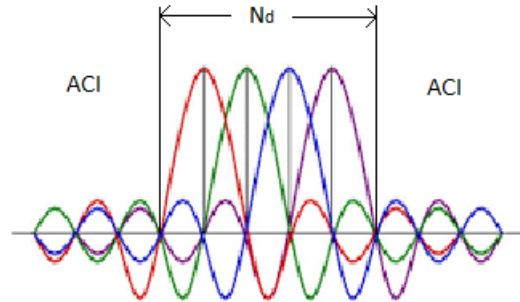


Figure 14. OFDM sub-carriers three-part division.

The resulting optimized frequency components are then transformed to the time domain by N -IFFT process and subtracted from the original OFDM signal, producing an OFDM signal with low power in the sidelobes; i.e., low ACI.

4.3 OFDM System Parameters

The proposed ACI reduction technique discussed in the previous section is assessed using a Matlab/Simulink simulation. The OFDM system parameters are based on the next generation of mobile communication systems and their values that are used for the performance assessment under the effect of AWGN channel are presented in Table 1 [10]-[11].

The cyclic prefix length is proposed to be greater than or equal to the maximum delay spread in urban channels proposed by the CODIT channel model [27].

Table 1. OFDM system parameters.

Description	Value
Modulation type	$M = 4$ (QPSK)
Cyclic prefix	$T_g \geq \tau_{\text{max}} = 4 \mu\text{s}$
Bandwidth	$BW = 20 \text{ MHz}$
OFDM symbol useful time duration	$T = 4 \times T_g = 16 \mu\text{s}$
Sub-carrier frequency	$f_{sc} = \frac{1}{T} = 62.5 \text{ kHz}$
Number of data sub-carriers	$N_d = \frac{BW}{f_{sc}} = 320$
FFT size	$N = 1024$

4.4 Simulation Steps

MATLAB/Simulink is a block diagram environment for multi-domain simulation and model-based design. Simulink provides a graphical editor, block libraries and solvers for modeling and simulating dynamic systems.

Through the study, the main reason of the interference is the sum of sub-carrier samples in the sidelobes

of OFDM symbol (out-of- band radiation). Reducing those radiations on the adjacent channels as much as possible with preserving the original data signal in the desired frequency is the main idea of the thesis.

Figure 15 shows the general block of the first step for the simulation; getting the information signal from the Bernoulli binary generator, then processing it through the OFDM transmitter system, which will be explained in the next section, adding ACI-1 and ACI-2 with the output of OFDM transmitter system, then processing the result through AWGN generator to the receiver to calculate the BER to know the amount of error.

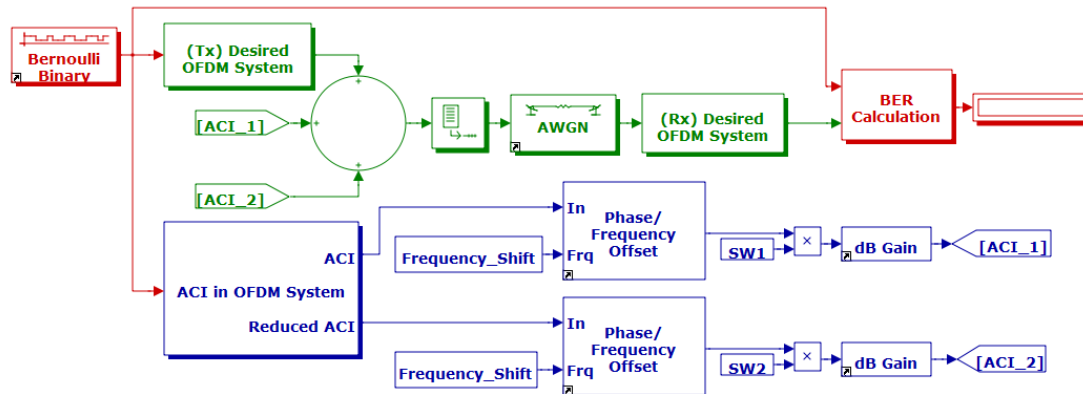


Figure 15. General block diagram of simulation.

ACI-1 represents the interference from the adjacent channel that affects the desired signal and ACI-2 represents the interference from the adjacent channel that affects the desired signal but after using the reduction technique. The frequency shift block is used to shift the frequency of the adjacent OFDM interference signal that affects the desired signal. In this thesis, the frequency would be shifted to the left by three values -20.1 MHz, -20.05 MHz and -20 MHz. ACI-1 and ACI-2 can be controlled by the switches SW1 and SW2 by multiplying the switches by 1 to open them and 0 to close them.

The power of the adjacent OFDM interference signal could be higher or lower than or equal to the power of the desired signal like -6 dB, -3 dB or 0 dB, which can be controlled by the gain of the signal.

Figure 16 shows the transmitter of the desired OFDM signal without ACI effect. The data transmitted is a binary signal which consists of ones and zeros.

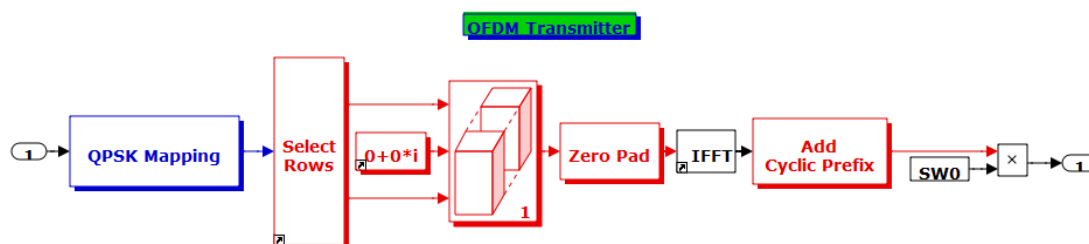


Figure 16. Transmitter of the desired signal.

Data is generated by OFDM symbol generator through QPSK mapping, S/P converter, zero padding, IFFT, cyclic prefix and up converting through the transmission channel. Figure 15 represents the ACI reduction technique applied on the adjacent OFDM signal that affects the desired signal. The difference between the desired signal and the output of this transmitter is the frequency shift, which has been explained above. Figure 17 has two outputs; the first one is the same as the desired signal, but shifted in frequency, while the second output is the same as the desired signal, but with ACI reduction technique.

ACI reduction block diagram represents the technique of reduction, which has been previously mentioned. After adding the zeros to the time domain OFDM signal samples, the OFDM symbol sub-carriers will be increased in the sampling points. The purpose of increasing the sampling points is to see the sidelobe power that causes an interference to the adjacent systems.

To study the interfering sidelobes, these have to be selected with removing the OFDM data sub-carriers in the medial, then adding zeros to the left and the right in order to compensate for the data having been removed.

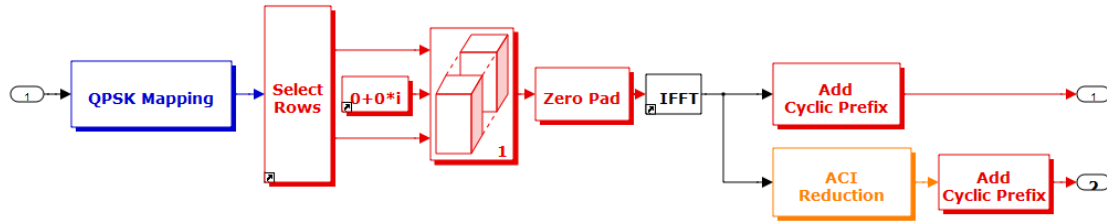


Figure 17. Transmitter of the desired signal with ACI reduction.

After processing the result through IFFT, the output will be the ACI signal presented in time domain. Choosing the N samples for OFDM signal, then down-sampling the signal by removing the added zeros in time domain from the beginning, then processing it through the FFT will lead to obtain a representation of the N number of sub-carriers in frequency domain for the sidelobe power.

4.5 Simulation Result

4.5.1 ACI Mitigation for QPSK-OFDM Signal at Zero dB Attenuation Factor

A comparison between BER and SNR values will be presented. All the figures below show the performance of QPSK-OFDM signal with zero attenuation factor ($\delta = 0$), but with different frequency shift and ACI gain values. When the attenuation factor is equal to zero dB, the attenuation will be unity, which means that all the power of the generated signal for ACI reduction is subtracted from the power of the data sub-carrier on the sidelobes of the original OFDM signal.

Figure 18 shows the BER performance when the gain of the adjacent interference signal is -6 dB below the original signal and the attenuation factor is 0 dB. As the SNR increases, the BER decreases. If the adjacent OFDM interference signal frequency is -20.1 MHz away from the desired one, and at $SNR = 8 \text{ dB}$, the BER is about 5×10^{-5} for both of the adjacent interference signals with and without ACI reduction. The BER for the desired OFDM signal at 8 dB is about 3×10^{-6} .

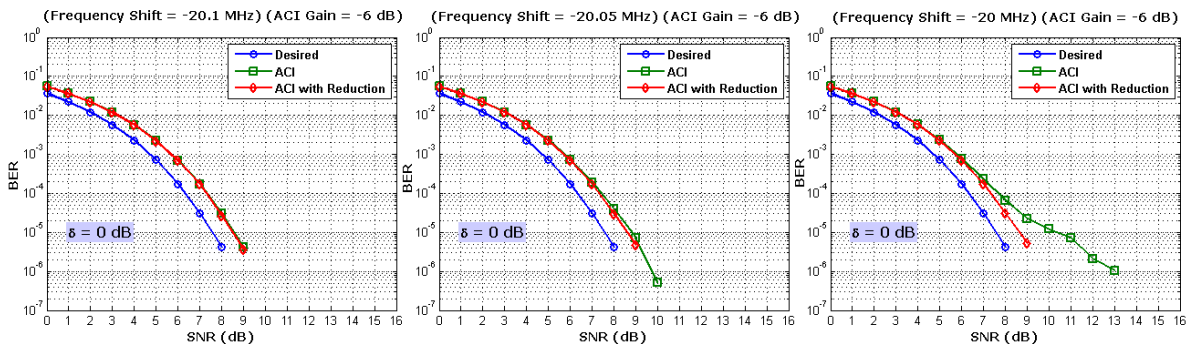


Figure 18. BER vs SNR QPSK-OFDM signal at -6 dB ACI gain with 0 dB attenuation factor.

For closer adjacent channel interference (-20.05 to -20 MHz), the BER performance decreases due to more interference power added to the desired signal. In Figure 18c, the BER increased to about 8×10^{-4} for the ACI without reduction while no change occurred by using the reduction technique.

These results are due to the -6 dB difference in the signal power between the adjacent and the desired signals as shown in Figure 19, which shows the performance of PSD using 0 dB weighing factor with different frequency shifts. The PSD for the ACI signal at the center frequency is almost -39 dBm and for the ACI signal after reduction is about -48 dBm, which is about 9 dB reduction. In fact, this is not the real difference since the reduction in power is measured as the average signal power to the average interference power, which is analyzed in Section 4.5.3 below.

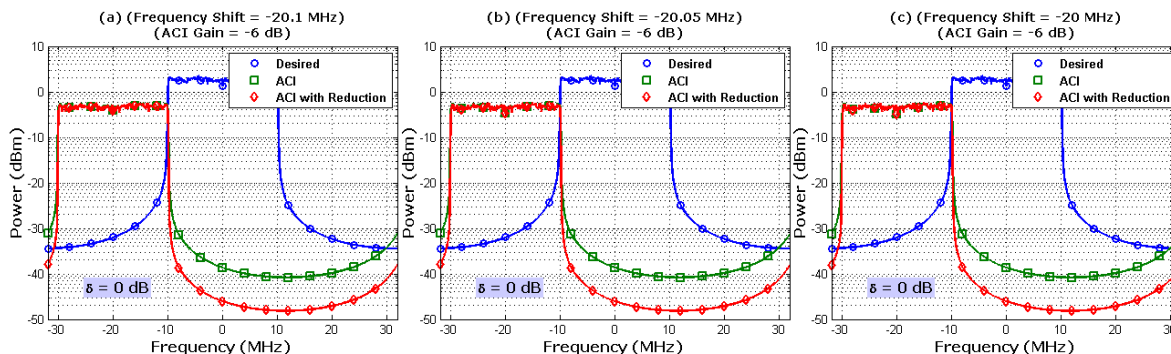


Figure 19. PSD of QPSK-OFDM signal at -6 dB ACI gain with 0 dB attenuation factor.

Figure 20 represents a clarification for Figure 19 for the PSD at different frequency shift values. Table 2 shows the power values for the adjacent OFDM interference signal that affects the desired OFDM signal. From the table, the closer the adjacent OFDM signal the higher the power that affects the desired OFDM signal, which means more ACI on the desired signal.

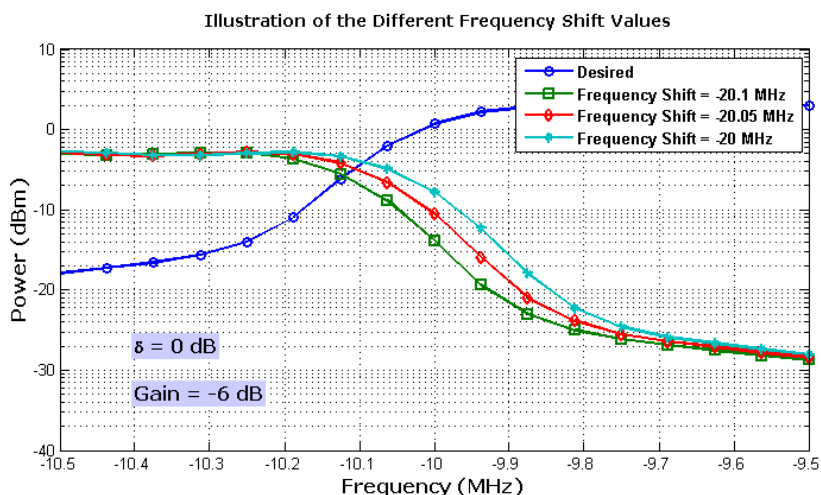


Figure 20. Illustration for PSD QPSK-OFDM signal at -6 dB ACI gain with 0 dB attenuation factor.

Table 2. PSD different values at -6 dB ACI gain with 0 dB attenuation factor.

Frequency (MHz)	Frequency shift (MHz)	PSD (dBm)
-10	-20.1	-16
-10	-20.05	-11
-10	-20	-8

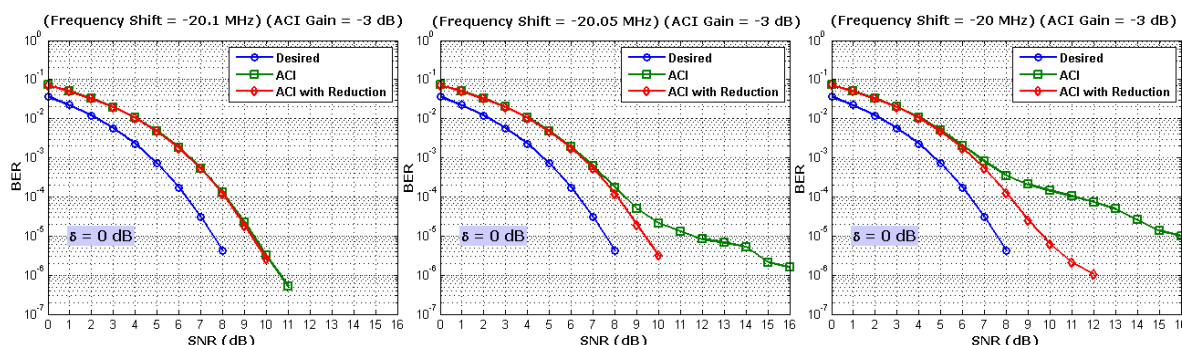


Figure 21. BER vs SNR QPSK-OFDM signal at -3 dB ACI gain with 0 dB attenuation factor.

If the adjacent channel has a higher gain, the effect of the interference on the desired signal would be higher.

Figure 21 shows the BER performance for -3 dB difference between the adjacent and the desired signals for different frequency separations. This shows an increase in the BER, especially when the adjacent signal is at -20 MHz to the desired one.

Figure 22 shows the performance of PSD at -3 dB difference, which shows that the sidelobe power is now closer to the desired OFDM data sub-carriers, resulting in an increase in the BER.

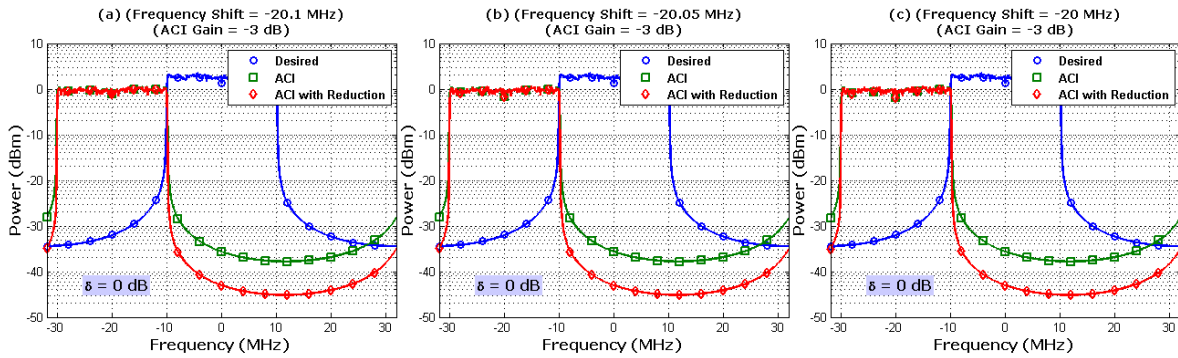


Figure 22. PSD of QPSK-OFDM signal at -3 dB ACI gain with 0 dB attenuation factor.

Figure 23 represents a clarification for Figure 22 for the PSD at different frequency shift values. Table 3 shows the power values for the adjacent OFDM interference signal that affects the desired OFDM signal. From the table, the closer the adjacent OFDM signal, the higher the power that affects the desired OFDM signal, which means more ACI on the desired signal.

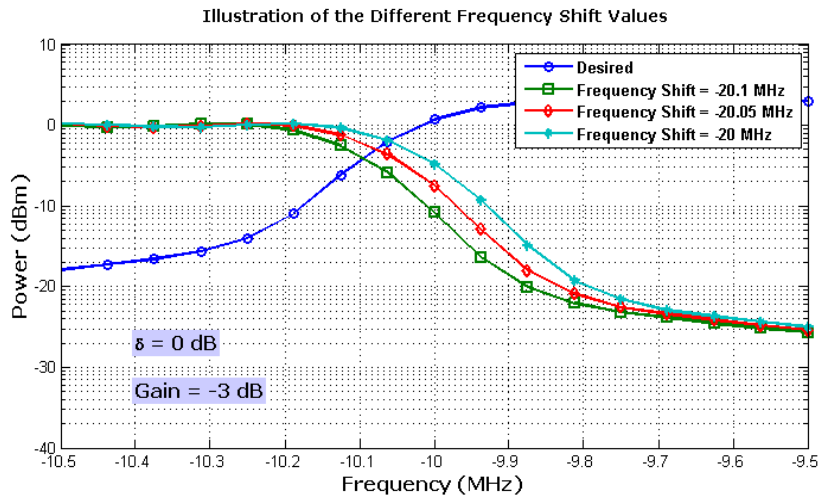


Figure 23. Illustration for PSD QPSK-OFDM signal at -3 dB ACI gain with 0 dB attenuation factor.

Table 3. PSD different values at -3 dB ACI gain with 0 dB attenuation factor.

Frequency (MHz)	Frequency shift (MHz)	PSD (dBm)
-10	-20.1	-12
-10	-20.05	-8
-10	-20	-7

Increasing the gain power for the adjacent signal will increase the interference with the desired signal. From Figure 24, the BER amount is increasing, because the value of the gain power is increased, but the best ACI reduction amount is when the frequency shift of the adjacent signal is at -20 MHz; a reduction from 10^{-3} to 10^{-4} at 9 dB SNR. A reduction of 10 dBm at 10 MHz from -35 dBm to -45 dBm

on the sidelobe power is obtained after using the ACI reduction technique as shown in Figure 25.

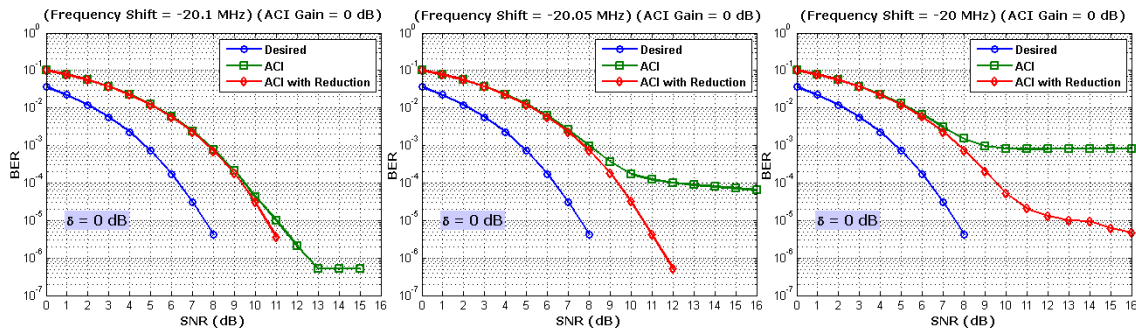


Figure 24. BER vs SNR for QPSK-OFDM signal at 0 dB ACI gain with 0 dB attenuation factor.

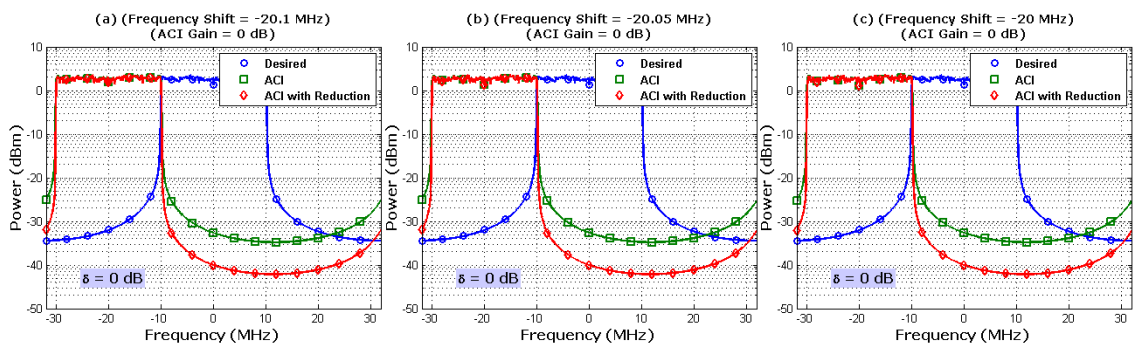


Figure 25. PSD of QPSK-OFDM signal at 0 dB ACI gain with 0 dB attenuation factor.

Figure 26 represents a clarification for Figure 25 for the PSD at different frequency shift values. Table 4 shows the power values for the adjacent OFDM interference signal that affects the desired OFDM signal.

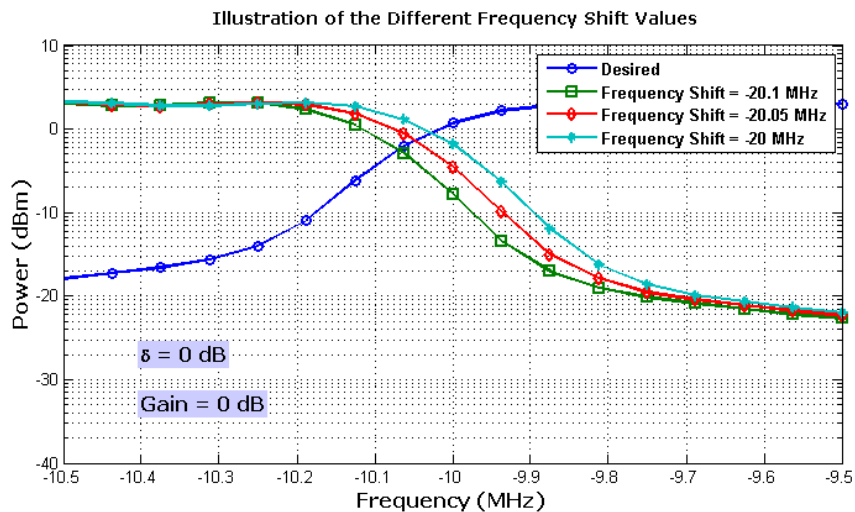


Figure 26. Illustration for PSD QPSK-OFDM signal at 0 dB ACI gain with 0 dB attenuation factor.

Table 4. PSD different values at 0 dB ACI gain with 0 dB attenuation factor.

Frequency (MHz)	Frequency shift (MHz)	PSD (dBm)
-10	-20.1	-8
-10	-20.05	-6
-10	-20	-4

From the table above, the closer the adjacent OFDM signal, the higher the power that affects the desired OFDM signal, which means more ACI on the desired signal. Figure 27 shows the BER and SNR when the gain of the adjacent interference signal is 3 dB and the attenuation factor on the sidelobes is 0 dB. When the adjacent OFDM interference signal is received by a gain power higher than the power of the desired signal, the interference will increase. Because the BER values are much higher than the previous results, the ACI reduction is not as strong as the ACI reduction resulting at 0 dB ACI gain.

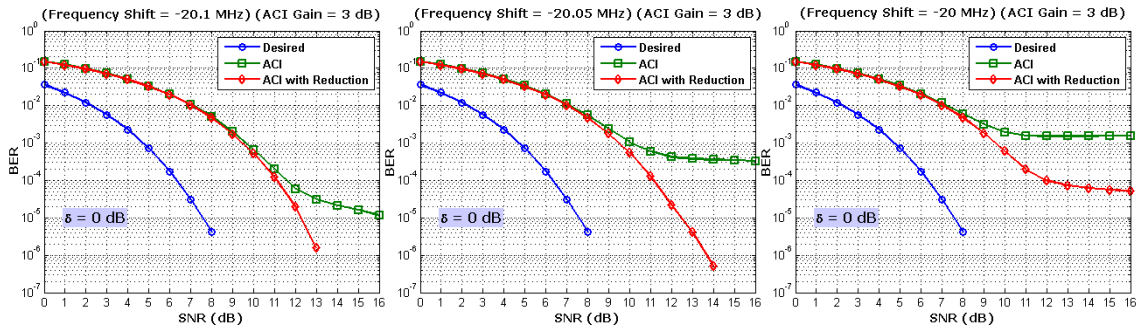


Figure 27. BER vs SNR for QPSK-OFDM signal at 3 dB ACI gain with 0 dB attenuation factor.

Increasing the gain power of the adjacent signal will increase the interference on the desired signal as shown in Figure 28. The PSD performance is reduced by 9 dB from -30 dBm to -39 dBm at the center frequency. This is also not the real difference, since the reduction in power is measured as the average signal power to the average interference power, which will be analyzed in Section 4.5.3 below as mentioned before.

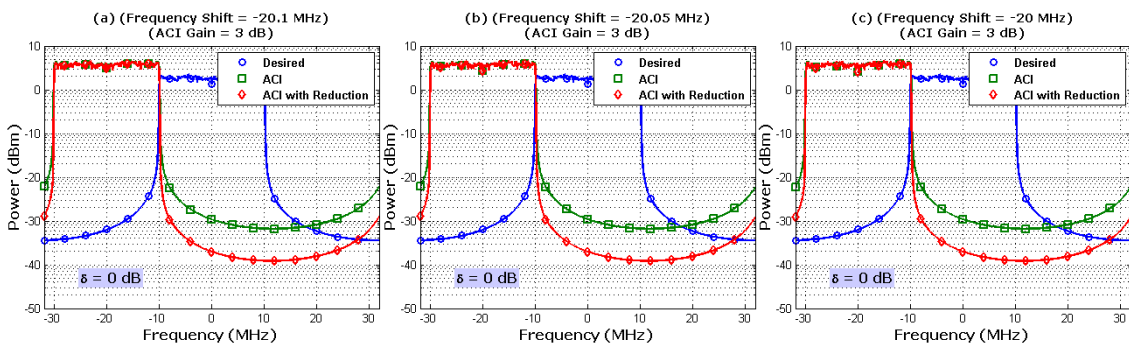


Figure 28. PSD of QPSK-OFDM signal at 3 dB ACI gain with 0 dB attenuation factor.

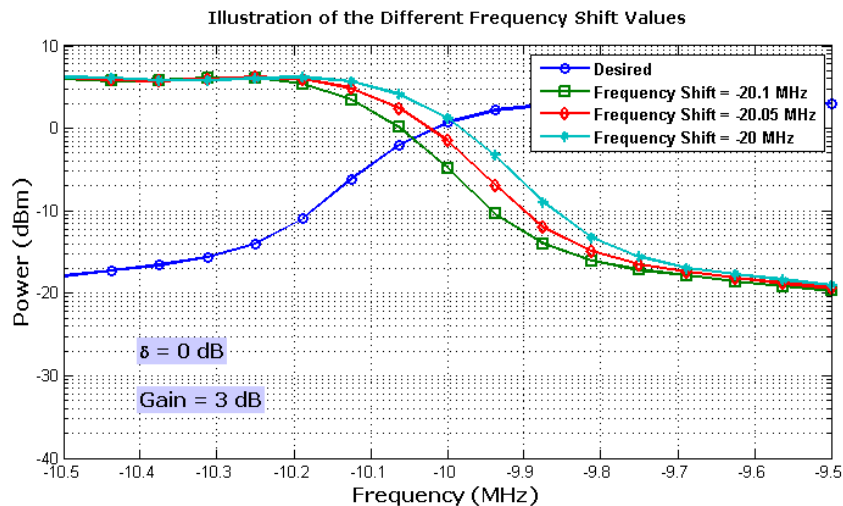


Figure 29. Illustration for PSD QPSK-OFDM signal at 3 dB ACI gain with 0 dB attenuation factor.

A clarification for Figure 28 is shown in Figure 29, where the performance of the PSD QPSK-OFDM signal at different frequency shift values is presented. Table 5 shows the power values for the adjacent OFDM interference signal that affects the desired OFDM signal.

Table 5. PSD different values at 3 dB ACI gain with 0 dB attenuation factor.

Frequency (MHz)	Frequency shift (MHz)	PSD (dBm)
-10	-20.1	-7
-10	-20.05	-3
-10	-20	1

4.5.2 ACI Mitigation for QPSK-OFDM Signal at -3 dB Attenuation Factor

All the figures below show the performance of a 20 MHz bandwidth QPSK-OFDM signal with -3 dB attenuation factor, but with different frequency shift and ACI gain values. When the attenuation factor is equal to -3 dB, the power of the generated oversampling signal for ACI reduction method is reduced to the half and subtracted from the power of the data sub-carrier on the sidelobes of the original OFDM signal, which means less sidelobe power reduction than by using zero attenuation factor. A comparison between BER vs SNR and PSD with different frequency shift and ACI gain values will be presented in the figures below.

Figure 30 shows the BER and SNR when the adjacent signal gain power is reduced to -6 dB with different frequency shifts values. When the SNR is 9dB, the best BER reduction is at -20 MHz.

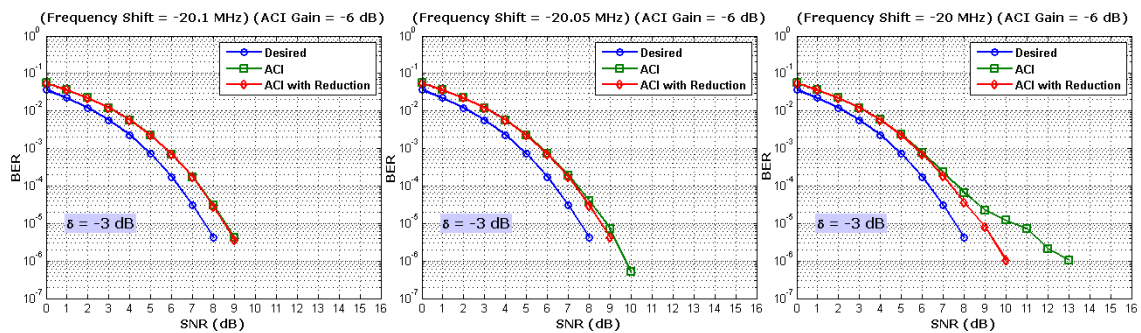


Figure 30. BER vs SNR for QPSK-OFDM signal at -6 dB ACI gain with -3 dB attenuation factor.

Figure 31 represents the PSD values. The reduction in the sidelobes is less than the previous results, because the gain power is minimum and the attenuation factor on those sidelobes is less than one. From the figure above, the PSD for the ACI signal at the center frequency is about -40 dBm and for the ACI signal after reduction is about -47 dBm, which is about 7 dB reduction. In fact, this is not the real difference, since the reduction in power is measured as the average signal power to the average interference power, which is analyzed in Section 4.5.3 below.

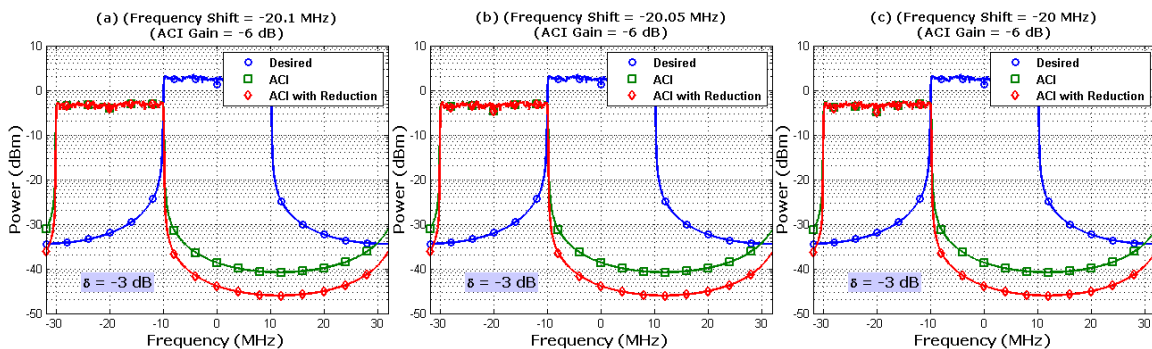


Figure 31. PSD of QPSK-OFDM signal at -6 dB ACI gain with -3 dB aAttenuation factor.

After increasing the gain power of the adjacent signal, the BER vs SNR performance is also increased.

Figure 32 shows that the best ACI reduction is at -20 MHz, as the BER is reduced from 10^{-3} to less than 10^{-4} at 9 dB SNR.

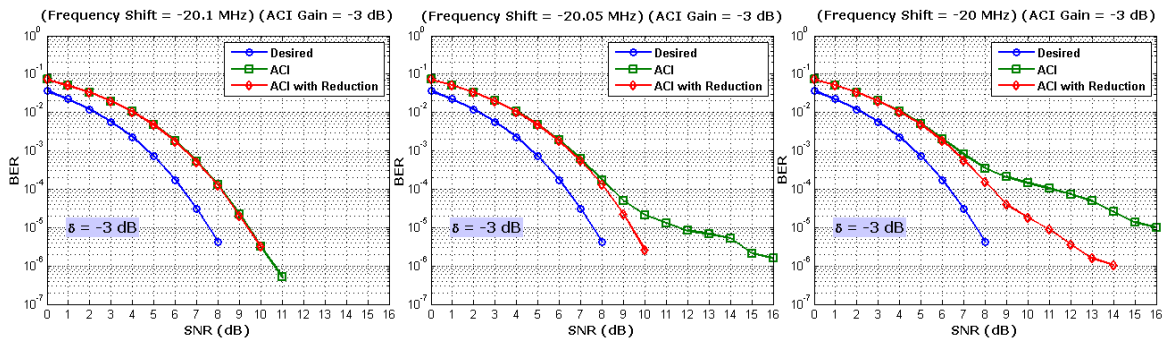


Figure 32. BER vs SNR for QPSK-OFDM signal at -3 dB ACI gain with -3 dB attenuation factor.

Figure 33 represents the PSD performance after increasing the adjacent signal gain power. It can be seen that the interference is increased on the desired signal, but a reduction of 7 dB on the power of the sidelobes is achieved after using the ACI reduction technique.

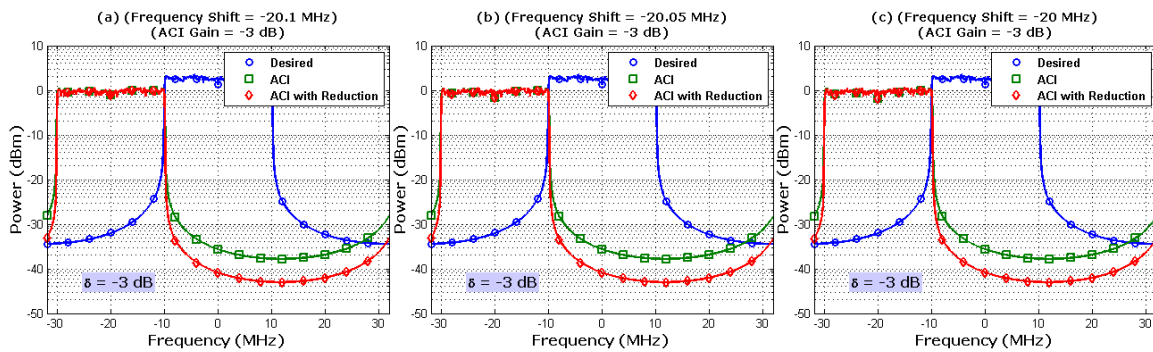


Figure 33. PSD of QPSK-OFDM signal at -3 dB ACI gain with -3 dB attenuation factor.

The BER gets higher as the adjacent signal power is increased. Figure 34 shows that the closer the adjacent signal to the desired signal, the better the ACI reduction.

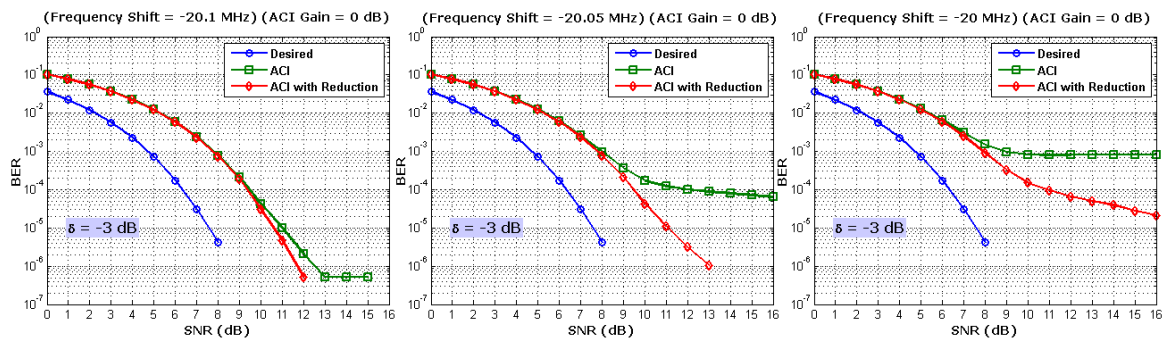


Figure 34. BER vs SNR for QPSK-OFDM signal at 0 dB ACI gain with -3 dB attenuation factor.

The effect of the sidelobe power from the adjacent signal is shown in Figure 35. As the PSD is increased because of the increment of ACI gain power, a reduction can be achieved by using half power sidelobe reduction technique.

The figures below represent half sidelobe power reduction with amplified adjacent gain power. The BER performance is getting higher than the previous results, because the gain is higher and so the amount of interference is higher. But, after using the ACI reduction technique, the BER is enhanced at a minimum value as shown in Figure 36.

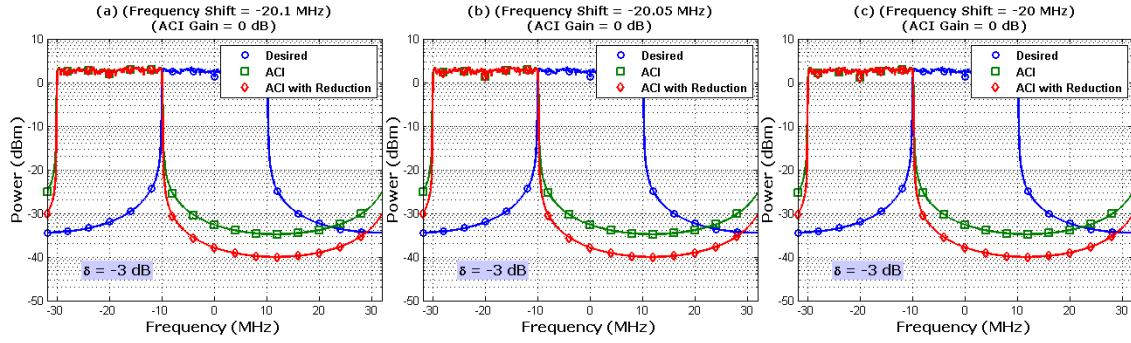


Figure 35. PSD of QPSK-OFDM signal at 0 dB ACI gain with -3 dB attenuation factor.

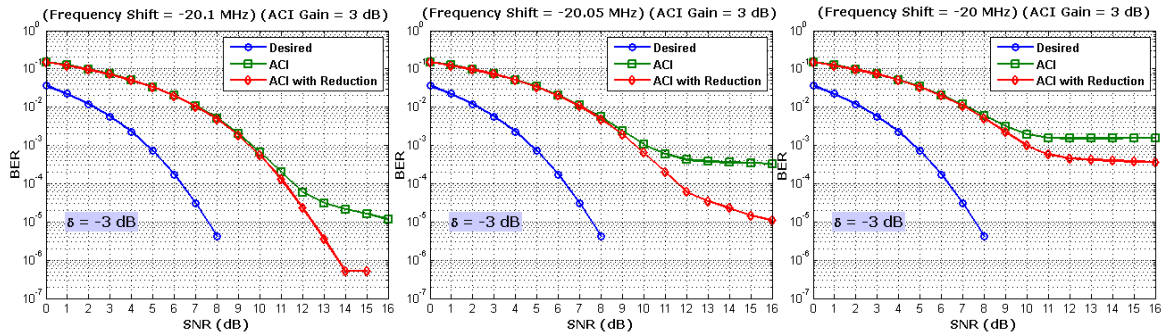


Figure 36. BER vs SNR for QPSK-OFDM signal at 3 dB ACI gain with -3 dB attenuation factor.

The interference from the adjacent sidelobes on the desired signal is very obvious. In Figure 37, at -10 MHz, the adjacent signal with ACI has a higher power than the desired signal at the same frequency, but after using ACI reduction technique, the adjacent power is reduced by 6 dB, which reduces the effect of interference and increases the system performance.

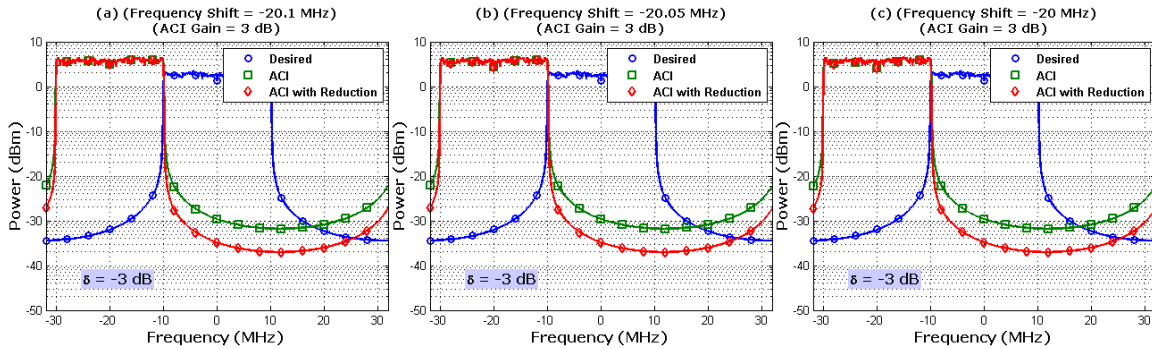


Figure 37. PSD of QPSK-OFDM signal at 3 dB ACI gain with -3 dB attenuation factor.

4.5.3 Signal to Interference Ratio (SIR) Analysis

The SIR is a comparison tool between the desired signal's average power to that of the interference signal, which is given as follows:

$$SIR = \frac{P_{Desired}}{P_{ACI}} \quad (5)$$

$$SIR_{dB} \downarrow = P_{Desired}^{dB} - P_{ACI}^{dB} \uparrow$$

Figure 38 illustrates the different SIR values between the desired OFDM signal's power and that of the ACI signal's power with and without applying the reduction technique. This illustration is done for the three different ACI applied frequencies and with different values of reduction factor δ .

Figure 38a shows that as the ACI power increases, the SIR decreases as given in Equation (5).

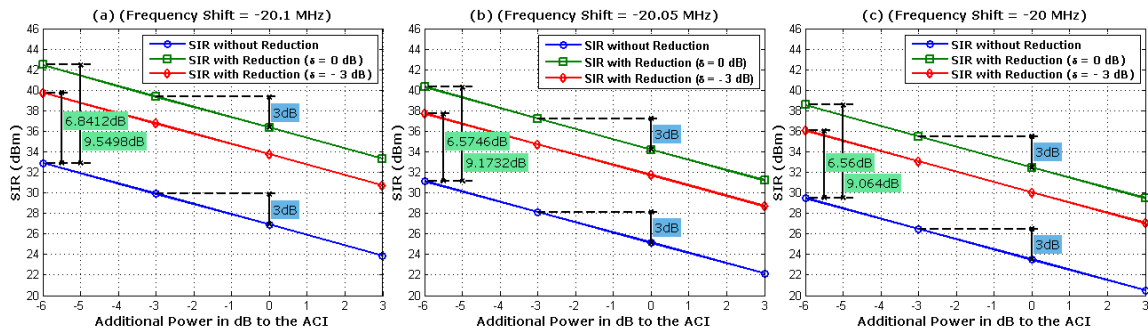


Figure 38. SIR comparison between the desired OFDM signal and the ACI signals.

In our simulation, four steps of increasing the ACI power by 3 dB each time are made from -6 dB to 3 dB and at each time the SIR decreases by 3 dB as shown in the figure.

The improvement in SIR is illustrated and found to be about 9 dB between the desired signal and the ACI signal after reducing the power at the sidelobes with a reduction factor of $\delta = 0$ dB, whereas for the ACI signal, with a reduction factor of $\delta = -3$ dB, the SIR is lower than before with a value of about 6.5 dB.

This result is due to the power of the added signal to the desired signal as a reduction technique. For $\delta = 0$ dB, no change occurs on the added (noise) signal, which results in more reduction on the sidelobes, therefore causing more SIR. But, for $\delta = -3$ dB, the power of the added signal is reduced to the half, which results in less reduction in the power of the sidelobes, leading to lower the SIR in comparison with the case before. In both cases, the SIR is improved.

Figure 38b and Figure 38c show the same analysis, but with one difference, which is that the value of the SIR is lowered. The reason behind this is the amount of power introduced by the ACI signal at its center frequency, becoming closer to the desired signal.

5. CONCLUSIONS

This work addresses the problem of ACI between the OFDM symbols. Through the study, the main reason of the interference is the sum of sub-carrier samples in the sidelobes of the OFDM symbol (out-of-band radiation). The purpose of this work is to reduce this radiation on the adjacent channels as much as possible, while preserving the original data signal in the desired frequency.

The operation that had been used in this paper is based on adding zero pilots in the time domain of the OFDM symbol, resulting in more resolution in the frequency domain, which would help reduce the out-of-band radiation.

The system speed is related to the sampling frequency of the FFT process, which is $f_s = 1/t_s = Nf_{sc}$. In this paper, as given in Table 1, the sampling frequency is given by $f_s = 1024 \times 62.5 \text{ kHz} = 64 \text{ MHz}$. By adding zeros to the time domain signal, nothing changes to the sampling frequency, since the zeros have the same sampling time. The change will be in the sub-carrier frequency, since the OFDM useful time duration increased and that led to decrease the sub-carrier frequency. The main idea about this technique is to increase the resolution in the frequency domain. The main effect is on the processing time that increased by increasing the size of the FFT process in this stage. The result after processing the frequency domain signal will be the opposite of the original form, but without data sub-carriers. That means only the addition of sub-carrier samples in the sidelobes, but with a negative power. Subtracting the new signal from the original signal will produce an OFDM signal with less sidelobe power to reduce ACI effect between the OFDM symbols.

From the results, the three main variables that affect the ACI reduction technique are: the attenuation factor, the ACI gain and the frequency shift. The attenuation factor controls the amount of the reduction on the sub-carrier sidelobe power. In the paper, two values are used for the attenuation factor: 0 dB, which means that all the power of the generated signal for ACI reduction method is subtracted from the power of the data sub-carrier on the sidelobes of the original OFDM signal. In case of the other value of

the attenuation factor is -3 dB, the power of the generated signal is reduced to the half and then subtracted from the power of the data sub-carrier on the sidelobes of the original OFDM signal, leading to less sidelobe power reduction than using zero attenuation factor. The second variable is the ACI gain; the adjacent signal gain power is very effective on how much the interference on the desired OFDM signal is. Four values for ACI gain (-6, -3, 0, 3) dB were taken to recognize the difference. The higher the gain power of the adjacent signal, the more interference on the sidelobe of the desired signal. The last variable mentioned in this work is the frequency shift. The closer the frequency of the adjacent signal, the higher the interference that affects the desired signal.

This reduction technique introduces a reduction of 9 dB SIR when using an attenuation factor of $\delta = 0$ dB, where this value reduces as the center frequency of the ACI approaches the desired signal due to the increase of the ACI power near the desired one. For $\delta = -3$ dB, a reduction of about 6 dB is achieved.

REFERENCES

- [1] V. K. Garg and J. E. Wilkes, *Wireless and Personal Communications Systems*, Upper Saddle River, NJ: Prentice - Hall PTR, 1996.
- [2] A. Goldsmith, *Wireless Communication*, New York: Cambridge University Press, 2005.
- [3] G. Jiann-Ching, A. Khayrallah and G. E. Bottomley, "Adjacent Channel Interference Rejection for Land Mobile Radio Systems," in the 48th IEEE Vehicular Technology Conference (VTC 98), pp. 1715-1719, vol. 3, 1998.
- [4] P. Dely, M. C. Castro and A. J. Kessler, "Impact of Adjacent Channel Interference on Performance of Multi-Radio Multi-Channel Mesh Networks," *European Collaborative Innovation Centres for Broadband Media Services*, 2014.
- [5] H. Holma and A. Toskala, *1970-WCDMA for UMTS: Radio Access for Third Generation Mobile Communications*, 2nd Ed., Chichester: Wiley, 2002.
- [6] W. C. Y. Lee, *Mobile Communications Design Fundamentals*, 2nd Ed., New York; Chichester: Wiley, 1993.
- [7] W. C. Y. Lee, *Mobile Communications Engineering: Theory and Applications*, 2nd Ed., New York; London: McGraw-Hill, 1998.
- [8] J. Kimery, "802.11ac Adjacent Channel Interference (ACI)," 14-April-2016, [Online], Available: <https://ytd2525.wordpress.com/category/signaling/>.
- [9] L. Hanzo, M. Münster, B. J. Choi and T. Keller, *OFDM and MC-CDMA for Broadband Multi-User Communications, WLANs and Broadcasting*, John Wiley & Sons, Ltd., July 2003.
- [10] R. V. Nee and R. Prasad, *OFDM for Wireless Multimedia Communications*, Boston; London: Artech House Publisher, 2000.
- [11] R. Prasad, *OFDM for Wireless Communications Systems: Artech House, Universal Personal Communications Series*, 2004.
- [12] K. G. Samarah, *High Bit Rate Air Interface for Next Generation Mobile Communication Systems*, Ph.D. Dissertation, School of Engineering, Design and Technology, University of Bradford, Bradford, 2007.
- [13] I. A. Glover and P. M. Grant, *Digital Communications*, London: Prentice-Hall, 1998.
- [14] D. J. Defatta, J. G. Lucas and W. S. Hodgkiss, *Digital Signal Processing: A System Design Approach*, Chichester: Wiley, 1988.
- [15] J. G. Proakis and D. G. Manolakis, *Digital Signal Processing: Principles, Algorithms and Applications*, 2nd Ed., New York; Toronto; New York: Macmillan; Maxwell Macmillan Canada; Maxwell Macmillan International, 1992.
- [16] S. Pagadarai, *Sidelobe Suppression for OFDM-Based Cognitive Radios in Dynamic Spectrum Access Networks*, M.Sc. Thesis, Department of Electrical Engineering & Computer Science, Jawaharlal Nehru Technological University, India, 2007.
- [17] A. Zubow and R. Sombrutzki, "Adjacent Channel Interference in IEEE 802.11n," in the 2012 IEEE Wireless Communications and Networking Conference (WCNC), pp. 1163-1168, 2012.
- [18] S. Brandes, I. Cosovic and M. Schnell, "Techniques for Reducing Out-of-band Radiation in OFDM-Based Transmission Systems," *European Transactions in Telecommunications*, vol. 21, p. 11, March 2010.

- [19] S. Technote, "Communication - OFDM, ", [Online], Available: http://www.sharetechnote.com/html/Communication_OFDM.html.
- [20] A. D. S. Jayalath and C. Tellambura, "Reducing the Out-of-band Radiation of OFDM Using an Extended Guard Interval," in the 54th IEEE Vehicular Technology Conference (VTC), pp. 829-833, vol. 2, 2001.
- [21] I. Cosovic, S. Brandes and M. Schnell, "Subcarrier Weighing: A Method for Sidelobe Suppression in OFDM Systems," IEEE Communications Letters, pp. 444-446, vol. 10, 2006.
- [22] S. Pagadarai, R. Rajbanshi, A. M. Wyglinski and G. J. Minden, "Sidelobe Suppression for OFDM-Based Cognitive Radios Using Constellation Expansion," in the IEEE Wireless Communications and Networking Conference, pp. 888-893, 2008.
- [23] J. G. Proakis, Digital Communications, 4th Ed., London: McGraw-Hill, 2001.
- [24] K. Pahlavan and P. Krishnamurthy, Principles of Wireless Networks: A Unified Approach, Prentice Hall PTR, 2001.
- [25] P. Wang, J. An and Y. Wu, "Reduction of Out-of-band Radiation in OFDM-Based DRM Simulcast Systems," International Conference on Wireless Communications, Networking and Mobile Computing, pp. 1-4, 2006.
- [26] A. W. Mustafa and K. G. Samarah, Adjacent Channel Interference Reduction in OFDM Systems, Unpublished Master Thesis, Electrical Engineering Department, Mutah University, 2017.
- [27] M. D. A. R. Chung, M. Dohler, M. Fiacco, S. Saunders, J. Brown, SMR. Jones, T. Harrold and A. Nix, "Propagation Models Final Report," London, 26 Jan. 2000.

ملخص البحث:

يعد الإرسال المضاعف عن طريق التقسيم الترددي المتعامد تقنية واحدة للإرسال الراديوي. ومع ذلك، إحدى أكبر المشكلات هي الإشعاع العالي خارج النطاق، الذي ينتج عن الفلقات الجانبية للحاملات الفرعية للإرسال المضاعف عن طريق التقسيم الترددي المتعامد؛ التي تعد مصدراً للتداخل من قنوات الإرسال المجاورة.

تركز هذه الورقة على تقليل الإشعاع خارج النطاق من خلال قراءة قدرة الإشعاع في الفلقات الجانبية واستخراجها عبر تمديد إشارة الإرسال المضاعف عن طريق التقسيم الترددي المتعامد في المجال الزمني بواسطة أصفار في الجانبين. ثم بتحويل الإشارة الناتجة إلى المجال الزمني وإزالة العينات الممتدة من أجل الحصول على العدد (N) من العينات من إشارة المجال الزمني التي تمثل إشارة الإشعاع خارج النطاق. ومن ثم إجراء تحويل فورييه للإشارة الناتجة وإزالة الحاملات الفرعية عالية التردد للحصول على أدلة يتم عكسها ثم إضافتها إلى الحاملات الفرعية للبيانات الأصلية، الأمر الذي ينجم عنه التقليل من تداخل القنوات المتجاورة. حيث أن الإشارة المضاعفة تمثل إشارة ضجيج بالنسبة للإشارة المرغوبة، مما يضعف أداء النظام من حيث معدل الأخطاء (BER). لذا، يتم استخدام معامل وزن يطبق على الإشارة المضافة للحصول على أداء أفضل مع تقليل جيد في الإشعاع خارج النطاق. تم استخدام محاكاة عبر (ماتلاب/سيميونك) لتقييم التقنية المقترحة بمعاملات وزن مختلفة وفصل مختلف الترددات بين الإشارة المرغوبة والإشارة المجاورة. فعند تخميد مقداره صفر ديسيبيل للإشارة المضافة، تم الحصول على تقليل للإشعاع خارج النطاق مقداره 10 ديسيبيل. أما عندما يعمل معامل الوزن على تقليل قدرة الإشارة الداخلة بمقدار 3 ديسيبيل، فيتم الحصول على تقليل في الإشعاع خارج النطاق بمقدار 6 ديسيبيل. وفي المحصلة، يتحسن أداء النظام من خلال تطبيق التقنية المقترحة، ويعتمد التحسن على البعد بين تردد الإشارة المرغوبة وتردد الإشارة المجاورة.

NOVEL TECHNIQUE FOR SECURING DATA COMMUNICATION SYSTEMS BY USING CRYPTOGRAPHY AND STEGANOGRAPHY

Walaa H. Al-Qwider¹ and Jamal N. Bani Salameh²

(Received: 17-May-2017, Revised: 20-Jul.-2017, Accepted: 30-Jul.-2017)

ABSTRACT

Information security is becoming more important and attracting much attention nowadays, as the amount of data being exchanged over the internet increased. There are various techniques to secure data communication, but the well-known and widely used techniques are cryptography and steganography. Cryptography changes data into another form that is unreadable by anyone except the intended receiver. Steganography hides the existence of secret data in a cover medium, so that no one can detect the hidden data except the authorized receiver. In this paper, we proposed a new technique for securing data communication systems by combining cryptography and steganography techniques. The cryptography algorithm that was used in this paper is Modified Jamal Encryption Algorithm (MJEA); it is a symmetric (64-bit) block encryption algorithm with (120-bit) key. For steganography, we designed an enhanced form of Least Significant Bit (LSB) algorithm with (128-bit) steg-key. The performance of the proposed technique has been evaluated by considering several experimental tests, such as impressibility test, embedding capacity test and security test. For this purpose, the proposed technique was applied on several 24-bit colored PNG cover images. All experimental results proved the strength of the proposed algorithm in securing the transition of data over unsecure channels to protect it against any attack. Furthermore, the simulation results show the superiority of our proposed algorithm when compared with other algorithms in terms of PSNR and embedding capacity.

KEYWORDS

Cryptography, Steganography, Hybrid system, Information hiding, Information security, MJEA, LSB.

1. INTRODUCTION

Nowadays, the amount of information being exchanged over the network is increasing tremendously and these data are sent mostly over an open channel, which threatens its security [1]. The three main elements that are considered to be the information security requirements are: Confidentiality, Integrity and Availability (CIA). They are widely used as a benchmark for evaluating information systems' security. Information security has gained important attention in recent years to protect the transmitted data from unauthorized accessing or interception. There are a lot of security techniques that are used to ensure the information security requirements; these techniques are cryptography, steganography, watermarking, digital signature and fingerprints. The most well-known and widely used techniques are cryptography and steganography [2]. Cryptography depends on the transfer of secret data from one format to another using certain ways by the sender until it reaches the recipient who works to get it back in its original form, whereas steganography conceals the existence of the secret data in another transmission medium. Cryptography can maintain confidentiality, while steganography can maintain integrity of the transmitted data. Cryptography contains two methods; an encryption method used to convert the original message into an unreadable form with the help of the encryption key and a decryption method used to get back the original message with the help of the decryption key. Cryptographic algorithms can be generally classified into two major groups: symmetric algorithms which use the same key for encryption and decryption and asymmetric algorithms which use different keys [3]. There are a lot of cryptographic algorithms in the literature. [4]-[12] show a review and comparative analysis of various encryption algorithms used for securing information, such as DES, RSA, RC4, RC5, Blowfish, Safer, CAST and Elliptic Curve cryptography.

1. W. H. Al-Qwider is with Computer Engineering Department, Mutah University, Alkarak, Jordan.

2. J. N. Bani Salameh is with Computer Engineering Department, Mutah University, Alkarak, Jordan. Email: jbanisal@mutah.edu.jo, jamalsalameh@yahoo.com.

Steganography is the process of hiding secret or sensitive information inside another carrier in such a way that no one except the authorized user can even detect that there is a secret message inside it [13]. Steganography can use many medium formats as a cover object to hide data in them such as; text, image, video, audio and protocol. The most used cover media are images [14]-[18]. The steganography system that uses digital images as cover files is called image-based steganographic system. Color image and gray image both can be used as cover media, but mostly the color one is used, because it gives more capacity and space for hiding data and its degree of redundancy is high, which makes it very suitable to use in steganography as a cover object [19]. Image steganography techniques can be broadly classified into two categories; namely, spatial domain and frequency or transform domain. In spatial-domain techniques, the pixel values of the cover image are directly manipulated or replaced by the secret message bit. Frequency domain-based methods embed the secret data in the transform coefficients of the cover image. The cover image is first transformed into the frequency domain and then messages are embedded in the transform coefficient [20]. The most common and simplest technique in spatial domain steganography techniques is Least Significant Bit (LSB) technique [21]-[23]. It requires less time and algorithmic complexity compared to other techniques. It takes the least significant bits of each byte on each pixel of the cover image and replaces them with the secret data bits. Number of bytes for each pixel depends on the format used to store the digital image; if 8-bit format is used, then there is just one byte, while if 24-bit format is used, then there are 3 bytes for each pixel. Number of bits taken from each byte to the replacement operation depends on the LSB technique used; some techniques take a fixed number of bits from each byte, whereas other techniques take a variable number of bits [24].

There are a lot of steganography algorithms in the literature; [25]-[26] show a survey and analysis of various steganographic techniques used for information hiding. In the following paragraphs, we will give a brief description about some steganographic algorithms that will be used in the evaluation process to compare them with our proposed algorithm. S. Masud, M. Saifur and M. Ismail proposed a steganography algorithm, where a secret key is used in the selection procedure of the LSB. Also, they used a 24-bit RGB color image as a cover medium. First, the cover image is divided into three matrices (red, green and blue). Also, the secret data is converted into binary representation. The red matrix and the secret key decide where to hide the secret data bits into either green matrix or blue matrix. Each bit of the secret key is XORed with each LSB of red matrix. The resulting XOR value decides that 1 bit of the secret data will be placed with either LSB of the green matrix or the blue matrix. The same process will be continued until the secret data bits are finished. The length of hidden information is stored in the first row of stego-image during the hiding process. In the extraction process, the same secret key must be used. Each bit of the secret key is XORed with each LSB of red matrix of the stego-image. The resulting XOR value decides that 1 bit of hidden information is stored in either LSB of green matrix or blue matrix. The recovery process will be continued depending on the length of hidden information bit stream [27]. Adnan Gutub proposed an RGB image steganography technique based on the pixel indicator. The secret data bits are hidden into two of the RGB pixel channels based on the indication within the third channel. The indicators have been selected in sequence; if the first indicator selection is the red channel in the pixel, the green is channel 1 and the blue is channel 2 (i.e., the sequence is RGB). In the second pixel, if the green channel is selected as the indicator, then red is channel 1 and blue is channel 2 (i.e., the sequence is GRB). In the third pixel, if blue is the indicator, then red is channel 1 and green is channel 2 (i.e., the sequence is BRG) [28]. S. Amritpal and S. Harpal proposed an improved LSB technique for color images by embedding the information into three planes of an RGB image. It replaces bits of the cover image in the order of 2:2:4 of the LSB in three planes (i.e., Red, Green and Blue planes) with the bits of secret data. The ratio 2:2:4 is selected depending on the sensitivity of red and green components of the light being similar and more sensitive as compared to the blue component. Thereby, security is increased and the rate of distortion is lowered in the cover image after hiding the secret message [29].

Cryptography and steganography can be combined together to make a strong security system for securing information from unauthorized access or unwanted intervention, in order to maintain its confidentiality and integrity. There have been lots of works in the literature that combine steganography with cryptography for more security. In the following paragraphs, we will give a brief description of some of them. M. Juneja and P. S. Sandhu designed a robust image steganography technique that is based on LSB insertion and encryption. They first encrypt the user data by using RSA algorithm, then they hide the encrypted data in an image using LSB insertion. The application performs an analysis on the user's library of images. This analysis allows users to hide their data in the image that is less likely

to be vulnerable to stegananalysis [30]. K. Joshi and R. Yadav proposed a new image steganography method in spatial domain combined with cryptography. They use a gray image as a cover image. Firstly, they encrypt the secret message by using Vernam Cipher algorithm, then they hide the encrypted message in a gray image using LSB with Shifting (LSB-S) algorithm. In LSB-S, they use four LSB of the pixel and perform circular left shift operation and XOR operation [31]. Y. Rener, Z. Zhiwei, T. Shun and D. Shilei tried to improve the imperceptibility of the steganography algorithm by combining it with DES encryption algorithm. The secret information is encrypted using DES algorithm, then it is embedded in a gray cover image using LSB steganography algorithm [32]. S. Ush, G. A. Sathish and K. Boopathy proposed a secure triple level encryption method based on combining steganography and cryptography. The data to be sent is first encrypted using the Playfair Cipher method, then the encrypted data will be encrypted again using AES algorithm after that the produced cipher text will be embedded in a color cover image using LSB algorithm and a hiding key to determine where to hide the data [33]. G. S. Charanl, S. S. Kumar, B. Karthikeyan, V. Vaithyanathan and K. D. Lakshmi proposed a novel LSB image steganography with multi-level encryption. The secret data is first encrypted using Ceaser Cipher technique, then it is encrypted again based on Chaos theory. Thereafter, the encrypted data will be embedded in a color image using 3, 3, 2 LSB replacement algorithm. In this algorithm, each 8 bits of the encrypted data are embedded in one pixel of the cover image, hence the first 3 bits are replaced with 3 LSB bits of red byte, the next 3 bits are replaced with 3 LSB bits of green byte and the last 2 bits are replaced with 2 LSB bits of blue byte [34]. S. A. Laskarand and K. Hemachandran proposed an embedding approach which is a combination of steganography and cryptography. The secret message is first encrypted using transposition cipher method, then the encrypted message is embedded in a cover image using the LSB insertion method. Each 3 bits of the encrypted data will be hidden in one pixel of the cover image; the first bit is replaced with the LSB bit of red byte, the next bit is replaced with the LSB bit of green byte and the last bit is replaced with the LSB bit of blue byte [35]. K. Muhammad, M. Sajjad, I. Mehmood, S. Rho and S. Wook Baik proposed a novel magic LSB substitution method (M-LSB-SM) for RGB image. They convert the image into a hue –saturation-intensity (HSI) color space, then the achromatic component (I-plane) of HIS is divided into four sub-images of equal size. After that, a secret key is used to rotate the four sub-images with different angles. The secret information is divided into four blocks, then each block is encrypted by using multi-level encryption algorithm (MLEA) and embedded into one of the rotated sub-images based on a specific pattern using magic LSB substitution [36].

As mentioned before, using steganography or cryptography alone has some limitation to secure the data communication system. So, combining them together can give a strong security system. Steganography will protect the transmitted data against the suspicion of the attacker by hiding it in a cover image and cryptography will protect the confidentiality of the transmitted data even though the attacker is able to break down the steganography system. The main contribution of this research is developing a new security system that combines steganography with cryptography in order to provide a secure transition of data over open channels.

In this paper, a new technique for securing data communication systems is proposed by combining cryptography and steganography. For steganography, an enhanced form of LSB algorithm was developed to hide the encrypted data in the cover image. The algorithm is based on a secret key used by the sender and the receiver to determine where to hide the encrypted message. So, it is hard for anyone to extract the embedded data without knowing the secret data. The cryptography technique adopted in this research was Modified Jamal Encryption Algorithm (MJEA), which is proposed by Jamal Bani Salameh [37]. MJEA is a novel symmetric block encryption algorithm; it has a block size of 64 bits and 120-bit key. The design of the algorithm is easy to implement and achieves great performance results according to the avalanche effect when compared with other algorithms. The rest of the paper is organized as follows: Section 2 describes the proposed technique in detail. Section 3 shows the experimental results and discusses the efficiency of the proposed mechanism. Finally, section 4 provides some concluding remarks and future work.

2. DESCRIPTION OF THE PROPOSED SYSTEM

In this research, we proposed a hybrid security system that combines cryptography and steganography techniques in order to provide secure transition of data over unsecure channels. In this section, the proposed technique will be introduced in more detail.

Figure 1 shows a block diagram of the proposed system at the transmitter side. As we see in the figure, the hexadecimal representation of the secret message (Sec-msg) is first encrypted by using MJEA under the control of 120-bit key (Enc-Key), where the output is the encrypted message (Enc-msg). As a double security, the Enc-msg is embedded in a cover image (Cov-Img) to get the stego-image (Steg-Img) by using an enhanced form of LSB embedding algorithm and (128-bit) steganography key (Steg-Key). For more security, the Steg-Key is encrypted using MJEA. The encrypted key and the length of the Enc-msg are embedded in the Cov-Img. The output of the embedding process is the Steg-Img that will be sent over the channel to the other side.

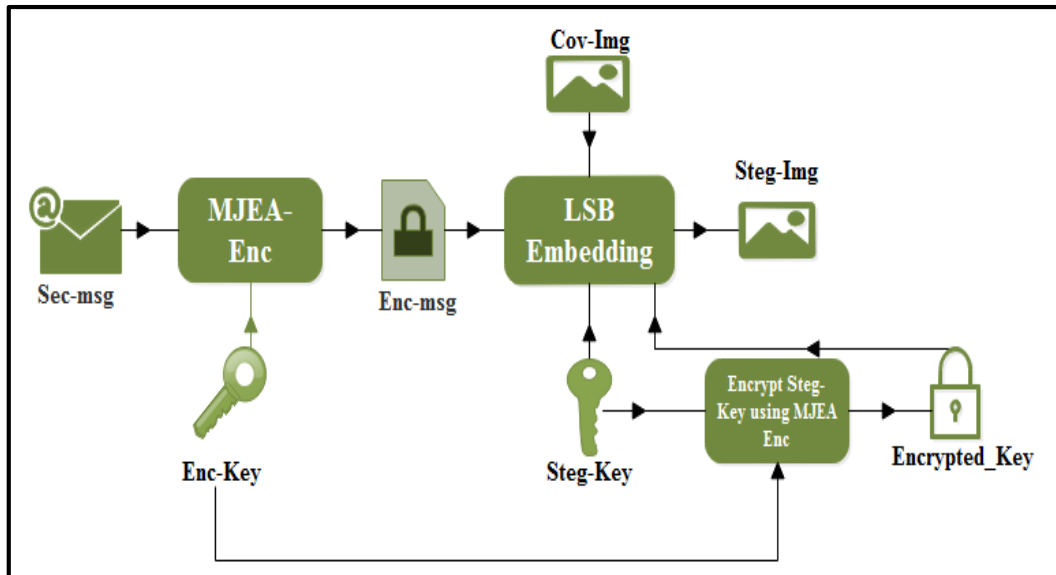


Figure 1. A block diagram of the proposed system at the sender side.

Figure 2 shows a block diagram of the proposed system at the receiver side. The main target for the receiver is to extract the Sec-msg out of the Steg-Img. To do that, the operation is done in a reverse action compared to the transmitter side. The first step in this process is extracting the Enc-Key and the Enc-msg length from the Steg-Img, then using MJEA to decrypt them in order to get the Steg-Key. The LSB extraction algorithm and the Steg-Key are used to extract the Enc-msg from the Steg-Img, then the Enc-msg is decrypted by using MJEA to get back the original Sec-msg that was sent by the sender.

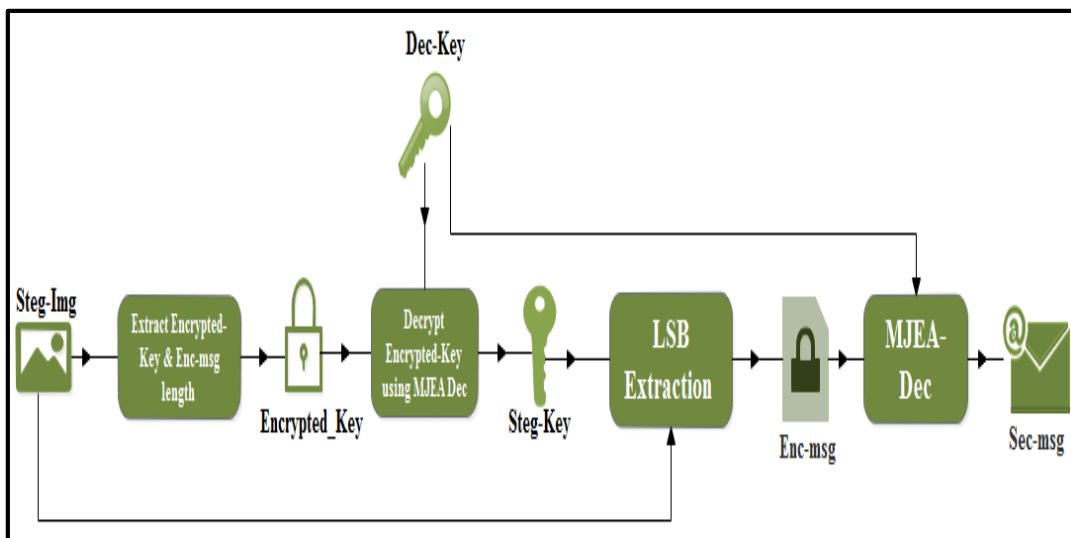


Figure 2. A block diagram of the proposed system at the receiver side.

The proposed system contains four main algorithms: the encryption algorithm, the decryption algorithm, the embedding algorithm and the extraction algorithm. In the following sub-sections, we will give a detailed description of each one of them.

2.1 The Encryption Algorithm

At the sender side, we applied MJEA to encrypt the secret message and the Steg-Key. Figure 3 shows a block diagram of this algorithm. As we see in the figure, MJEA divides the message into (64-bit) blocks, then it encrypts each block separately. All operations in MJEA are XORed on 8-bit words. The 64-bit block of the plain text (Pt) goes in one end of the algorithm, then the algorithm runs to produce the 64-bit cipher text (Ct) at the end. Each (Pt) block is converted into a (Ct) block in 8 rounds under the control of (120-bit) encryption key.

2.2 The Decryption Algorithm

At the receiver side, we applied MJEA algorithm to decrypt the encrypted Steg-Key to get the Steg-Key to be used in the extraction process and to decrypt the encrypted Sec-msg to get the original one that was sent by the transmitter. The decryption algorithm is different from the encryption algorithm in that the S-boxes must be used in the reverse order, as well as the inverse linear transformation and reverse order of the sub-keys. Decryption for MJEA is relatively straightforward beginning with the ciphered text as input which is divided into (64-bit) blocks, then each block is decrypted separately. The (64-bit) block of the Ct goes in one end of the algorithm, and then the algorithm runs to produce the (64-bit) of Pt at the end. Each Ct block is converted into a Pt block in 8-roundes under the control of the same (120-bit) encryption key that was used in the sender side.

2.3 The Embedding Algorithm

This algorithm is used at the sender side to embed the Enc-msg in the least 3-3-2 bits of the Red-Green-Blue components of the Cov-Img under the control of 128-bit Steg-Key. Furthermore, the proposed technique uses the embedding algorithm to hide the encrypted Steg-Key and the message length in the last 17 rows of the Cov-Img array. The full description of the embedding algorithm step by step is shown as a flowchart in Figure 4, which includes the hiding process. As we see in this figure, the inputs for this algorithm are: Enc-msg, Cov-Img, Steg-Key and the Encrypted Steg-Key. The only output out of this algorithm is the Steg-Img that will be sent over the channel to the receiver.

2.4 The Extraction Algorithm

The extraction algorithm takes place at the receiver side. The first step in this algorithm is to extract the (128-bit) Encrypted Steg-Key from the Steg-Img, which will be decrypted by the decryption algorithm to produce the same Steg-Key that was used in the embedding process. This Steg-Key is used in the extraction algorithm to extract the Enc-msg from the Steg-Img. The full description of the extraction algorithm step by step is shown as a flowchart in Figure 5. As we see in this figure, the input for this algorithm is the Steg-Img and the output is the Enc-msg that will be transferred to the decryption algorithm to produce the original Sec-msg that was sent by the transmitter.

3. EXPERIMENTAL RESULTS AND ANALYSIS

The performance of the proposed technique has been evaluated by considering several experimental tests. There are three main metrics that can be used to measure the effectiveness of a given steganography technique: impressibility, embedding capacity and robustness [26].

1. Impressibility: it means that the hidden data cannot be perceived by the human visual system or other statistical means. It is a property in which a person cannot distinguish or detect that the Steg-Img has hidden data.
2. Embedding capacity: it refers to the maximum quantity of secret data that can be hidden inside the cover image without degrading its quality under certain constraints.
3. Robustness: it is the ability of the algorithm to retain the hidden data after many image-related operations, such as cropping, rotating, filtering, compression, etc...

In this research, we used MatLab for simulation, because it supports image processing by using a group of orders under the Image Processing Tool Box.

The evaluation process for the proposed technique will include the following tests:

- Performance analysis of MJEA.

- Visual testing to show how the proposed algorithm works.
- Statistical test, which includes the PSNR (Peak Signal to Noise Ratio) to measure the quality of the image and the MSE (Mean Square Error) to measure the distortion in the image.
- The security test, in which the histogram for all cover images and corresponding Steg-Imgs were calculated then analyzed by comparing them together to see whether the proposed technique is secure against histogram analysis attack.

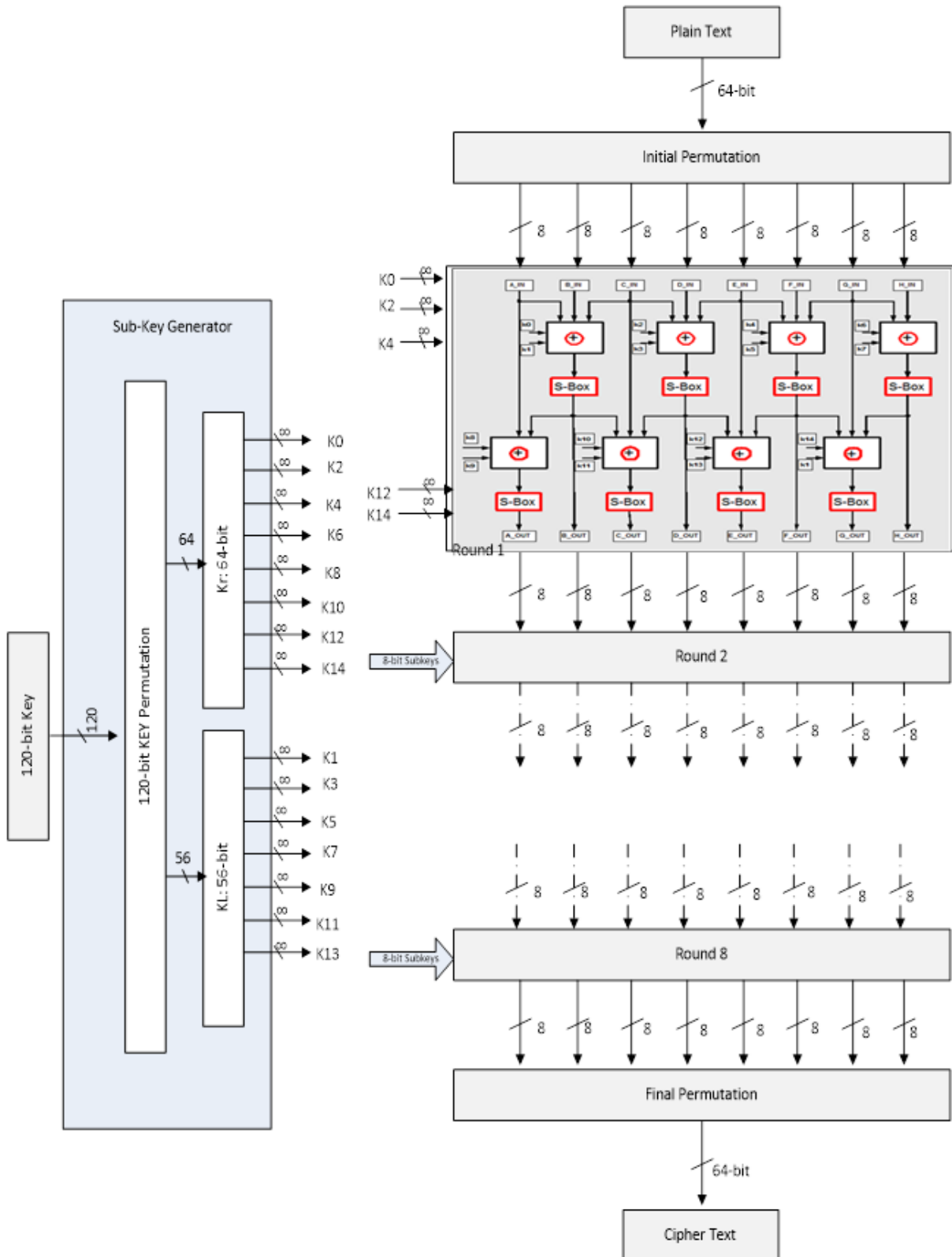


Figure 3. A block diagram of MJEA.

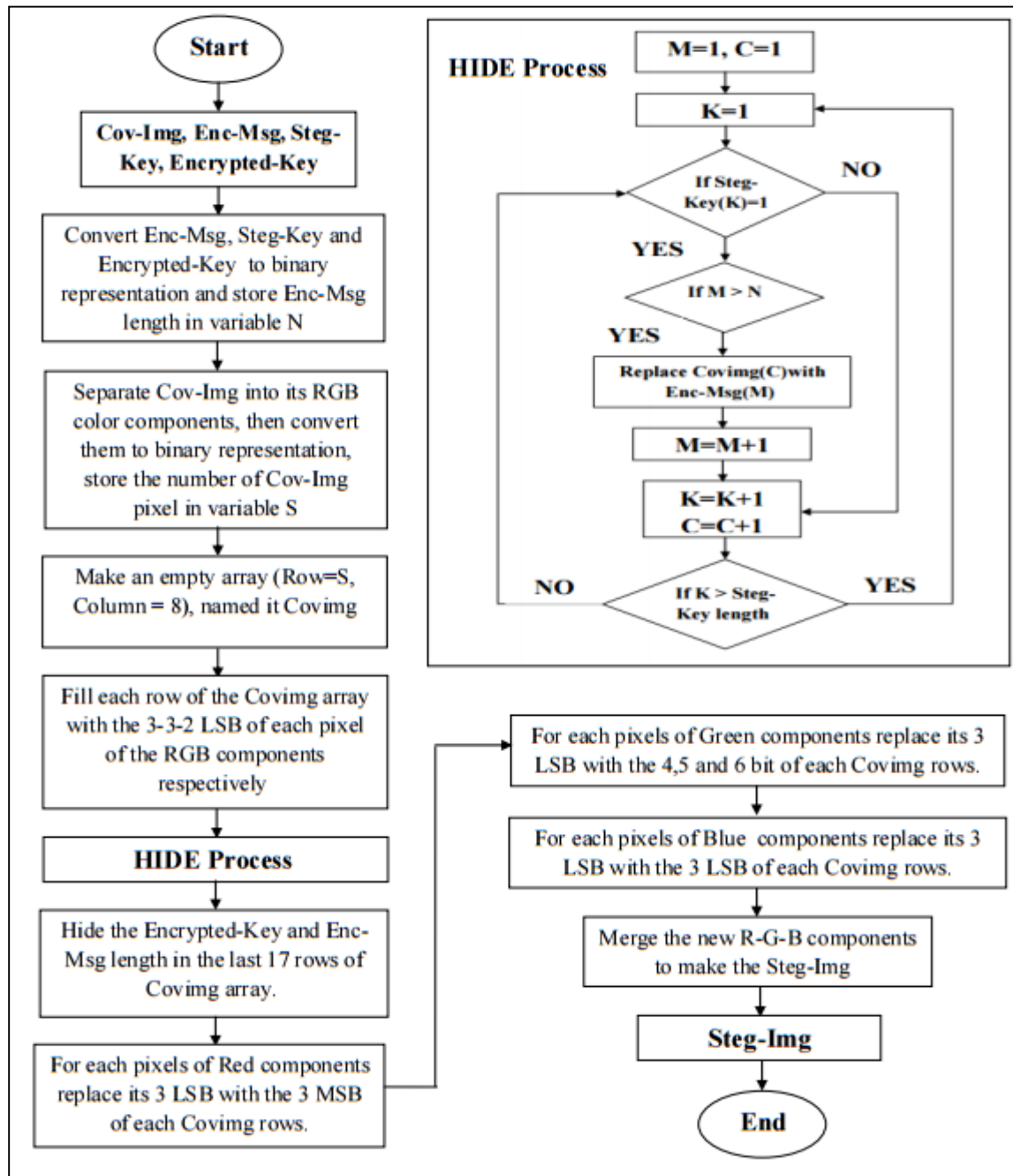


Figure 4. The embedding algorithm.

- Image quality comparison test, in which the proposed algorithm has been compared with other similar LSB algorithms based on PSNR and embedding capacity.

For evaluation purposes, the proposed algorithm was applied on several 24-bit colored PNG (Portable Network Graphic) cover images. This format has been used, because it is a lossless compression technique, which means that the original image will never lose any information when it is compressed during the transmission process over the network. In the following sub-sections, we are going to talk about the simulation results and analysis for all tests conducted.

3.1 Performance Analysis of MJEA

The performance of MJEA was evaluated through a number of experiments in [37]-[38]. MJEA has been analyzed considerably as plain text encryption algorithm through a series of simulation tests. The algorithm thoroughly scrambles the plaintext with the key when run for at least four rounds. MJEA achieved a good Avalanche Effect when tested separately; on average, more than 50% of bits were

changed when we change a bit in the plaintext, key or the ciphertext. A comparison has been conducted between MJEA and different encryption algorithms. Simulation results clearly showed the superiority of MJEA over the other encryption algorithms in terms of Avalanche Effect [37]. Also, MJEA has been analyzed considerably as image encryption algorithm [38]. Experimental results show the possibility of applying MJEA to encrypt digital images. The algorithm was able to achieve high embedding capacity and high quality of encoded image. It was able to replace and transform all pixels in the original-image. On the other side, there was no loss of the image quality after performing the decryption process.

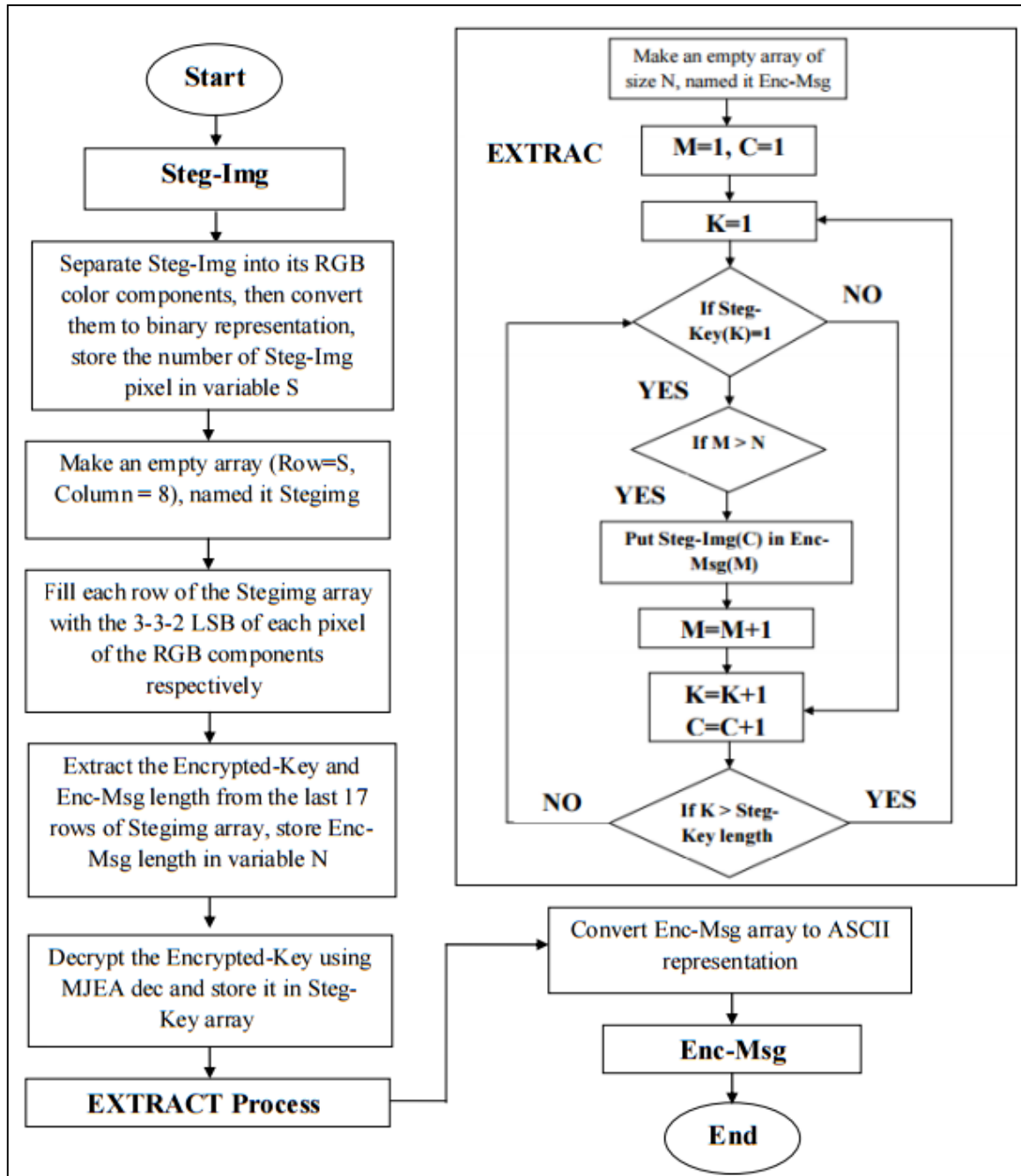


Figure 5. The extraction algorithm.

3.2 Visual Testing for the Proposed Method

In this sub-section, we carried out a series of experiments to show the effectiveness and the correctness of the proposed technique. To do that, we need to prove that the sender is able to hide the secret message in the cover image without being perceived by the human visual system and the receiver is able to extract the secret message from the Steg-Img without any loss. Here, we use three PNG images with different sizes: the first one is Pepper image with (256*256) pixels, the second one is Lena image with (512*512)

pixels and the third one is Animal image with (1024 *1024) pixels. For all experiments, we used the following keys:

The Steg-Key: 88aaa66bbb00ccc77ddd88eee99fff11

The Enc-Key: 111222333444555a666777888999bc

To show the effect of the embedding process on the Cov-Imgs, 2012-byte data representing the Enc-msg is embedded in the three tested Cov-Imgs. The first experiment is done on Pepper image. Figure 6 shows the results at the sender side. Figure 6a shows a sample of the Sec-msg to be encrypted and embedded in a Cov-Img, then transmitted to the receiver. Figure 6b shows a sample of the encrypted Sec-msg. As we see in this figure almost every single bit in the Sec-msg is changed. Figure 6c shows the Cov-Img. Figure 6d shows the Pepper Steg-Img which hides the Enc-msg plus the encrypted Steg-Key. This image will be sent to the receiver side.

4162737472616374 2D496E2074686973 2070617065722C20 616E20696D70726F 76656D656E742069 6E2074686520706C 61696E204C534220 62617365640D0A69 6D61676520737465 67616E6F67726170 6879206973207072	f89b6dfd5a70dd2a c05abe57439b3e5f 6361d471 feecf21 1c35ea227bb556b1 a42d663b7d26f782 2d381820a114dd60 6cc7bb4ff91bb9d9 6adc086d5626605 98f47083dd57fd63 d664e68470562213 2d4d2a6a5b63a89a
a) Sec-msg	b) Enc-msg
	
c) Pepper Cov-Img	d) Pepper Steg-Img

Figure 6. Testing Pepper image at the sender side.

Figure 7 shows the result at the receiver side. Figure 7a shows the Pepper Steg-Img which holds the Enc-msg plus the encrypted Steg-Key that was received from the sender side. Figure 7b shows a sample of the Enc-msg after it was extracted from the Steg-Img by using modified LSB and the help of the Steg-Key. Figure 7c shows a sample of the recovered Sec-msg after it was decrypted by using MJEA and with the help of decryption key. As we see in this figure, the recovered message is exactly the same as the original secret message without any loss.

The second experiment is carried out on Lena image. Figure 8 shows the result at the sender side and Figure 9 shows the result at the receiver side. In this experiment, we repeated the same scenario as we did on Pepper image and found that the receiver was able to recover the Sec-msg that was exactly the same as the original one.

The third experiment is carried out on Animal image. We repeat the same scenario done in the previous two experiments. Figure 10 shows the result at the sender side and Figure 11 shows result at the receiver

side. As we see in those figures, the receiver was able to recover the Sec-msg that was exactly the same as the original one.

	f89b6dfd5a70dd2a c05abe57439b3e5f 6361d471 feecf21 1c35ea227bb556b1 a42d663b7d26f782 2d381820a114dd60 6cc7bb4ff91bb9d9 6adc086d5626605 98f47083dd57fd63 d664e68470562213 2d4d2a6a5b63a89a	4162737472616374 2D496E2074686973 2070617065722C20 616E20696D70726F 76656D656E742069 6E2074686520706C 61696E204C534220 62617365640D0A69 6D61676520737465 67616E6F67726170 6879206973207072
a) Pepper Steg-Img	b) Encrypted Sec-msg	c) Sec-msg

Figure 7. Testing Pepper image at the receiver side.

4162737472616374 2D496E2074686973 2070617065722C20 616E20696D70726F 76656D656E742069 6E2074686520706C 61696E204C534220 62617365640D0A69 6D61676520737465 67616E6F67726170 6879206973207072	f89b6dfd5a70dd2a c05abe57439b3e5f 6361d471 feecf21 1c35ea227bb556b1 a42d663b7d26f782 2d381820a114dd60 6cc7bb4ff91bb9d9 6adc086d5626605 98f47083dd57fd63 d664e68470562213 2d4d2a6a5b63a89a
a) Sec-msg	b) Enc-msg
	
c) Lena Cov-Img	d) Lena Steg-Img

Figure 8. Testing Lena image at the sender side.

Based on the results shown in the figures above, we can note the following:

- At the sender side, the Steg-Imgs and the Cov-Imgs look intact, which means that the hidden data cannot be perceived by the human visual system, which is a good feature of the proposed technique.
- At the receiver side, we were able to extract the Sec-msg from the Steg-Imgs exactly without any loss.

We can conclude from those experiments that the proposed technique works correctly.

	<pre>f89b6dfd5a70dd2a c05abe57439b3e5f 6361d471 feecf21 1c35ea227bb556b1 a42d663b7d26f782 2d381820a114dd60 6cc7bb4ff91bb9d9 6adc086d5626605 98f47083dd57fd63 d664e68470562213 2d4d2a6a5b63a89a</pre>	<pre>4162737472616374 2D496E2074686973 2070617065722C20 616E20696D70726F 76656D656E742069 6E2074686520706C 61696E204C534220 62617365640D0A69 6D61676520737465 67616E6F67726170 6879206973207072</pre>
a) Lena Steg-Img	b) Encrypted Sec-msg	a) Sec-msg

Figure 9. Testing Lena image at the receiver side.

<pre>4162737472616374 2D496E2074686973 2070617065722C20 616E20696D70726F 76656D656E742069 6E2074686520706C 61696E204C534220 62617365640D0A69 6D61676520737465 67616E6F67726170 6879206973207072</pre>	<pre>f89b6dfd5a70dd2a c05abe57439b3e5f 6361d471 feecf21 1c35ea227bb556b1 a42d663b7d26f782 2d381820a114dd60 6cc7bb4ff91bb9d9 6adc086d5626605 98f47083dd57fd63 d664e68470562213 2d4d2a6a5b63a89a</pre>
a) Sec-msg	b) Enc-msg
	
c) Animal Cov-Img	d) Animal Steg-Img

Figure 10. Testing Animal image at the sender side.

3.3 Statistical Test

The statistical measurements that will be used in this test are PSNR (Peak Signal to Noise Ratio) and MSE (Mean Square Error) measurements. PSNR is a measure of the quality of the image and is measured by comparing the Cov-Img with the Steg-Img. It is calculated by using Equation 1. Higher PSNR value indicates better quality of image (i.e., lower distortion, which decreases the possibility of visual attack by human eyes) [3].

$$\text{PSNR} = 10 \log_{10} \left(\frac{\text{MAX}_i^2}{\text{MSE}} \right) \text{ (dB)} \quad (1)$$

where MAX_i is the maximum value of the samples which is equal to 255 for a monochrome image having 8 bits per pixel and MSE is the mean square error.

MSE defines as the square of error between the Cov-Img and the Steg-Img and is given in Equation 2. Higher value of MSE means more image distortion.

	<pre>f89b6dfd5a70dd2a c05abe57439b3e5f 6361d471 feecf21 1c35ea227bb556b1 a42d663b7d26f782 2d381820a114dd60 6cc7bb4ff91bb9d9 6adc086d5626605 98f47083dd57fd63 d664e68470562213 2d4d2a6a5b63a89a</pre>	<pre>4162737472616374 2D496E2074686973 2070617065722C20 616E20696D70726F 76656D656E742069 6E2074686520706C 61696E204C534220 62617365640D0A69 6D61676520737465 67616E6F67726170 6879206973207072</pre>
a) Animal Steg-Img	b) Encrypted Sec-msg	a) Sec-msg

Figure 11. Testing Animal image at the receiver side.

$$MSE = \frac{1}{M*N} \sum_{i=0}^{M-1} \sum_{j=0}^{N-1} (C(i,j) - S(i,j))^2 \quad (2)$$

where $M*N$ is the image size, $C(i,j)$ is the intensity of the pixel at the Cov-Img and $S(i,j)$ is the intensity of the pixel at the Steg-Img.

To conduct this test, we embedded 2012-byte data representing the Enc-msg in each one of the Cov-Imgs, then we calculated the PSNR and MSE values for all Steg-Imgs produced by the proposed technique with the help of 128-bit Steg-Key. Table 1 shows the results of this test.

Figure 12 shows the results of PSNR and MSE for the three tested images from visualization perspective. The first row shows the Cov-Img's, whereas the second row shows the Steg-Img's after embedding 2012-byte of encrypted data.

Table 1. The PSNR and MSE results.

Images	PSNR	MSE
Pepper (256*256)	57.985	0.14986
Lena(512*512)	64.009	0.03317
Animal(1024*1024)	70.109	0.00820

As seen from the results above, the PSNR values are high and above 50%, which means that the proposed algorithm is strong according to the impressibility test. This result makes it difficult for anyone to notice the existence of hidden data in the Steg-Img. Also, notice that the PSNR value increases as the size of image increases. So, it is recommended to use a bigger size Cov-Img if there is a need to embed a bigger size of Sec-msg. There must be a trade-off between the Cov-Img size and the PSNR value.

3.4 The Embedding Capacity Test

The embedding capacity test calculates the maximum size of the Enc-msg that can be hidden in the Cov-Img and investigates the effect of increasing the size of the Enc-msg on the visual quality of the Steg-Img by calculating its PSNR values. Table 2 shows the maximum embedding capacity for the three cover images (Pepper, Lena and Animal) and Table 3 shows the PSNR and the MSE values for different embedded text sizes that were embedded in the Cov-Imgs.

Figures 13 and 14 show the effect of increasing the embedded text size on the PSNR and MSE values for the Cov-Imgs. Figure 15 shows the effect of increasing the embedded text size on the Steg-Img from a visualization perspective.

As seen from Tables (2-3) and Figures (13-15), the PSNR value decreases as the embedded text size

increases, but the decrease is slow compared to the increase in the text size. When we hide the maximum embedding capacity (32kB text size) in Pepper, we still get a good PSNR result (45dB), still with a good quality image. For Lena and Animal images, the result is still good and accepted and there is an availability to increase the embedded text size up to the maximum size while the quality of the Steg-Img remains good. The MSE results show that Pepper image has the highest value, because we hide the maximum embedding capacity in it. More data embedded in a cover image means more image distortion, which in turn means more MSE values.

		
		
(a) <u>Pepper Img</u> PSNR = 57.985 MSE = 0.14986	(b) <u>Lena Img</u> PSNR = 64.009 MSE = 0.03317	(c) <u>Animal Img</u> PSNR = 70.109 MSE = 0.00820

Figure 12. Results of PSNR and MSE from visualization perspective.

Table 2. Maximum embedding capacity.

Image	Max Embedding Capacity (Byte)
Pepper (256*256)	32768
Lena (512*512)	131072
Animal (1024*1024)	524288

The performance of our algorithm shows a good behavior under the PSNR and MSE tests. The results show that the proposed algorithm has the ability to hide a text size up to the maximum size in the cover images while the quality of the Steg-Img remains accepted without any distortion.

3.5 Security Test

The quality of images could be visually noticed by applying the histogram analysis. In this test, we embedded (2024-byte data) in each one of the Cov-Imgs, then we applied the histogram statistical analysis to get the histograms for all Cov-Imgs and their corresponding Steg-Imgs, whereafter we compared them together.

Table 3. PSNR & MSE values for different text sizes.

Text Size(kB)	Pepper		Lena		Animal	
	PSNR(dB)	MSE	PSNR(dB)	MSE	PSNR(dB)	MSE
1	60.883	0.07543	66.960	0.01667	73.063	0.00405
2	57.985	0.14986	64.009	0.03317	70.109	0.00820
4	54.996	0.29764	61.078	0.06402	67.118	0.01569
8	51.930	0.60484	58.040	0.12784	64.105	0.03171
16	48.989	1.14495	55.048	0.25534	61.061	0.06473
32	45.966	2.21182	52.042	0.50968	58.097	0.12766

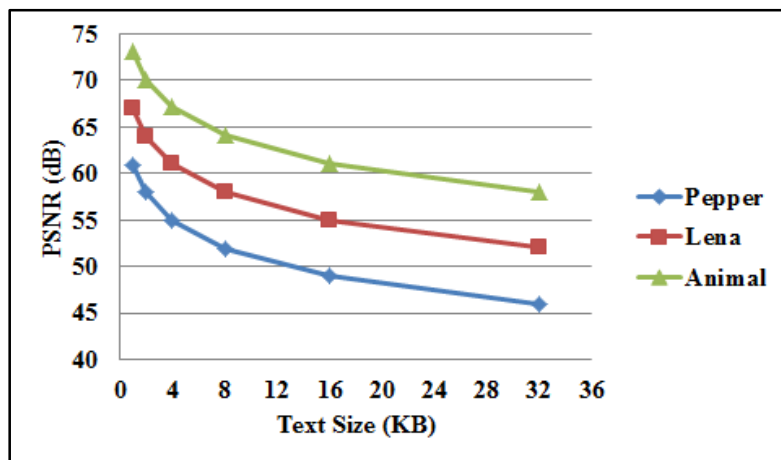


Figure 13. The effect of increasing the embedded text size on the PSNR values.

Figures (16-18) show the histogram analysis for the (Pepper, Lena and Animal) images, where the upper part of each figure represents the histogram analysis for each red, green and blue channel for the Cov-Img and the bottom part represents the histogram analysis for each red, green and blue channel for the Steg-Img. As we can see in all figures, the histograms of the Cov-Imgs look intact with the histograms of the Steg-Imgs. There are no detected visual changes between the original image histograms and the Steg-Img histograms. So, we can say that the proposed technique shows a high degree of security with moderate capacity. This result indicates that it is hard for the steganalyst to notice that there is an embedded text in the Steg-Img by analyzing the histograms of the Cov-Img and comparing them with the Steg-Img histograms. This result means that the proposed technique is secured against histogram analysis attack. To add more security level, a secret Steg-Key is used to determine where to hide the secret text in the Cov-Img, so that if the attacker knows that there is an embedded text in the image it will be hard for him to extract this embedded text unless he knows the Steg-Key.

A further security analysis for the proposed method was carried out by using Kirchhoff's principle [39]-

[40]. This test measures the strength of the algorithm against brute force attack.

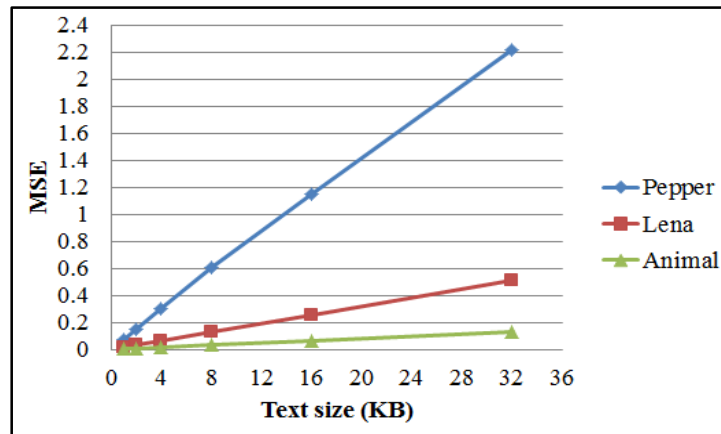


Figure 14. The effect of increasing the embedded text size on the MSE values.

 PSNR= 60.88 MSE= 0.0754	 PSNR=57.985 MSE=0.14986	 PSNR=54.996 MSE= 0.2976	 PSNR=51.930 MSE= 0.6048	 PSNR=48.98 MSE=1.1449	 PSNR=45.966 MSE=2.2118
 PSNR=66.960 MSE=0.0166	 PSNR=64.009 MSE=0.03317	 PSNR=61.078 MSE=0.0640	 PSNR=58.040 MSE=0.1278	 PSNR=55.04M SE=0.2553	 PSNR=52.042 MSE=0.5096
 PSNR=73.063 MSE=0.0040	 PSNR=70.109 MSE=0.00820	 PSNR=67.118 MSE=0.0156	 PSNR=64.105 MSE=0.0317	 PSNR=61.0 MSE=0.0647	 PSNR=58.097 MSE=0.1276
(a) Pepper, Lena and Animal Steg-Img with 1 KB payload	(b) Pepper, Lena and Animal Steg-Img with 2 KB payload	(c) Pepper, Lena and Animal Steg-Img with 4KB payload	(d) Pepper, Lena and Animal Steg-Img with 8KB payload	(e) Pepper, Lena and Animal Steg-Img with 16KB payload	(f) Pepper, Lena and Animal Steg-Img with 32KB payload

Figure 15. The effect of increasing the embedded text size on Steg-Img from visualization perspective.

In this case, the ability of the attacker to break down the system will depend on the length of the used keys. In the proposed system, two keys were used; the Enc-Key (120 bits) and the Steg-Key (128 bits). To calculate the time needed by the attacker to break down the system, we do the following calculation:

- For the cryptography algorithm:

As we know, MJEa is a symmetric cryptography algorithm with (120-bit) key; the attacker needs to produce a 120-bit master key in order to break down this system. This means that the possible number of keys is 2^{120} .

Master key length = 120 bits.

Possible number of keys = 2^{120} .

Assume that the attacker's machine can generate 1 million keys per second.

The time needed to break down the system (years) = $2^{120} / (10^6 * 365 * 86400) = 4.215 * 10^{22}$ (years).

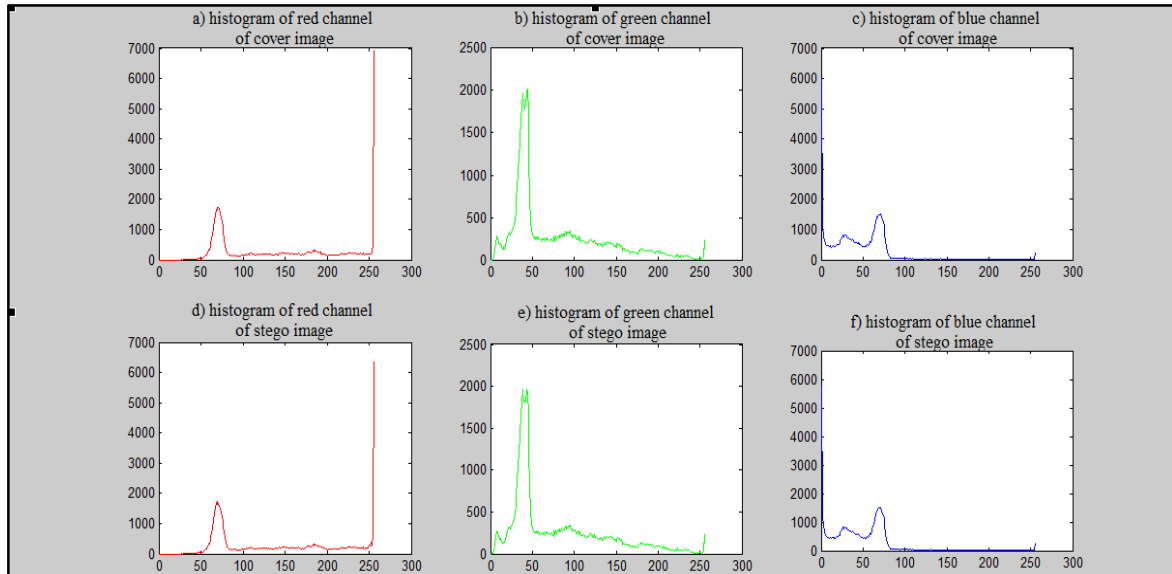


Figure 16. The histogram of the red, green and blue channels of Pepper image.

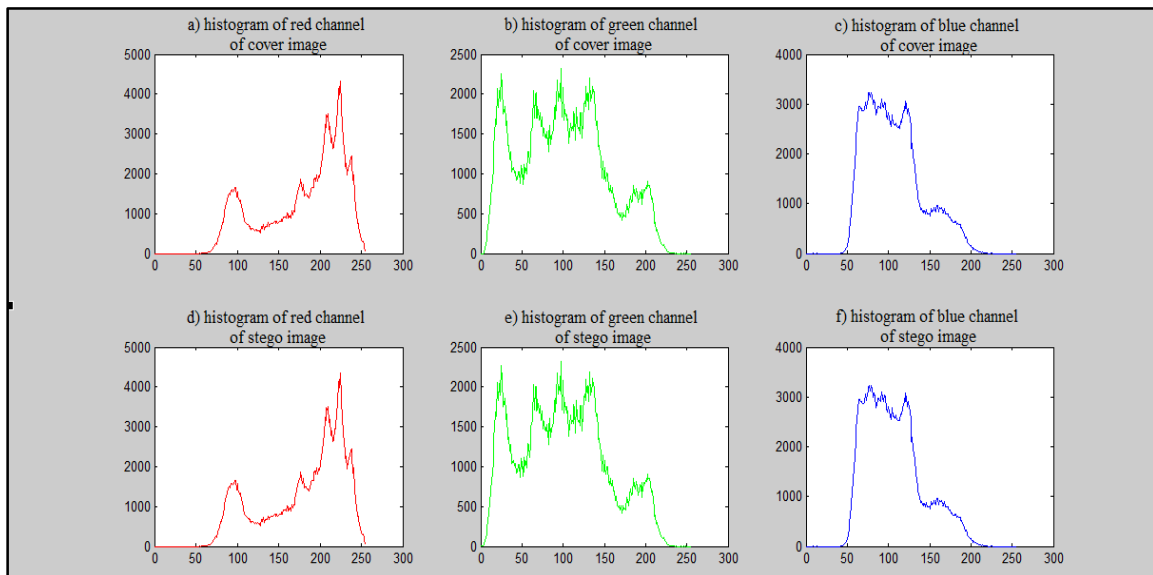


Figure 17. The Histogram of the red, green and blue channels of Lena image.

- For the steganography algorithm:
Our steganography algorithm uses a (128-bit) long steg-key. The attacker needs to produce 128-bit master key in order to break down this system. This means that the possible number of keys is 2^{128} .
Master key length = 128 bits.
Possible number of keys = 2^{128} .
Assume that the attacker's machine can generate 1 million keys per second.
The time needed to break down the system (years) = $2^{128} / (10^6 * 365 * 86400) = 1.079 * 10^{25}$ (years).

This result shows that it takes a very long time from the attacker to break down the system, which indicates that the keys used in the proposed system is strong enough to keep the system secure against brute-force attack.

3.6 Comparison of the Proposed Technique with Other LSB Algorithms

An image quality comparison between the proposed technique and other LSB algorithms similar to our work has been conducted. The nearest works to our proposed algorithm that use LSB steganography technique are: Masud, Saifur and Ismail algorithm, Adnan Gutub algorithm and Amritpal and Harpal

algorithm. Our algorithm will be compared with those algorithms in terms of PSNR and maximum embedded capacity. In order to do this, comparison of the codes for all algorithms is implemented in MatLab. We took the same experimental metrics for all algorithms under the same simulation environment and used the same cover images (Pepper, Lena and Animal) for all algorithms.

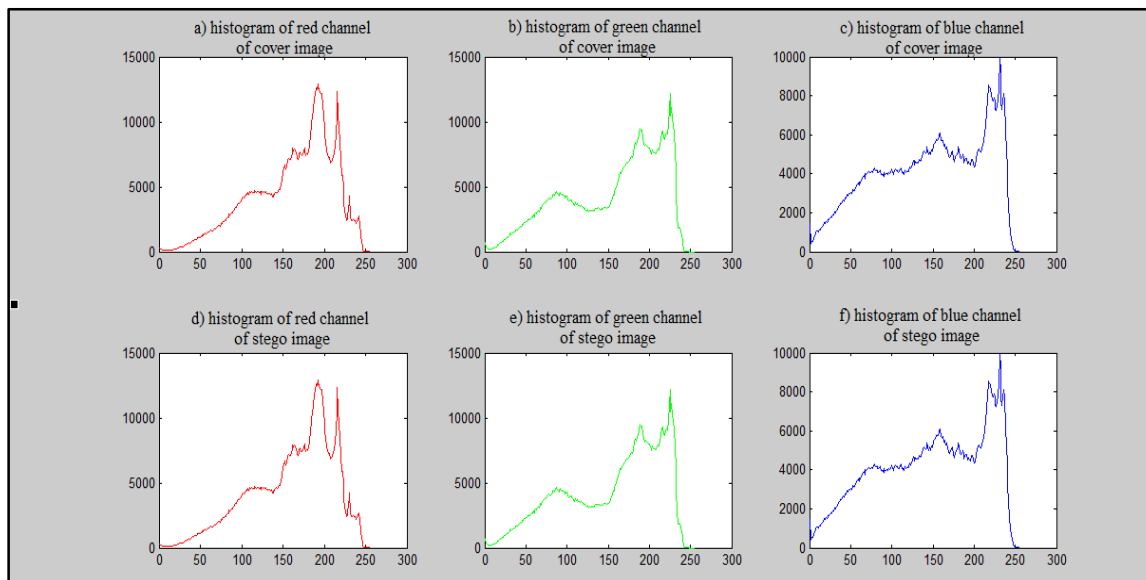


Figure 18. Histogram of the red, green, and blue channels of Animal image.

The first test will be carried out by comparing all algorithms in terms of PSNR. To do this, we embedded (2024-byte) data representing the Enc-msg in each one of the Cov-Imgs. Table 4 shows the PSNR results in dB for all algorithms. The result in the table show that the proposed algorithm has a higher PSNR value with respect to the other algorithms, which means that the quality of the Steg-Img obtained from our algorithm is better than those obtained from the other algorithms. This promising result shows the superiority of our proposed algorithm when compared with other algorithms in terms of PSNR.

The second test will be carried out by comparing all algorithms in terms of payload. To do this we need to calculate the maximum embedded capacity that represents the Enc-msg in each one of the cover images. More embedded capacity in the cover image while still having good visual quality for the Steg-Img means better performance for the algorithm.

Table 5 shows the payload results for all algorithms. It can be noticed from the results shown in the table that the payload of the proposed method is greater than those of the other algorithms except for Amritpal and Harpal algorithm. This result means that this algorithm actually has a greater embedded capacity, but doesn't mean that it is better than our algorithm; it is rather a very simple algorithm with less security because it doesn't have any type of cryptography, the attacker can easily extract the Sec-msg from the Steg-Img.

Table 4. Comparison of the proposed technique with other LSB algorithms using PSNR coefficient in (dB).

Image	Masud,Saifur and Ismail algorithm	Adnan Gutub algorithm	Amritpal and Harpal algorithm	The proposed algorithm
Pepper	59.244	56.361	57.9825	60.055
Lena	64.960	62.431	64.0239	66.252
Animal	70.964	68.103	69.9610	72.311

Table 5. Comparison of the proposed technique with other LSB algorithms using payloads in (byte).

Image	Masud,Saifur and Ismail algorithm	Adnan Gutub algorithm	Amritpal and Harpal algorithm	The proposed algorithm
Pepper	16384	16495	65536	32768
Lena	65536	65903	262144	131072
Animal	262144	262081	1048576	524288

The promising results obtained in this test show the superiority of our proposed technique with respect to the other algorithms.

As a final note on the performance evaluation process, the proposed algorithm has more security than other algorithms because of using the Steg-Key and cryptography. It is hard to extract the Enc-msg out of the Steg-Img without knowing the Steg-Key and if this happened, the message will be unreadable for the attacker, because it is encrypted. The only way to recover the Sec-msg in this case is to break down the security system by getting the encryption algorithm and the Enc-Key.

4. CONCLUSIONS AND FUTURE WORK

In this research, we proposed a novel technique to secure data communication systems by using cryptography and steganography. We used MJEA encryption algorithm to encrypt the secret message before hiding it in the cover image. For steganography, we used an enhanced form of LSB technique to hide the secret message in the cover image.

To evaluate the performance of our proposed technique, we carried out several experimental tests. From the simulation results, we can conclude the following points:

- Based on the visual testing result, the Steg-Imgs and the Cov-Imgs at the sender side look intact, which means that the hidden data cannot be perceived by the human visual system and the receiver was able to extract the Sec-msgs from the Steg-Imgs exactly without any loss, which means that our proposed technique works correctly.
- The histograms of different cover images and their corresponding Steg-Imgs were found to be intact; there was no difference between them. This means that our algorithm is secured against any attack that uses histogram analysis.
- The proposed technique was able to achieve high embedding capacity and high-quality Steg-Imgs.
- The results of the image quality comparison between the proposed technique and other similar LSB algorithms show the superiority of our technique with respect to the other algorithms in terms of PSNR and embedding capacity.
- The encrypted messages are decrypted successfully without any loss, which means that the decoder is efficiently able to recover the original messages.
- The performance of our algorithm shows a good behavior under the PSNR and MSE tests. The results show that the proposed algorithm has the ability to hide a text size up to the maximum size in the cover images while the quality of the Steg-Img remains accepted without any distortion.

Some further research areas could be investigated to improve the performance of the proposed algorithm, such as:

- Using the proposed algorithm with the transform domain embedding technique trying to improve the robustness of the algorithm and to allow using loss compression image format, such as JPEG.
- Using a 32-bit color image instead of a 24-bit one, which will help in increasing the maximum embedding capacity.

- Trying to use audio or video as cover media instead of images.
- Hiding another format of secret data, such as images.
- Evaluating our proposed method under more performance metrics.

REFERENCES

- [1] A. Gutub, "Social Media & Its Impact on E-governance," The 4th Annual Middle East Smart Cities Summit (ME Smart Cities 2015), Dubai, UAE, December 2015.
- [2] N. A. Al-Otaibi and A. A. Gutub, "2-Layer Security System for Hiding Sensitive Text Data on Personal Computers," Lecture Notes on Information Theory, vol. 2, no. 2, pp. 151-157, Engineering and Technology Publishing, June 2014.
- [3] W. Stallings, *Cryptography and Network Security: Principles and Practice*, Prentice Hall, 2013.
- [4] J. V. Shanta, "Evaluating the Performance of Symmetric Key Algorithms: AES and DES," International Journal of Computational Engineering & Management, vol. 15, no. 4, pp. 43-49, 2012.
- [5] A. Nadeem, "A Performance Comparison of Data Encryption Algorithms," 1st International Conference on Information and Communication Technologies (ICICT), pp. 84-89, 2005.
- [6] N. Alassaf, B. Alkazemi and A. Gutub, "Applicable Light-Weight Cryptography to Secure Medical Data in IoT Systems," Journal of Research in Engineering and Applied Sciences (JREAS), vol. 2, no. 2, pp. 50-58, April 2017.
- [7] A. Gutub and F. A. Khan, "Hybrid Crypto Hardware Utilizing Symmetric-Key & Public-Key Cryptosystems," International Conf. on Advanced Computer Science Applications and Technologies (ACSAT), pp. 116-121, 2012.
- [8] A. Gutub, "Remodeling of Elliptic Curve Cryptography Scalar Multiplication Architecture Using Parallel Jacobian Coordinate System," International Journal of Computer Science and Security (IJCSS), vol. 4, no. 4, pp. 409-425, October 2010.
- [9] A. Gutub, "Efficient Utilization of Scalable Multipliers in Parallel to Compute GF(p) Elliptic Curve Cryptographic Operations," Kuwait Journal of Science & Engineering (KJSE), vol. 34, no. 2, pp. 165-182, December 2007.
- [10] A. A. Gutub, A. Tabakh, A. Al-Qahtani and A. Amin, "Serial vs. Parallel Elliptic Curve Crypto Processor Designs," IADIS International Conference: Applied Computing, pp. 67-74, Fort Worth, Texas, 23-25 October 2013.
- [11] A. A. Gutub, "Preference of Efficient Architectures for GF(p) Elliptic Curve Crypto Operations Using Multiple Parallel Multipliers," International Journal of Security (IJS), vol. 4, no. 4, pp. 46 – 63, 2010.
- [12] A. A. Gutub, "Fast 160-Bits GF(p) Elliptic Curve Crypto Hardware of High-Radix Scalable Multipliers," International Arab Journal of Information Technology (IAJIT), vol. 3, no. 4, October 2006.
- [13] S. Channalli and A. Jadhav, "Steganography an Art of Hiding Data," International Journal of Computer Science and Engineering, vol. 3, pp. 137-141, 2009.
- [14] F. Khan and A. A. Gutub, "Message Concealment Techniques Using Image-based Steganography," 4th IEEE GCC Conference and Exhibition, Gulf International Convention Centre, 2007.
- [15] M. T. Parvez and A. A. Gutub, "Vibrant Color Image Steganography Using Channel Differences and Secret Data Distribution," Kuwait Journal of Science and Engineering (KJSE), vol. 38, no. 1B, pp. 127-142, June 2011.
- [16] W. Abu-Marie, H. Abu-Mansour and A. A. Gutub, "Image-based Steganography Using Truth Table-based and Determinate Array on RGB Indicator," International Journal of Signal and Image Processing (IJSIP), vol. 1, no. 3, pp. 196-204, May 2010.
- [17] N. A. Al-Otaibi and A. A. Gutub, "Flexible Stego-System for Hiding Text in Images of Personal Computers Based on User Security Priority," International Conf. on Advanced Engineering Technologies (AET-2014), pp. 250-256, 2014.
- [18] A. A. Gutub, A. Al-Qahtani and A. Tabakh, "Triple-A: Secure RGB Image Steganography Based on Randomization," 7th ACS/IEEE International Conference on Computer Systems and Applications, pp. 400-403, 2009.

- [19] S. Hemalatha, U. Dinesh Acharya and A. Renuka, "Comparison of Secure and High Capacity Color Image Steganography Techniques in RGB and YCbCr Domains," *International Journal of Advanced Information Technology*, vol. 3, no. 3, 2013.
- [20] M. Kalita and T. Tuithung, "A Comparative Study of Steganography Algorithms of Spatial and Transform Domain," *International Journal of Computer Applications*, no. 1, pp. 9-14, 2016.
- [21] N. Alotaibi, A. A. Gutub and E. Khan, "Stego-System for Hiding Text in Images of Personal Computers," *The 12th Learning and Technology Conference (Wearable Tech/ Wearable Learning)*, Effat University, Jeddah, KSA, April 2015.
- [22] A. A. Gutub, M. Ankeer, M. Abu-Ghalioun and A. K. Alvi, "Pixel Indicator High Capacity Technique for RGB Image-based Steganography," *5th IEEE International Workshop on Signal Processing and Its Applications*, University of Sharjah, U.A.E., 18 – 20 March 2008.
- [23] K. Muhammad, M. Sajjad, I. Mehmood, S. Rho and S. W. Baik, "Image Steganography Using Uncorrelated Color Space and Its Application for Security of Visual Contents in Online Social Networks," *ELSEVIER, Future Generation Computer Systems*, 2016.
- [24] N. Akhtar, P. Johri and S. Khan, "Enhancing the Security and Quality of LSB Based Image Steganography," *5th IEEE International Conference on Computational Intelligence and Computer Networks*, pp. 385-390, September 2013.
- [25] R. Kaur and B. Singh, "Survey and Analysis of Various Steganographic Techniques," *International Journal of Engineering Science & Advanced Technology*, vol. 2, no. 3, pp. 561-566, 2012.
- [26] C. P. Sumathi, T. Santanam and G. Umamaheswari, "A Study of Various Steganographic Techniques Used for Information Hiding," *International Journal of Computer Science & Engineering Survey*, vol. 4, no. 6, pp. 9-25, December 2013.
- [27] S. M. Masud Karim, M. Saifur Rahman and M. Ismail Hossain, "A New Approach for LSB Based Image Steganography Using Secret Key," *14th IEEE International Conference on Computer and Information Technology*, Dhaka, Bangladesh, 22-24 Dec. 2011.
- [28] A. Gutub, "Pixel Indicator Technique for RGB Image Steganography," *Journal of Emerging Technologies in Web Intelligence*, vol. 2, no. 1, Feb. 2010.
- [29] A. Singh and H. Singh, "An Improved LSB Based Steganography Technique for RGB Images," *IEEE International Conference on Electrical, Computer and Communication Technologies*, 5-7 March, Coimbatore, India, 2015.
- [30] M. Juneja and P. S. Sandhu, "Designing of Robust Image Steganography Technique Based on LSB Insertion and Encryption," *International Conference on Advances in Recent Technologies in Communication and Computing*, pp. 302-305, 2009.
- [31] K. Joshi and R. Yadav, "A New LSB-S Image Steganography Method Blend with Cryptography for Secret Communication," *3rd IEEE International Conference on Image Information Processing*, pp. 86-90, 2015.
- [32] Y. Renner, Z. Zhiwei, T. Shun and D. Shilei, "Image Steganography Combined with DES Encryption Pre-processing," *6th International Conference on Measuring Technology and Mechatronics Automation*, pp. 323-326, Wagnaghat, India, 21-24 Dec. 2014.
- [33] S. Ushll, G. A. Sathish Kumal and K. Boopathyagan, "A Secure Triple Level Encryption Method Using Cryptography and Steganography," *International Conference on Computer Science and Network Technology*, pp.1017-1020, 2011.
- [34] G. Sai Charan, N. Kumar, B. Karthikeyan, V. Yanathan and K. Lakshmi, "A Novel LSB Based Image Steganography with Multi-Level Encryption," *International Conference on Innovations in Information, Embedded and Communication Systems (ICIIECS)*, Coimbatore, India, 19-20 March 2015.
- [35] S. Ahmed Laskar and K. Hemachandran, "High Capacity Data Hiding Using LSB Steganography and Encryption," *International Journal of Database Management Systems*, vol. 4, no. 6, pp. 57-62, 2012.
- [36] K. Muhammad, M. Sajjad, I. Mehmood, S. Rho and S. Wook Baik, "A Novel Magic LSB Substitution Method (M-LSB-SM) Using Multi-Level Encryption and Achromatic Component of an Image," *Multimedia Tools and Applications*, vol. 75, no. 22, pp. 14867-14893, Nov. 2016.
- [37] J. N. Salameh, "A New Symmetric-Key Block Ciphering Algorithm," *Middle-East Journal of Scientific Research*, vol. 12, no. 5, pp. 662-673, 2012.

- [38] J. N. Bani Salameh, "An Investigation of the Use of MJEA in Image Encryption," WSEAS Transactions on Computers, vol. 15, pp. 12-23, January 2016.
- [39] K. Muhammad, J. Ahmad, N. Ur Rehman, Z. Jan and M. Sajjad, "CISSKA-LSB: Color Image Steganography Using Stego-key-directed Adaptive LSB Substitution Method," Springer US, Multimedia Tools and Applications, vol. 76, no. 6, pp. 8597-8626, April 2016.
- [40] K. Muhammad, M. Sajjad and S. W. Baik, "Dual-Level Security Based Cyclic18 Steganographic Method and Its Application for Secure Transmission of Key Frames During Wireless Capsule Endoscopy," Springer US, Journal of Medical Systems, May 2016.

ملخص البحث:

هناك تقنيات مختلفة لتحقيق أمن البيانات، أبرزها وأوسعها انتشاراً التشفير والاختزال. يعمل التشفير على تغيير البيانات التي شكل آخر تتعذر قراءته إلا من جانب المستقبل المقصود. أما الاختزال فيخفي وجود بيانات سرية في وسيط تغطية بحيث لا يمكن لأحد كشف البيانات المخفية سوى المستقبل. تم اقتراح تقنية جديدة في هذه الورقة لضمان أمن البيانات في أنظمة الاتصال عبر المزاجية بين التشفير والاختزال. لأغراض التشفير، استخدمنا خوارزمية جمال المعدلة (MJEA). كما قمنا بتصميم نسخة محسنة من خوارزمية للاختزال.

لقد جرى تقييم أداء التقنية المقترحة بإجراء عدة اختبارات تجريبية، مثل: اختبار الحساسية، واختبار سعة التضمين، واختبار الأمان. ولهذه الغاية، تم تطبيق التقنية المقترحة على عدة صور تغطية ملونة. وقد أثبتت النتائج التجريبية جميعها قوة الخوارزمية المقترحة في ضمان انتقال البيانات عبر القنوات غير الآمنة وحمايتها من أي هجمات.

علاوة على ذلك، أظهرت نتائج المحاكاة تفوق الخوارزمية المقترحة على عدد من الخوارزميات الأخرى التي اقترحها باحثون آخرون من حيث نسبة الإشارة إلى الضجيج وسعة التضمين، الأمر الذي يؤكد نجاعة التقنية المقترحة في هذا البحث في نقل البيانات عبر قنوات الاتصال بأمان.

EFFECT OF MULTIPLEXER/DEMULTIPLEXER BANDWIDTH ON UPGRADING CURRENT 10G TO 40G OPTICAL COMMUNICATION SYSTEMS

A. Atieh¹, M. Wa'ad² and I. Mansour²

(Received: 16-Jun.-2017, Revised: 30-Jul.-2017, Accepted: 02-Aug.-2017)

ABSTRACT

Many current 10G optical systems need to be upgraded to higher data rates (for example 40G, 100G, etc...), in order to satisfy the increased demand for higher bandwidth. However, many system providers in the third world countries have limited budgets and could not just replace all equipment to upgrade their systems. Thus, it is important to investigate what equipment could still be used in the upgraded system. In other words; which equipment could be used for both 10G and higher data rate transmitters? The bandwidth of the passive modules is a crucial specification that enables optical communication systems. Therefore, the effect of multiplexer (MUX) and demultiplexer (DEMUX) bandwidth on the performance of hybrid 10G/40G optical communication systems is investigated in this work. Hybrid optical systems enable adding new channels with higher data rate on current 10G common equipment. Numerical simulations are conducted on eight consecutive dense wavelength division multiplexing (DWDM) channels selected on 100-GHz ITU-grid each carrying data rate of 10 Gbps or 40 Gbps. Different loading configurations of wavelengths with data rates are considered in this work. In addition, different MUX/DEMUX bandwidths of 40, 50, 60 and 70 GHz are used to investigate the performance of each selected hybrid system configuration. It is found that the optimal MUX/DEMUX bandwidth for all investigated hybrid configurations is 60 GHz. The hybrid system performance is evaluated for both return-to-zero (RZ) and non-return-to-zero (NRZ) pulse format. The maximum reach of a selected hybrid configuration is also numerically investigated using circulating loop configuration for both RZ and NRZ pulse formats.

KEYWORDS

Effect of MUX/DEMUX bandwidth on signal transmission, Hybrid optical fiber communication, Upgrading 10G to 40G systems, Dispersion and non-linearity interaction in optical fibers.

1. INTRODUCTION

The demand for new services which are bandwidth hungry is increasing all over the world. These services include education on demand, interactive video gaming, IP-TV, voice over IP, high definition TV, video on demand, video conferencing, video surveillance etc... Optical fiber cables offer huge bandwidths which can be exploited to support such services. Commercial optical fiber communication systems are implemented in long haul, metropolitan and access area networks to support the required bandwidths [1]-[3]. The bandwidth of an optical communication system is typically increased by either deploying new systems with higher data rates or upgrading current systems. The later technique can be achieved by increasing the number of wavelengths used on an existing wavelength plan with each wavelength having the same data rates or by using different data rate for the different wavelengths. Using different data rates in a system at different wavelengths is known as a hybrid communication system, which is also known a heterogeneous system [4]-[7]. Commercial DWDM systems are deployed initially with channels carrying lower data rate (10G), then upgraded using wavelengths carrying 40G data rate. Different methods have been proposed in the literature to enable hybrid communication systems: flexible reconfigurable optical add/drop multiplexer (ROADM) bandwidths [8], coherent modulation schemes for 40G and 100G rates [9] and group delay management technique [10]. Already published techniques did not investigate the optimal bandwidth of MUX and DEMUX that could be

1. A. Atieh is with Electrical Engineering Department, University of Jordan, Amman, Jordan. Email: akatieh@hotmail.com.

2. M. Wa'ad and I. Mansour are with Electronics and Communications Engineering Department, Al-Ahliyya Amman University, Jordan.

used to enable hybrid communication systems.

Typically, ON/OFF keying modulation scheme is used for 10G optical communication systems, which also use non return-to-zero (NRZ) pulse format. However, advanced modulation schemes are used for 40G and 100G systems such as differential phase-shift keying (DPSK) and dual-polarization quadrature phase shift keying (DP-QPSK) [11]-[12]. DP-QPSK systems can be implemented employing duobinary or return-to-zero (RZ) pulse formats with different pulse width to bit periods [13]-[14].

Signals carrying different data rates in a hybrid optical communication system travel through the same optical fiber and use the same passive and active optical modules. Usually, lower data rate signals are deployed at earlier stages in any commercial system. Then, higher data rate signals are added to the system. The added signals have different modulation bandwidths and require different passives' bandwidths. In addition, the interaction of dispersion and non-linearity for each signal will be different depending on its location on the ITU-grid, optical fiber dispersion slope and fiber zero-dispersion wavelength. Thus, each signal will have different performance which must be taken into account in designing and operating newly upgraded systems. The interaction of dispersion and non-linearity in optical fiber is investigated for optical communication systems with independent 10G or 40G modulated signals and for a single MUX/DEMUX bandwidth [15]-[18]. The interaction for hybrid communication system is not published -to the best of our knowledge- and cannot be foreseen. Therefore, numerical simulations are conducted to study hybrid system performance due to fiber dispersion and non-linearity interaction.

In this work, the effect of MUX/DEMUX bandwidth on the performance of 10G/40G data rate hybrid optical communication system is investigated using Optisys software from Optiwave, Inc. Although very high data rate systems (100G, 200G) exist commercially in the market [19]-[20], there is still a great need for such investigation, especially for system providers who have limited budgets available to upgrade their current 10G systems into higher data rate systems. The upgrade could be implemented by carrying higher data rate signals (40G) on wavelengths distributed over the same common equipment used for the 10G system.

MUX/DEMUX bandwidths of 40, 50, 60 and 70 GHz are used in the investigation. Commercial 10G MUX/DEMUX passband bandwidth differs from vendor to vendor and from technology to technology. An example of an arrayed waveguide MUX 3-dB passband bandwidth parameter is 50 GHz (0.4 nm). Numerical simulations are conducted at different MUX/DEMUX bandwidths to evaluate the system performance for different hybrid configurations listed in Table 1. Return-to-zero (RZ) and non return-to-zero (NRZ) pulse formats are used in this investigation. The system performance of different hybrid configurations is compared with standard standalone 10G and 40G communication systems. A circulating loop configuration is also used in the simulation to investigate the maximum propagating distance of signals for a selected hybrid communication system using RZ and NRZ pulse formats.

2. HYBRID SYSTEM CONFIGURATION

Figure 1 shows the block diagram of the hybrid optical communication system used in the numerical simulations. Eight neighboring DWDM channels on a 100-GHz ITU-grid are selected around 1550.12nm with a linewidth of 10 MHz. Each channel carries either 10 Gbps or 40 Gbps data rate, depending on the selected hybrid configuration as listed in Table 1. The laser center wavelength is assumed stable and no drifting is considered in this work. A dispersion compensating fiber (DCF) piece with a dispersion of -85 ps/(km.nm) at 1550 with a dispersion slope of -0.3 ps/(km.nm²) is used in the simulation. The used DCF piece offsets the dispersion accumulated by the single mode fiber (SMF) piece which has a dispersion of 17 ps/(km.nm) at 1550 nm with a dispersion slope of 0.075 ps/(km.nm²). Two erbium-doped fiber amplifiers (EDFA) are used to compensate the attenuation in the fiber link due to SMF and DCF pieces which have attenuation of 0.2 dB/km and 0.5 dB/km, respectively. The EDFA noise figure (NF) is set to 6 dB. The EDFA NF parameter affects the overall system performance at the receiver, which is defined by optical signal-to-noise ratio (OSNR). The laser continuous wave (CW) power launched into the modulator is set to 4 dBm. The MUX and DEMUX modules are assumed lossless with Bessel filter shape of second order. Adjacent channels crosstalk of the MUX/DEMUX is assumed 30 dB. The bandwidth of the MUX/DEMUX pair is varied (40, 50, 60 and 70 GHz) to

investigate its effect on the performance of each channel in hybrid optical communication systems. A Mach-Zehnder external modulator is used to modulate ON/OFF keying (OOK) pseudo-random bit sequence using NRZ and RZ pulse formats. The chirp of the modulator is set to zero and the sequence length is 11 bits. The power level of the eight channels at the output of the modulator for H 10 - 40 hybrid configuration is shown in Figure 2. The variation in power level for the different channels is due to wavelength-dependent modulator transfer function. At the receiver end, an optical attenuator is used to control the received power level launched into the bit error-rate (BER) tester in order to create waterfall BER curves. A pin detector with low-pass filter is used as a receiver.

Table 1. Different 10G/40G hybrid and standalone configurations.

Configurations	Names
10-10-10-10-10-10-10-10	R 10
40-40-40-40-40-40-40-40	R 40
10-40-10-40-10-40-10-40	H 10 - 40
10-10-40-40-10-10-40-40	H 2 10 - 2 40
40-40-10-10-40-40-10-10	H 2 40 - 2 10
10-10-10-10-40-40-40-40	H 4 10 - 4 40
40-40-40-40-10-10-10-10	H 4 40 - 4 10

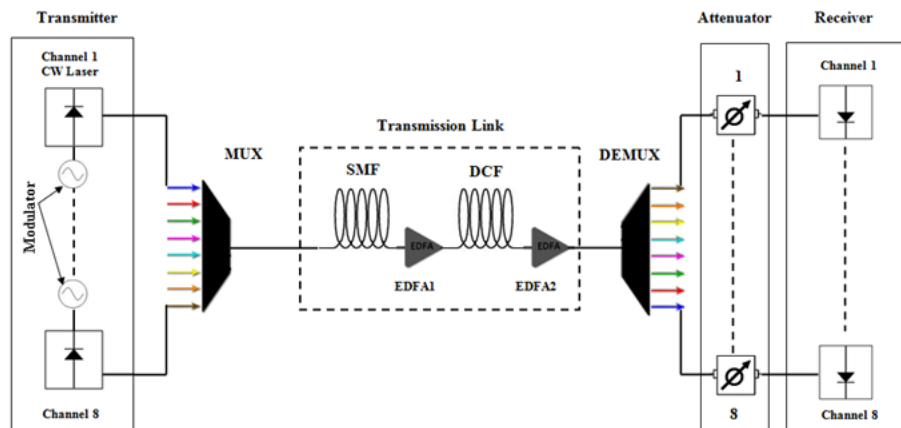


Figure 1. Optical communication system used in the simulations. EDFA: erbium-doped fiber amplifier; SMF: single mode fiber; DCF: dispersion compensated fiber; CW: continuous wave; MUX: multiplexer; DEMUX: demultiplexer.

3. MUX/DEMUX BANDWIDTH EFFECT

The bandwidth of propagated optical signals in the fiber depends on their data rate and the pulse format used. The optical bandwidth equals the signal data rate for NRZ pulse format. However, the bandwidth of an optical signal that uses RZ pulse format depends on pulse duty cycle; 50% of the duty cycle RZ pulses occupy twice the bandwidth of NRZ pulses for the same data rate. Thus, an optical modulated signal at 10Gbps using NRZ pulses occupies 10GHz bandwidth. When the MUX/DEMUX bandwidth is larger than the modulated signal bandwidth, no distortion is acquired after

"Effect of Multiplexer/Demultiplexer Bandwidth on Upgrading Current 10G to 40G Optical Communication Systems", A. Atieh, M. Wa'ad and I. Mansour.

multiplexing/demultiplexing processes. Nevertheless, it is not beneficial to use larger MUX/DEMUX bandwidths to avoid passing through more noise with the optical signal. Therefore, it is important to optimize the MUX/DEMUX bandwidth used.

Figure 3 shows the simulated BER performance of H 10 – 40 hybrid configuration at 60 GHz MUX/DEMUX bandwidth. The odd channels carry 10 Gbps data, while the even channels carry 40 Gbps data. It is clear that the BER performance differs from channel to channel for the same data rate. Table 2 illustrates a summary of the total differences between each group of 10G and 40G channels for different MUX/DEMUX bandwidths. The total performance difference among the same channels will be defined in this work as “range penalty”. Table 2 also shows the “center received power” of each group of channels. These simulations were repeated for all configurations listed in Table 1. Figure 4 and Figure 5 show, respectively, the range penalty and received power center for different hybrid configurations.

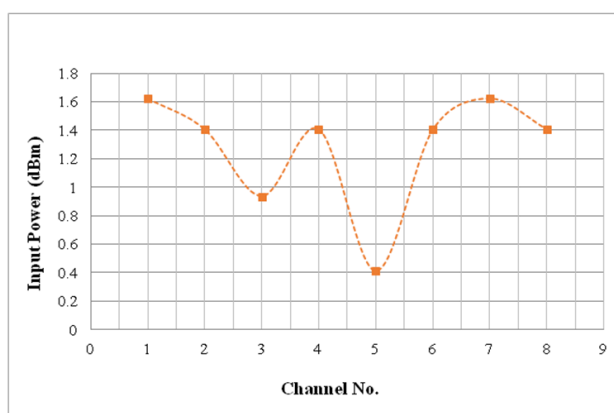


Figure 2. Channels' power levels at the output of the Mach-Zehnder modulator for H 10 – 40 hybrid configuration.

It is clear that each channel has different performance, which is mainly due to its wavelength and relative dispersion at that wavelength. Also, the power level of each wavelength is different, as shown in Figure 2. Therefore, the dispersion and non-linearity interaction during propagation in optical fiber will be different for each wavelength as explained in more detail in section 5.

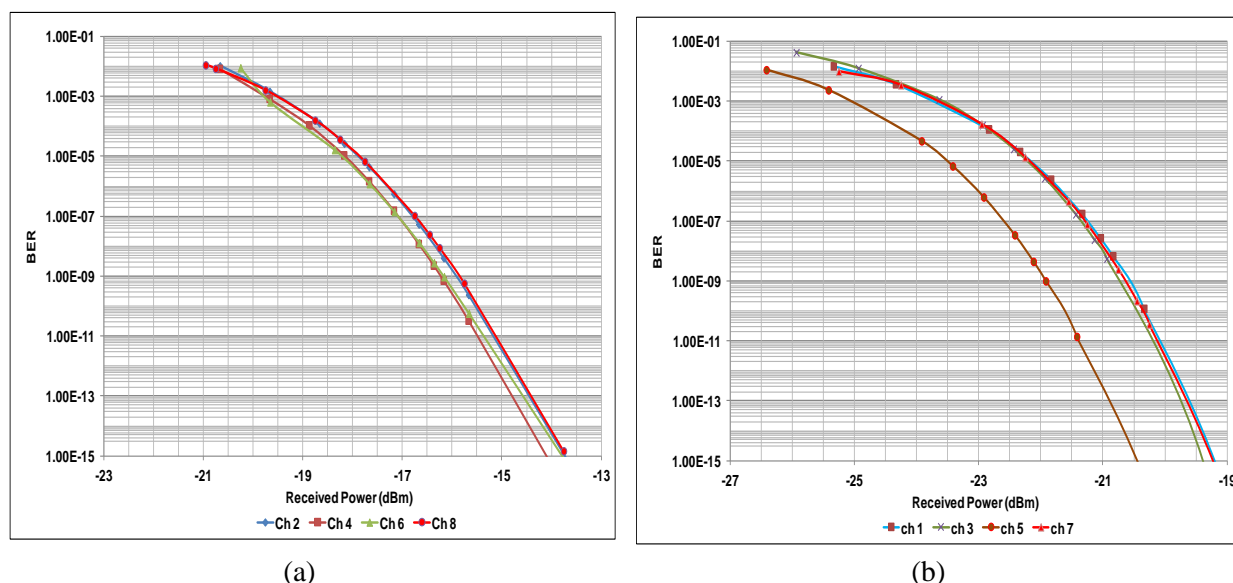


Figure 3. System performance of 8-channel 100-GHz spacing hybrid H 10 -40 configuration with NRZ modulated signals with 60 GHz MUX/DEMUX BW (a) 40 Gbps data rate (b) 10 Gbps data rate.

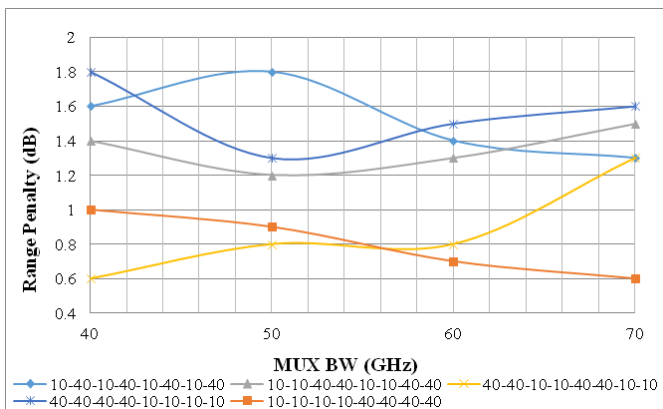
4. CIRCULATING LOOP SIMULATION

Figure 6 illustrates the block diagram of the circulating loop configuration used in the simulations to investigate the maximum propagating distance of signals for a selected hybrid optical communication system. The hybrid H 10 – 40 configuration is used in performance evaluation for NRZ and RZ pulse formats. The loop is made up of 50km of NZ-DSF fiber and 10km of DCF. Figure 7 and Figure 8 show the system performance of 10G and 40G channels propagating in the loop using RZ and NRZ pulses, respectively. It is clear that RZ pulse format outperforms NRZ pulse format. The maximum possible transmission distance for RZ pulses with a MUX/DEMUX BW of 60 GHz is approximately 400km (8 times 50km) which is characterized at BER of 1×10^{-12} and limited by the 40 Gbps channels, while the maximum possible transmission distance for NRZ pulses is about 200km (4 times 50km). The BER variation at high loop count shown in Figure 7 and Figure 8 is an artefact due to high BER values close to 10^{-2} . The MUX/DEMUX BW of 60 GHz is chosen in performance evaluation of pulse format in long distance hybrid rate data transmission, because it gives best performance for 40G data rate as shown in Figure 4b.

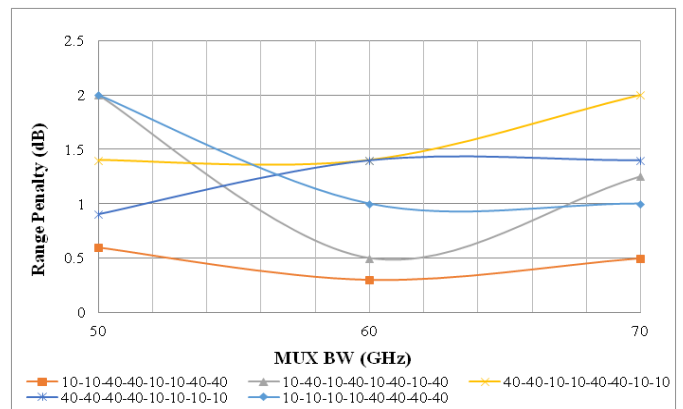
Table 2. Summary of system performance for H 10 – 40 hybrid configuration at 40, 50, 60 and 70 GHz MUX/DEMUX bandwidths at BER = 10^{-12} .

MUX/DEMUX BW GHz	System Performance			
	10 Gbps		40 Gbps	
	Range Penalty dB	Receiver Power Center dBm	Range Penalty dB	Receiver Power Center dBm
40	1.6	-20.70	Failed*	Failed*
50	1.8	-20.30	2.0	-13.0
60	1.4	-20.50	0.5	-15.0
70	1.4	-20.25	1.25	-14.75

* Failed, because signals cannot be detected without using forward error correction (FEC) capability in the system. FEC can correct errors of BER of 1×10^{-3} or lower.



(a)



(b)

Figure 4. System performance range penalty summary at different MUX/DEMUX bandwidths for different hybrid configurations (a) 10 Gbps channels (b) 40 Gbps channels.

5. DISCUSSION

Non-linear Schrödinger equation governs signal propagation in optical fiber. It is given by:

$$\frac{\partial A}{\partial z} + \frac{\alpha}{2}A + \frac{i\beta_2}{2} \frac{\partial^2 A}{\partial T^2} - \frac{\beta_3}{6} \frac{\partial^3 A}{\partial T^3} = i\gamma[|A|^2A + \frac{i}{\omega_0} \frac{\partial}{\partial T} (|A|^2A) - T_R A \frac{\partial |A|^2}{\partial A}] \tag{1}$$

"Effect of Multiplexer/Demultiplexer Bandwidth on Upgrading Current 10G to 40G Optical Communication Systems", A. Atieh, M. Wa'ad and I. Mansour.

where $(T = t - \beta_1 z)$ is a normalizing parameter to reference the moving pulses in a retarded frame. β_1 is the inverse of group velocity (v_g), β_2 is the group velocity dispersion (GVD) parameter, β_3 is the third-order dispersion parameter, α is the fiber attenuation described in dB/km and A is the slowly varying amplitude of propagated pulse electric field along the fiber in the z direction. $|A|^2$ is the optical pulse power, T_R is the Raman time constant and the non-linear parameter γ is given by:

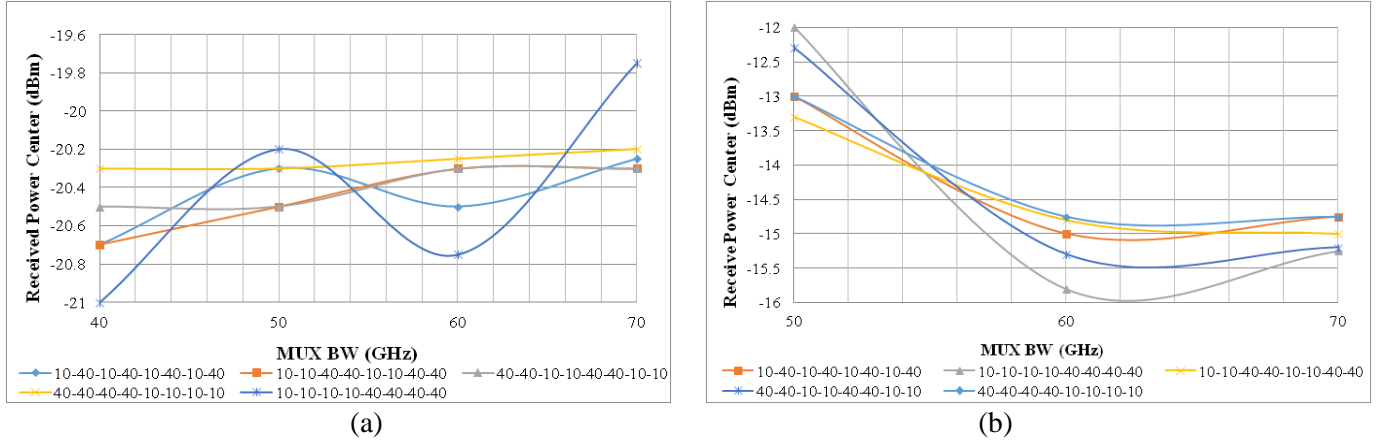


Figure 5. Summary of system performance of received power center value at different MUX/DEMUX bandwidths for different hybrid configurations (a) 10 G bps channels (b) 40 Gbps channels.

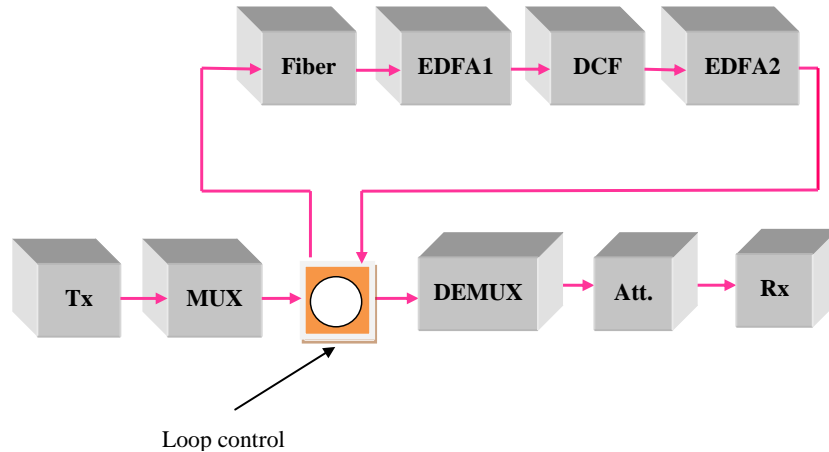


Figure 6. Block diagram of a circulating loop configuration used to investigate maximum propagation distance of signals in hybrid communication systems.

$$\gamma = \frac{n_2 \omega_0}{c A_{eff}} \quad (2)$$

where n_2 is the non-linear refractive index, A_{eff} is the effective core area, c is speed of light in vacuum and ω_0 is related to the propagated optical signal center wavelength λ . The GVD parameter can be positive or negative, depending on whether λ is lower or higher than the fiber zero-dispersion wavelength λ_D . When λ is higher than λ_D , the GVD is negative and this regime is called anomalous-dispersion regime. On the other hand, the regime is called normal dispersion regime when GVD is positive ($\lambda < \lambda_D$). The commonly used fiber dispersion parameter D (ps/km.nm) is related to GVD by:

$$D = -\frac{2\pi c}{\lambda^2} \beta_2 \quad (3)$$

Typically, the red-shifted (lower frequency) components of a propagated pulse travel slower than the blue-shifted (higher frequency) components in the anomalous-dispersion regime, causing the pulses to broaden in the time domain and compress in the wavelength domain. When the blue-shifted components

surpass the red-shifted components, an inverse effect may occur, which causes compression in the time domain. On the other hand, the blue-shifted components travel slower than the red-shifted components in the normal dispersion regime, causing pulses to compress in the time domain and broaden in the wavelength domain.

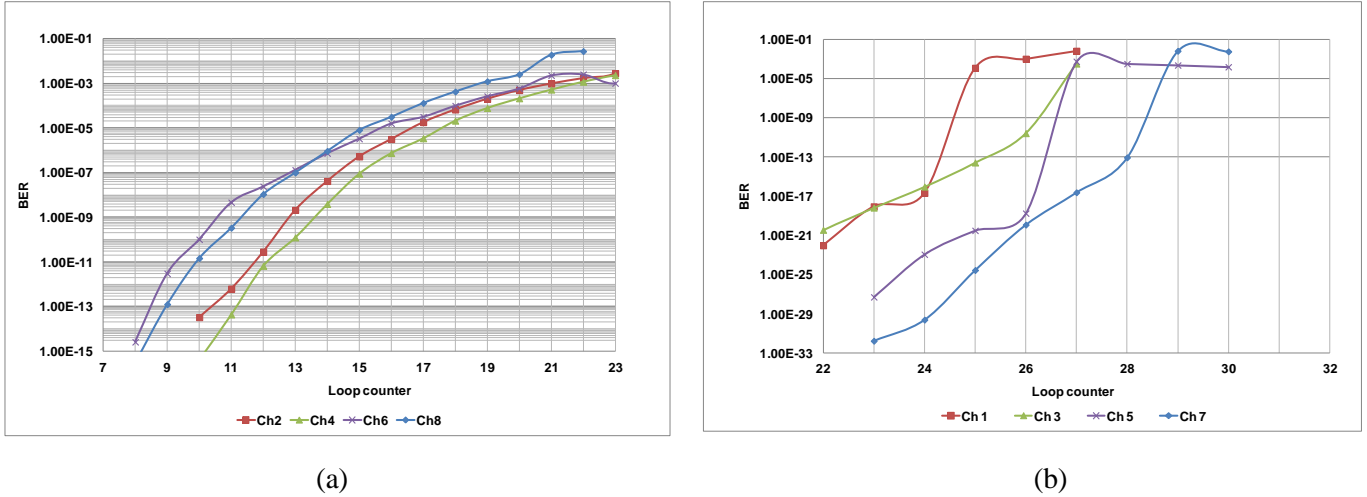


Figure 7. System performance for RZ modulated pulses of H 10 – 40 hybrid configuration propagated in a circulating loop (a) 10 Gbps channels (b) 40 Gbps channels.

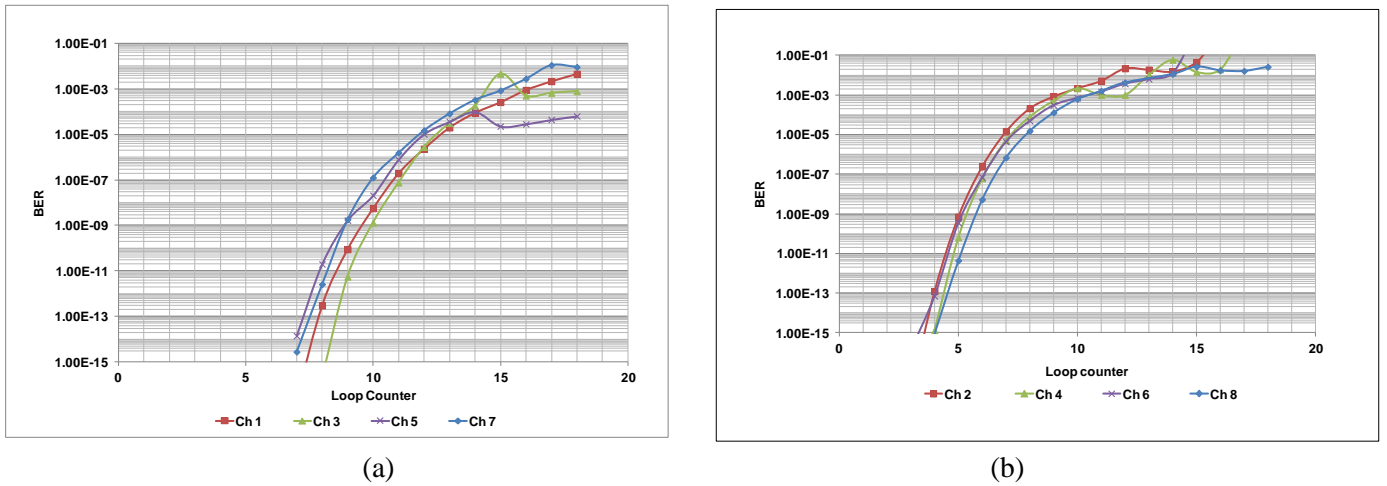


Figure 8. System performance for NRZ modulated pulses of H 10 – 40 hybrid configuration propagated in a circulating loop (a) 10 Gbps channels (b) 40 Gbps channels.

When optical pulses propagate in the optical fiber, they may encounter dispersion effect only, non-linearity effect only, none of these effects or both non-linearity and dispersion effects. In order to determine which effect occurs in the optical fiber, dispersion and non-linear lengths are defined as:

$$L_D = \frac{T_o^2}{\beta_2}, L_{NL} = \frac{1}{\gamma P_o} \tag{4}$$

where T_o and P_o represent the propagated pulse width (1/e width) and peak power, respectively. When $L \ll L_{NL}$ and $L \ll L_D$, neither dispersion effect nor non-linear effect play a role in pulse evolution in the optical fiber. When $L \ll L_{NL}$, but $L \sim L_D$, the propagated pulses encounter dispersion only, while the non-linear effect in the fiber is negligible. On the other hand, when $L \sim L_{NL}$, but $L \ll L_D$, the dispersion term in Schrödinger non-linear equation will be ignored and the propagated pulses encounter non-linear effects during propagation. In the last case, when the fiber length is longer or comparable to both the non-linear and dispersion lengths, the evolution of pulses in the optical fiber will encounter both fiber dispersion and non-linearities.

The main non-linear effects that propagated DWDM signals encounter in optical fibers are self-phase modulation (SPM), cross-phase modulation (XPM) and four-wave mixing (FWM). Other non-linear effects that signals experience in optical fibers are stimulated Brillouin scattering (SBS) and stimulated Raman scattering (SRS). The effect of SPM and XPM on propagated pulses is to broaden their wavelength content by causing non-linear phase shift. The non-linear intensity-dependent phase shift ϕ_{NL} is given by the following equation for two neighboring signals propagating in the fiber.

$$\phi_{NL} = n_2 k_0 L (|E_1|^2 + 2|E_2|^2) \quad (5)$$

where $|E_1|^2$ and $|E_2|^2$ are the intensities of a signal at a specific wavelength and its neighboring signal at another wavelength selected on ITU-grid. The first term in equation (5) is related to SPM and the second term is related to XPM. Each non-linear effect is triggered in the optical fiber when the propagated signal has a power level that exceeds a specific threshold. The first non-linear effect that optical signals run into is SBS, then SPM and XPM. However, FWM requires extra conditions beyond the power level threshold, which are related to phase and frequency matching of WDM signals propagating in the fiber [21]. The propagated pulses' format also affects the non-linear threshold due to its influence on the average power of the optical signal in the fiber. In addition, optical signal data rate plays a role in the fiber non-linear threshold and affects the sensitivity of propagated signal to dispersion. The higher the signal data rate, the more sensitive the signal propagated pulses to dispersion. NRZ pulses have higher average power compared to RZ pulses for the same data rate. Thus, they are more sensitive to non-linearity. On the other hand, RZ pulses are more sensitive to dispersion compared to NRZ pulses.

Propagated pulses in the optical fiber encounter broadening in the wavelength domain and compression in the time domain, because of SPM and XPM non-linearities. Thus, their effect is opposite to that of dispersion. However, it is too difficult to predict the behavior of dispersion and non-linearity interaction in optical fiber. Hence, numerical simulations are typically conducted in order to find the optimal regime of operation for each hybrid configuration.

Figure 9 and Figure 10 show the BER performance for single wavelength of H 10 - 40 hybrid configuration (Ch 2: 40 Gbps, -16.5 dBm) at different settings of dispersion and non-linearity. The BER parameter is calculated from Q-parameter using Optiwave optisys software. The BER performance curves *versus* dispersion values for different effective core areas are shown in Figure 9. BER performance curves *versus* effective area for different DCF lengths are illustrated in Figure 10. Note that increasing the fiber length does not necessarily give worst BER performance as shown in Figure 10, especially when going from 2.8km to 7.8km. Therefore, it is clear that there is an optimal regime of operation for each combination of A_{eff} and dispersion.

The large difference among each group of channels can be explained through the argument of interaction of fiber non-linearity and dispersion. The laser diode CW power level of each channel is set to 4 dBm. The power of each channel varies at the output of the external modulator due to its wavelength dependence. Figure 2 illustrates the output power per channel for the hybrid configuration H 10 – 40. The variation is over 1 dB. In addition to that, the dispersion of each channel is also different due to non-zero dispersion slope of SMF and DCF optical fibers. The dispersion slopes of SMF and DCF fibers are assumed 0.075 and - 0.3 ps/ (km.nm²), respectively. Thus, the interaction of non-linearity and dispersion in the fiber transmission link is different for each channel as shown in Figure 9 and Figure 10. However, if the power level of all channels is the same, the non-linear effect for all channels will be relatively the same with minor differences due to the dependence of γ on frequency as described in Equation 2. The dispersion of each channel also varies slightly due to optical fibers' dispersion slopes. Thus, the BER performance of channel 5 is expected to be closer to the other channels shown in Figure 3b when its power level equals the power levels of other channels.

6. CONCLUSIONS

The possibility of transmitting 40G channels over 10G common equipment is investigated. Numerical simulations were conducted to investigate the effect of MUX/DEMUX bandwidth on system performance of hybrid 10G/40G optical communication systems. Different hybrid 10G/40G configurations were evaluated. It was found that the best MUX/DEMUX bandwidth, which could be used

for different configurations, is 60 GHz. However, the configuration 10-10-40-40-10-10-40-40 has lower penalty for 40G channels for all investigated MUX/DEMUX bandwidths, while the configuration 40-40-10-10-40-40-10-10 has the best performance for 10G channels at 40GHz and 50GHz MUX/DEMUX bandwidths. The simulations showed also that it is difficult to predict the hybrid system performance for different configurations due to unpredictable interaction between dispersion and non-linearity in the optical fiber. It was also found that using RZ pulse format for both 10 Gbps and 40 Gbps modulated signals provides further signal propagation compared to using NRZ pulse format.

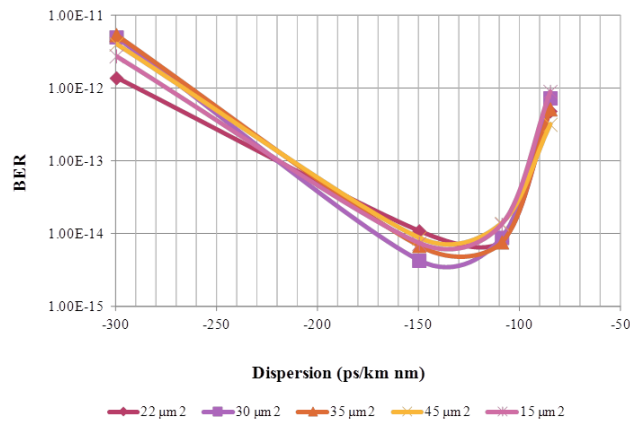


Figure 9. BER performance *versus* DCF dispersion for different A_{eff} (EDFA gain = 5 dB).

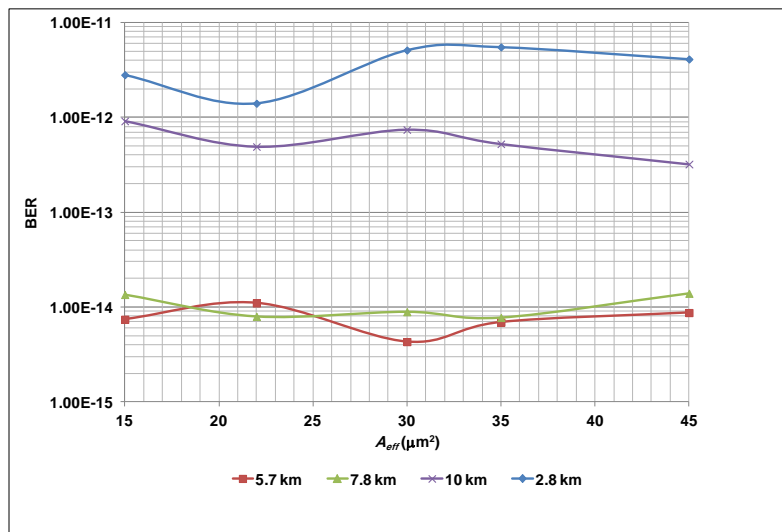


Figure 10. BER performance *versus* A_{eff} for different lengths of DCF (EDFA gain = 5 dB).

REFERENCES

- [1] K. Fukuchi, T. Ono and Y. Yano, "10 Gbit/s-120 km Standard Fiber Transmission Employing a Novel Optical Phase-encoded Intensity Modulation for Signal Spectrum Compression," Optical Fiber Communication Conference (OFC'97), pp. 270-271, Feb. 1997.
- [2] K. S. Cheng and J. Conradi, "Reduction of Pulse-to-pulse Interaction Using Alternative RZ Formats in 40-Gb/s Systems," IEEE Photonics Technology Letters, vol. 14, no. 1, pp. 98-100, Jan. 2002.
- [3] Y. Jiang, X. Tang, J. C. Cartledge, M. Poirier, M. Boudreau, K. Roberts and A. Atieh, "Electronic Dispersion Pre-compensation for 10.71 Gb/s NRZ-OOK Using InP and LiNbO₃ Mach-Zehnder Modulators," Electron. Lett., vol. 47, pp. 865, 2011.
- [4] J. Renaudier *et al.*, "Performance Comparison of 40G and 100G Coherent PDM-QPSK for Upgrading Dispersion Managed Legacy Systems," National Fiber Optic Engineers Conference, CA, US, 2009.

"Effect of Multiplexer/Demultiplexer Bandwidth on Upgrading Current 10G to 40G Optical Communication Systems", A. Atieh, M. Wa'ad and I. Mansour.

- [5] H. Bissessur, "40G over 10G Infrastructure-Dispersion Management Issues," Optical Fiber Communication Conference, Anaheim, California, United States, 2005.
- [6] P. Winzer, "High-spectral-efficiency Optical Modulation Formats," *Journal of Lightwave Technology*, vol. 30, no. 24, pp. 3824-3835, 2012.
- [7] L. N. Binh and T. L. Huynh, "Phase-modulated Hybrid 40Gb/s and 10Gb/s DPSK DWDM Long-haul Optical Transmission," *Optical Fiber Communication and the National Fiber Optic Engineers Conference (OFC/NFOEC)*, pp. 1 – 11, 2007.
- [8] M. Filer and S. Tibuleac, "DWDM Transmission at 10Gb/s and 40Gb/s Using 25GHz Grid and Flexible-bandwidth ROADM," *Optical Fiber Communication Conference/National Fiber Optic Engineers Conference*, Los Angeles, United States, 2011.
- [9] O. Vassilieva, K. Croussore, I. Kim, T. Naito and T. Hoshida, "Suppression of XPM Penalty in Dispersion Managed Hybrid 10G/40G/100G DWDM Networks Using Group Delay Management," *35th European Conference on Optical Communication (ECOC-2009)*, Vienna, Austria, 2009.
- [10] O. Bertran-Pardo, J. Renaudier, G. Charlet, H. Mardoyan, P. Tran, M. Salsi and S. Bigo, "Overlaying 10 Gb/s Legacy Optical Networks with 40 and 100 Gb/s Coherent Terminals," *Journal of Lightwave Technology*, vol. 30 no. 14, pp. 2367-2375, 2012.
- [11] D. McGhan, C. Laperle, A. Savchenko, C. Li, G. Mak and M. O'Sullivan, "5120-km RZ-DPSK Transmission over G.652 Fiber at 10 Gb/s without Optical Dispersion Compensation," *IEEE Photonics Technology Letters*, vol. 18, no. 2, pp. 400-402, 2006.
- [12] R. A. Griffin, A. Tipper and I. Betty, "Performance of MQW InP Mach-Zehnder Modulators for Advanced Modulation Formats," *Optical Fiber Communication Conference (OTuL5)*, 2005.
- [13] Z. Zhang, L. Chen, X. Bao and A. Atieh, "Partial Bit Delay Correlative Modulation Used to Improve the Dispersion Tolerance of an Optical Duobinary System," *Optics Express*, vol. 16, no. 15, pp. 11344-11353, June 2008.
- [14] Y. Wang and L. Lyubomirsky, "Impact of DP-QPSK Pulse Shape in Non-linear 100 G Transmission," *Journal of Lightwave Technology*, vol. 28, no. 18, pp. 2750-2756, Aug. 2010.
- [15] J. Toulouse, "Optical Non-linearities in Fibers: Review, Recent Examples and Applications," *Journal of Lightwave Technology*, vol. 23, no. 11, pp. 3625-3641, Nov. 2005.
- [16] V. Kamalov, B. Koley, X. Zhao and C. Lam, "Field Verification of 40G DPSK Upgrade in a Legacy 10G Network," *IEEE Conference on (OFC/NFOEC) Optical Fiber Communication (OFC)*, collocated National Fiber Optic Engineers Conference, San Diego, CA, USA, NTuC2, 21-25 March 2010.
- [17] F. Yang, M. Mahic and L. Kazovsky, "Non-linear Crosstalk and Two Countermeasures in SCM-WDM Optical Communication Systems," *Journal of Lightwave Technology*, vol. 18, no. 4, pp. 512-520, Apr. 2000.
- [18] A. Bononi, P. Serena and N. Rossi, "Non-linear Signal–Noise Interactions in Dispersion-managed Links with Various Modulation Formats," *Optical Fiber Technology*, vol. 16, no. 2, pp. 73-85, Mar. 2010.
- [19] H. Zhang, A. Turukhin, O. Sinkin, W. Patterson, H. Batshon, Y. Sun, C. Davidson, M. Mazurczyk, G. Mohs, D. Foursa and A. Pillipetski, "Power-efficient 100 Gb/s Transmission over Transoceanic System," *Journal of Lightwave Technology*, vol. 34, no. 8, pp. 1859-1863, Nov. 2015.
- [20] S. Bilal, K. Goroshko, H. Louchet, I. Koltchanov and A. Richter, "Non-linear Tolerant Modulation Format Enabled Tb/s Superchannel Transmission over 420 km of Unrepeated Raman Amplified Link," *Optical Fiber Technology*, vol. 36, pp 306-311, 2017.
- [21] G. P. Agrawal, *Non-linear Fiber Optics*, 3rd Ed., Academic Press, Jan. 2001.

ملخص البحث:

يحتاج كثير من أنظمة الاتصال الضوئية القائمة ذات السعة 10G الى تحديث لتصبح ملائمة لسعات أعلى (40G، 100G...)؛ من أجل تلبية الطلب المتزايد على نطاقات ترددية أعلى. غير أن كثيرين من المزودين بهذه الأنظمة في دول العالم الثالث تعوزهم الميزانية اللازمة لتغيير المعدات بالكامل في أنظمة الاتصال الضوئية القائمة. لذا، فإن من المهم دراسة أيّ المعدات يمكن الإبقاء عليها عند تحديث الأنظمة القائمة منخفضة السعة لرفع سعتها. فالسؤال الأساسي هنا هو: ما المعدات التي تصلح للسعات المنخفضة والعالية على حدّ سواء؟

في هذه الورقة، يجري استقصاء أثر النطاق الترددي للمرسل المضاعف (MUX) وكاشف الإرسال المضاعف (DEMUX) على أداء أنظمة الاتصال الضوئية الهجينة (40G/10G)، علماً بأن هذه الأنظمة تسمح بإضافة قنوات جديدة بسعات أعلى الى المعدات القائمة ذات السعة 10G. وقد أجريت محاكاة رقمية على 8 قنوات متعاقبة على شبكة الاتحاد الدولي للاتصالات ذات النطاق الترددي 100 جيجاهيرتز تحمل كل منها بيانات بمعدل 10G أو 40G. وقد استخدمت قيم مختلفة للنطاق الترددي للمرسل المضاعف/ كاشف الإرسال المضاعف (40، 50، 60، 70 جيجاهيرتز) من أجل دراسة أداء كل تشكيلة من تشكيلات النظام الهجين. ووجد أن النطاق الترددي الأمثل لجميع تشكيلات النظام المستقصاة هو (60 جيجاهيرتز). وقد جرى تقييم أداء النظام الهجين لكل من نمطي النبضات: الرجوع الى الصفر (RZ)، وعدم الرجوع الى الصفر (NRZ). كذلك، تم استقصاء المدى الأقصى لتشكيلة هجينة منتقاة لكل من نمطي النبضات: الرجوع الى الصفر، وعدم الرجوع الى الصفر.

EDITORIAL BOARD SUPPORT TEAM

LANGUAGE EDITOR

Haydar Al-Momani

EDITORIAL BOARD SECRETARY

Eyad Al-Kouz

JJCIT ADDRESS

WEBSITE: www.jjcit.org

EMAIL: jjcit@psut.edu.jo

ADDRESS: Princess Sumaya University for Technology, Khalil Saket Street, Al-Jubaiha.

B.O. BOX: 1438 Amman 11941 Jordan.

TELEPHONE: +962-6-5359949.

FAX: +962-6-7295534.



المجلة الأردنية للحاسوب و تكنولوجيا المعلومات

ISSN 2415 - 1076 (Online)
ISSN 2413 - 9351 (Print)

العدد ٢

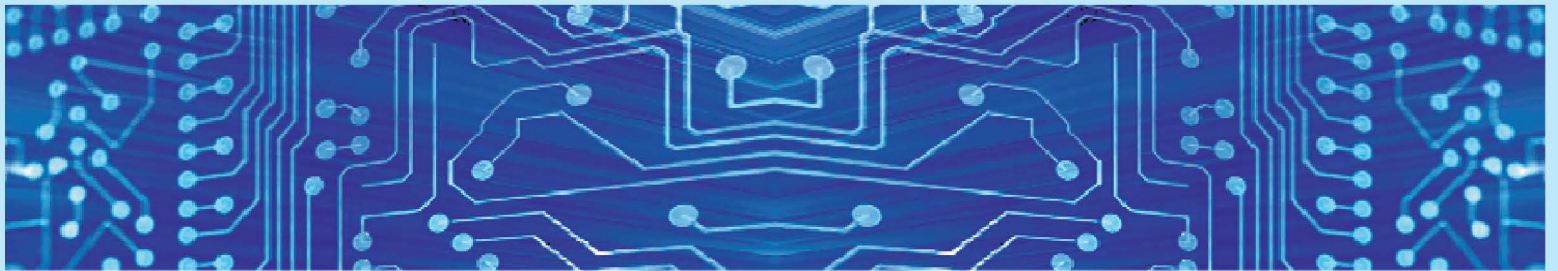
المجلد ٣

آب ٢٠١٧

JJCIT

www.jjcit.org

jjcit@psut.edu.jo



مجلة علمية عالمية متخصصة محكمة
تصدر بدعم من صندوق دعم البحث العلمي